Biophysical and Statistical Modeling for Predicting the Progression and Regression of Cardiac Growth

---

A
Dissertation

Presented to
the faculty of the School of Engineering and Applied Science
University Of Virginia

---

in partial fulfillment
of the requirements for the degree

DOCTOR OF PHILOSOPHY

by

DEREK J. BIVONA

December 2021

APPROVAL SHEET

This
Dissertation
Is submitted in partial fulfillment of the requirements
for the degree of

DOCTOR OF PHILOSOPHY

Author: DEREK J. BIVONA

The dissertation has been read and approved by the examining committee:

Advisor	Jeffrey W. Holmes, MD, PhD
Committee Chair	Silvia S. Blemker, PhD
Committee Member	Kenneth C. Bilchick, MD
Committee Member	Gustavo K. Rohde, PhD
Committee Member	Jason A. Papin, PhD

Accepted for the School of Engineering and Applied Science:

Jennifer L. West, School of Engineering and Applied Science

December 2021

This work is dedicated
to my brother, Alec Bivona, who inspires me with his resilience,
and to my parents, Donna Bivona and John Bivona, who give me more love and support than I can ever imagine.

Acknowledgements

I give my sincerest gratitude to my family and friends who have encouraged and supported me throughout graduate school. The work in this dissertation is the product of many minds, and I would like to thank them all. I want to sincerely thank the following people who contributed immensely to my work:

- Chapter 2 - Ana Estrada & TK Phung
- Chapter 3 - Kyoko Yoshida
- Chapter 4 - Pim Oomen, Srikar Tallavajhala & Mohamad Abdishektaei

I must thank my advisor, Jeffrey Holmes, for his mentorship and guidance over the past five years. Not only did he teach me everything I know about cardiac biomechanics, but he also taught me how to be a researcher of integrity. He always encouraged me to never stop learning and allowed me to push the boundaries of his lab. Working with him has been an incredible experience, and I am so thankful for the opportunity. I would also like to thank Dr. Ken Bilchick for his enthusiasm throughout our collaboration. I had the most fun working with him during graduate school. I was fortunate enough to share Python code with a practicing physician, which was a unique and rewarding experience. I am so grateful he offered me a post-doctoral position upon graduation, and I am excited to continue to work with him.

I need to thank the Cardiac Biomechanics Group who provided a generous learning environment for me to develop as a researcher. Thank you to Pim who offered me continuous support as our lab dwindled in size. Thank you to Laura who always tagged me in fitness challenges on social media. Thank you to Kellen for being the best graduate student role model. Most of all, I need to thank Ana, TK, and Kyoko. Thank you to Ana with whom I shared the successes and failures of finite-element modeling. Thank you to TK for pushing his keyboard aside and placing my laptop oh his desk to help me whenever I asked. More importantly, thank you to both Ana and TK for all the laughs, pranks, and coffee; the two of you made me look forward to going into lab every day. Finally, I want to thank Kyoko from the bottom of my heart; I could not have asked for a better friend, mentor, and emergency contact. Ten years from now, I will not remember the tips she gave me to help my finite-element models converge, but I will remember the way she made me feel when she checked on me every day during one of the most difficult times in my life.

I also want to thank my friends outside of lab. Thank you to Vi for being the best roommate in Park City, Utah during a modeling workshop. Thank you to Hunter for sharing with me the struggles in coursework. Thank you to Corey for chicken tender time in the hospital cafeteria. Thank you to Bruce for the daily walks during the pandemic. Thank you to Marc Paulo for the constant reminders of my self-worth. Thank you to Cailey for being my biggest fan and for calling me seconds before her heart surgery. Thank you to Devrick for our heart-to-heart conversations and our mutual love of music. Thank you to Soham and Lucas for keeping the athlete in me alive and for helping me win multiple intramural championships. Finally, thank you to Sham for saving the day as she set up my Wi-Fi minutes before my defense.

Lastly, I must thank the three most important people in my life: my mom, my dad, and my brother. My mom called me every night to ensure I was happy and healthy. She sent me cards in the mail to remind me how proud she was of me. I thank her for her unconditional love, which carried me through graduate school. My dad made numerous solo trips to Charlottesville to spend time with me, and I want him to know I did not take any of them for granted. He instilled in me from a very young age the discipline and work ethic that allowed me to succeed in graduate school. Our times on the baseball diamond are the memories I hold closest and thought about frequently during my time at UVA. Finally, my little brother has been my best friend since my parents brought him home from the hospital. I always looked forward to playing video games and working out with him every time I went home for a holiday break. More importantly, he has overcome every challenge he has faced in his life and inspires me to do the same. I love you all with my entire heart and dedicate this work to you.

Abstract

Heart disease is the leading cause of death in the United States and affects roughly one third of the adult population. In particular, approximately one million Americans suffer from myocardial infarctions (MI) each year; as a result, they may experience maladaptive cardiac growth and remodeling that leads to heart failure (HF). In fact, around six million Americans currently suffer from HF. Many of these patients also experience electrical conduction delays that cause ventricular dyssynchrony and worsen HF. Heart failure is progressive, with continuing dilation of the heart contributing to ever-worsening pump performance; predicting the course of this remodeling and its modification by treatments could therefore provide important insight. Fortunately, biophysical and statistical modeling provides a low-risk, low-cost framework that allows us to not only gain a better understanding of post-MI remodeling but also predict the progression and regression of heart failure. Therefore, the goal of this work is to develop computational models that can predict the changes in mechanics, composition, and geometry that occur in the heart following MI and the ventricular remodeling that occurs in response to current therapies aimed at reversing HF. We utilize two different modeling approaches to predict the progression and regression of cardiac growth: (1) a biophysical mechanistic model of the infarcted left ventricle (LV) that predicts remodeling during post-infarction healing, and (2) a statistical modeling framework to predict ventricular remodeling and patient outcome following cardiac resynchronization therapy. Overall, my work explores the prevailing concept in biomechanics that the long-term remodeling of mechanically active biologic tissues such as the myocardium can be predicted based on regional mechanics, using two complementary approaches: biophysical models that explicitly link mechanics to remodeling, and statistical models that inform how much of the observed remodeling can be explained by mechanics.

Table of Contents

Chapter 1

1 Introduction

1.1 The Physiology of the Heart: Mechanical and Electrical Properties

The human heart functions as a system of well-coordinated pumps that deliver blood to the body. The heart is made up of four chambers: the right atrium, the right ventricle, the left atrium, and the left ventricle. The right side of the heart sends deoxygenated blood to the lungs to become oxygenated, and the left side of the heart pumps the oxygenated blood to the tissues of the body. The movement of blood from the atria to the ventricles and from the ventricles to peripheral tissue depends on the pressure differences between the chambers along with the contractility and electrical activity of the cells that make up the heart – known as cardiomyocytes. For example, the cardiomyocytes in the left atrium contract and generate pressure within the chamber until it exceeds that in the left ventricle. When this pressure is reached, the mitral valve opens, and a certain amount of blood flows from the left atrium into the left ventricle. Shortly after, the cardiomyocytes within the left ventricle contract and increase the chamber pressure until it exceeds that in the aorta. This causes the aortic valve to open, and the ventricle pumps blood into the aorta and the rest of the body.

The cardiomyocytes are striated muscle cells that contract involuntarily. As they contract and generate pressure within the chambers, they shorten along their axes of orientation, which depend on the location within the walls of the atria and ventricles[1–3]. The timing of this contraction is orchestrated by an organized electrical network of specialized cells that transmits an electrical signal throughout the heart. In a healthy heart, this signal begins at the sinoatrial node located in the right atrium. It then travels to the atrioventricular node where it is split down the right and left bundle branches; the right bundle conducts impulses to the right side of the heart, and the left bundle conducts impulses to the left side. Finally, the signal reaches the lower chambers of the heart through the Purkinje fibers. The precise timing of this normal pattern of electrical signaling allows the atria to contract and pump blood into the ventricles before the ventricles contract and pump that blood throughout the body. As such, the function of a healthy heart relies on its mechanical properties (i.e. cardiomyocyte contraction, chamber pressure, and blood volume within the chambers) and electrical properties (i.e. the timing of cardiomyocyte contraction).

1.2 Diseases of the Heart

1.2.1 Heart Failure & Its Causes

The heart's function can break down due to three conditions that alter normal physiology: (1) mechanical properties of the heart are altered as in viral myocarditis or myocardial infarction; (2) electrical properties are altered as in left bundle branch block; or (3) the load placed on the heart is too great for it to overcome as in pressure overload. An example of altered load occurs when aortic blood pressure is elevated in hypertension. Under this condition, the heart is unable to eject a normal blood volume, which triggers multiple short-term compensatory mechanisms that increase pressure generation to help the ventricle overcome the elevated pressure. This also prompts growth and remodeling over time as the extra work that the ventricle must perform leads to the adaptation of a thicker ventricular wall. The thicker wall results in a structurally stiffer heart, reducing the amount of blood that the ventricle can hold and send to the body[4]. On the other hand, an example of an altered electrical component occurs when there is a blockage of the electrical signaling within the left bundle branch of the heart. The blockage causes the ventricle to contract dyssynchronously. This too reduces the amount of blood that the ventricle can send to the body[5]. Both cases can lead to heart failure. Heart failure is defined as the inability of the heart to pump a sufficient amount of blood through the body and can be characterized by ventricular thickening (concentric hypertrophy) and/or ventricular dilation (eccentric hypertrophy)[6].

Unfortunately, heart failure is common in the United States. According to the American Heart Association, approximately six million Americans suffer from heart failure each year while it causes nearly 400,000 deaths[7]. Heart failure arises from diverse causes, but the four most common are: (1) coronary artery disease, (2) chronic hypertension, (3) cardiac arrhythmias, and (4) valve disease. All of which disrupt the normal mechanical or electrical properties of the heart or the loads placed on it.

1. Coronary artery disease occurs when there is a buildup of plaque in a coronary artery that supplies blood to the heart. This obstruction often leads to a myocardial infarction (heart attack), and the cardiomyocytes located within the obstructed region no longer receive blood and necrose. Depending on the size and location of the infarct, along with

whether the remodeling process within this region offers appropriate mechanical reinforcement, the ventricle may dilate with worsening pump performance, leading to heart failure[8].

2. Chronic hypertension, as mentioned previously, refers to elevated aortic (or blood) pressure and contributes to heart failure as the increased demand of force production leads to ventricular wall thickening and stiffening, which reduces the amount of blood filling and leaving the ventricle[4].

3. Cardiac arrhythmias describe improper beating of the heart due to abnormal electrical impulse origination or propagation. The most common arrhythmia is atrial fibrillation in which the atria beat out of coordination (and often very rapidly) with the ventricles. This decreases the amount of blood that fills the ventricle and lessens the amount of blood that is pumped to the body[9].

4. Valve disease involves conditions that affect the opening or closing of the valves within the heart. One of the most common valve issues is mitral valve regurgitation. In this condition, the mitral valve fails to close tightly and allows blood to flow back into the left atrium from the left ventricle. It burdens the left ventricle with a larger than normal blood volume and may cause the ventricle to dilate and worsen pump performance, leading to heart failure[10].

1.2.2 Myocardial Infarction

Myocardial infarctions (heart attacks) are often consequences of coronary artery disease. In severe cases, the buildup of plaque in the coronary arteries entirely blocks blood flow to a region of the heart, starving the myocardium of oxygen and nutrients, and results in a myocardial infarction (MI). According to the American Heart Association, approximately one million Americans suffer heart attacks each year[7]. While most survive the initial infarction, the remodeling that occurs over the following weeks and months within the damaged infarct region (also known as scar) is a critical determinant of heart function and risk of a range of serious post-MI complications such as infarct rupture and heart failure[11]. In the days and weeks following MI, the myocytes necrose, and their contents are resorbed. Myofibroblasts infiltrate the damaged

region and deposit collagen – a highly abundant protein with great tensile strength – which helps to reinforce the structure of the ventricle. Unfortunately, within the first week, if the structural integrity of the infarct scar is not great enough to support the mechanical loading throughout the cardiac cycle (the filling and pumping of blood), there is a risk of rupture and death. However, if the accumulation of collagen within the first week is sufficient, then the long-term structure and remodeling of the scar region will affect the function of the heart along with heart growth and progression to heart failure[11]. If the infarct is too compliant, the remaining myocardium wastes energy in stretching the infarct, which reduces the amount of blood the ventricle can pump to the body. On the other hand, if the infarct is too stiff, then the ventricle has difficulty filling with blood which again limits pump performance. An infarct also leads to elevated end-diastolic pressure (EDP); higher EDP increases wall stress within the ventricle, which leads to dilation. This dilation also increases wall stress and triggers a downward spiral into heart failure as the ventricle grows in chamber size to adapt to the increase in loading[12]. Current therapies aim to prevent adverse ventricular remodeling with biomaterial injections within the infarct region and mechanical reinforcement of the infarct region[13–15]. Finally, while infarcts disrupt the mechanical function of the heart, they also disrupt its electrical function because the infarct region is no longer electrically conductive. Depending on the size and location of the infarct, the electrical signal may be disrupted to such a degree to cause left bundle branch block and worsen heart failure[16].

1.2.3 Left Bundle Branch Block

A healthy heart beats in a synchronous, coordinated manner due to normal electrical impulses that travel through an organized network of specialized cells. Arrhythmias and conduction disorders arise when abnormalities exist in the generation or conduction of these electrical signals. There are many factors that can interfere with normal rhythm and electrical conduction and include congenital abnormalities of atrioventricular structure or function, electrolyte abnormalities, hypoxia, hormonal imbalances, drug and toxin consumption, hypertension, myocarditis, cardiomyopathy, and myocardial infarction. One of the most common electrical conduction delays is left bundle branch block (LBBB)[5]. LBBB refers to the delay or blockage of electrical impulses to the left side of the heart. It is often present in patients with heart failure and a previous MI, as the non-conductive infarct scar slows or even blocks the electrical signal. This leads to dyssynchrony of contraction within the left ventricle. The pump function deteriorates

from a nearly instantaneous contraction of the entire ventricle to an inefficient, gradual sequence around the muscle chamber. This pattern of contraction promotes ventricular dilation and worsens heart failure. Current therapies aim to use pacemakers to resynchronize ventricular contraction and reverse heart failure[16].

1.3 Computational Modeling for Heart Disease

Complex interactions between the various factors that contribute to ventricular remodeling and heart disease make it difficult to not only understand the course of disease progression but also design therapies to combat and reverse it. Conducting the experiments needed to elucidate such interactions while also testing potential therapies is costly and time-consuming. Fortunately, computational modeling provides a low-risk, low-cost, highly iterative framework that allows researchers to gain a better understanding of heart disease and test the feasibility of therapies. Computational modeling uses mathematics to represent and describe real-world situations. Models can be used to develop a better understanding of a problem by quantitatively expressing the current knowledge of a system, to test the effect of a change or intervention within a system, and to aid in decision making[17]. There are many types of computational models, but most can fall into one of two categories: (1) biophysical mechanistic modeling or (2) statistical modeling. The two modeling techniques differ in how they describe a system[18]. Biophysical mechanistic models represent a system using expressions that describe its underlying processes with a defined set of assumptions. On the other hand, statistical modeling represents a system by describing its generated data under a set of statistical assumptions. Overall, when appropriately applied, both biophysical mechanistic models and statistical models can advance the current state of heart disease research.

1.3.1 Biophysical Mechanistic Modeling

Biophysical mechanistic modeling is a subset of computational modeling that uses mathematical expressions to represent the processes of a system. In the case of cardiac computational modeling, different types of biophysical models are used to represent the actions of the heart across different scales from gene expression and cell growth of cardiomyocytes to the hemodynamics of the cardiovascular system to the deformation of the entire ventricle during a heartbeat. For example, cell-signaling models capture the behavior of intracellular signaling

pathways with differential equations and can be used to predict cardiomyocyte gene expression and hypertrophy when the regular signaling network is perturbed[19]. Another type of mechanistic model is compartmental modeling which uses a system of differential equations to describe the movement of a substance from one compartment to another. Compartmental models have been applied to the cardiovascular system to better understand the relationship between pressures and blood volumes within the different chambers of the heart and how this relationship changes in pathologic conditions that lead to heart growth[20]. A third example of a biophysical mechanistic model, and the one further developed in this dissertation, is finite-element analysis (FEA). FEA is a powerful modeling technique that uses continuum mechanics to describe how a three-dimensional object deforms when under load. It is used often to predict the deformation of the heart in both physiologic and pathologic conditions[21]. FEA has also been used previously to predict ventricular growth when homeostatic conditions are disrupted and has also allowed for *in-silico* testing of certain therapies following a myocardial infarction[15, 22]. The process of building and running FE models is arduous and computationally expensive, especially for routine clinical use; however, FE models can be advantageous in time-insensitive applications as they can be customized to represent the anatomy of a specific patient and produce high resolution spatial information.

1.3.2 Statistical Modeling and Machine Learning

Statistical models and machine learning use mathematical expressions along with probability and statistics to uncover patterns within data generated by a physical system, which aids in predicting specific outcomes. These types of models have recently been recognized as promising approaches in cardiovascular research and can range in complexity. One of the simplest statistical models is linear regression. A linear regression model estimates the association of one or more independent, explanatory variables with a continuous, dependent response variable by fitting a line to the data that best captures their relationship. These models are common in medical research, especially with respect to heart disease, as many studies have used them to investigate and quantify the association of several different factors with an outcome of interest. For example, a linear regression model has been constructed to predict the change in left ventricular volume (outcome) following the implantation of a pacemaker using a set of clinical factors/variables that describe a patient's left ventricular contraction and scar formation[16]. On the other hand, more complex models have been implemented to aid physicians

in making difficult decisions. A convolutional neural network is an example of a commonly used, complex model within medical research. These models usually take an image as input, assign importance to various aspects within the image, and produce a desired output. They have been used to identify cancerous cells within histological images and to segment the different chambers of the heart from echocardiographic and magnetic resonance images[23, 24]. While these models are powerful tools, they rely on the quantity and quality of available data and aim to make predictions without accounting for the underlying biophysical processes. Even though they tend to perform poorly with sparse data and can be difficult to interpret at times, when accurately trained and implemented, these models run very quickly and can provide guidance in the clinic in near real-time.

1.4 Thesis Overview

In this dissertation, I developed both biophysical mechanistic based models and statistical models for predicting the progression and regression of cardiac growth. Chapter 2 presents a biophysical mechanistic model of the infarcted left ventricle that predicts geometric remodeling during post-infarction healing. This model predicts changes in infarct scar dimensions over time along with the deformations that occur in the infarct during ventricular contraction. Chapter 3 extends this model to predict the amount of growth that occurs in the non-infarcted (remote) region. Together, Chapters 2 and 3 result in the most comprehensive model to date of post-infarction ventricular remodeling. In Chapter 4 I present a statistical modeling framework that predicts ventricular remodeling and patient outcomes following pacemaker therapy. We use several different statistical models along with various types of data to explain the regression of cardiac growth. Overall, the work in this dissertation explores the prevailing concept in biomechanics that the long-term remodeling of mechanically active biologic tissues such as the myocardium can be predicted based on regional mechanics, using two complementary approaches: biophysical models that explicitly link mechanics to remodeling, and statistical models that inform how much of the observed remodeling can be explained by mechanics.

Chapter 2

2 A Finite-Element Model of Changes in Mechanics, Composition, and Geometry During Post-Infarction Healing

2.1 Introduction

2.1.1 Scar Remodeling Process: Changes in Composition and Shape

According to the American Heart Association (AHA), approximately one million Americans suffer from heart attacks each year[7]. A heart attack, or myocardial infarction (MI), occurs when a blockage in the coronary arteries prevents oxygenated blood from reaching certain regions of the heart. While most patients survive the initial infarction, the long-term remodeling of both the damaged infarct region and the undamaged (remote) regions are critical determinants of patient outcome and risk of progression towards heart failure[25].

There are numerous, complex physiologic processes that occur in the left ventricle (LV) following a myocardial infarction, which include the necrosis of myocytes and deposition of collagen within the scar region, changes in ventricular mechanical load, and the growth of myocytes within the remote region[26, 27]. Immediately after MI, the myocytes in the damaged region necrose, and their contents are resorbed. This causes tissue volume to steadily decrease throughout the subsequent weeks – though it is unknown whether this volume loss occurs isotropically or anisotropically. Myofibroblasts infiltrate the damaged region and deposit collagen, which causes an increase in collagen content (quantified as collagen area fraction) and stiffens the scar region over time[28, 29]. However, the state, or configuration, in which collagen is deposited relies on the mechanical loading of the ventricle at the time of deposition, thus these configurations differ throughout the infarct healing process as the loading conditions change[30]. The mechanical loading of the ventricle depends on its operating pressures and the cavity volume. In the weeks following MI, end-diastolic pressures (EDP) typically fluctuate, depending on the size of the infarct[31]. EDP also varies between patients and, over the course of months, evolves differently per patient based on whether the patient develops heart failure[28, 32–35]. By using non-invasive imaging techniques to measure the thickness of the scar along with one or more

in-plane scar dimensions, several studies have reported changes in scar shape[33, 36–42]. However, these measurements are typically performed in intact, mechanically loaded hearts, where measured dimensions reflect the combined effects of volumetric remodeling, changes in loading, changes in stiffness, and potential changes in unstressed configurations of deposited collagen, making the infarct remodeling data difficult to interpret. In fact, our group recently performed an exhaustive review of quantitative studies of infarct remodeling and found that some studies reported in-plane expansion of the healing infarct while others reported in-plane compaction (shrinkage) when dimensions were measured at end diastole in intact hearts[43]. All studies that measured wall thickness reported gradual thinning of the scar, which can aggravate adverse remodeling of the left ventricle by increasing wall stresses.

2.1.2 Previous Attempts at Post-MI Modeling

Previous studies of post-MI modeling have focused on how infarct dimensions or properties affect mechanics[30, 43–45]. Our lab developed finite-element (FE) models of canine and rat left ventricles, with prescribed thickness and stiffness, to determine the conditions that induce infarct compaction and expansion[43]. While the results of these models illustrated the concept that observed expansion or compaction depends on the balance between infarct thickness and stiffness prescribed in the unloaded state, they did not attempt to reproduce the experimentally observed evolution of scar dimensions, mechanics, and hemodynamics. Another group developed an FE model based on porcine physiology that more accurately represented the temporal changes in both the infarct material properties and the infarct thickness dimensions[44]. This model may allow for the serial assessment of an individual infarct over time, but it is incomplete without the considerations of the typical changes in mechanical load post-MI or the state at which collagen is deposited in the scar over time. Other studies have created post-MI FE models to test potential therapies such as mechanical reinforcement and biomaterial injections. One study simulated the injection of a biomaterial in the infarct region and concluded that the amount of injected material, rather than its stiffness, notably decreased fiber stress in the remote region[46]. This suggests that increasing wall thickness may be the primary mechanism by which biomaterial injections limit adverse remodeling with altering material properties as a secondary mechanism. However, if post-MI FE models do not reproduce the observed *in-vivo* scar dimensions over time, then their ability to prospectively predict potential effects of new interventions under consideration will remain limited.

Currently, no study or model exists that focuses on what originally determines the changes in dimensions and properties. To better interpret the reports of scar dimensions during healing described in the literature and separate the contributions of volumetric growth and remodeling, infarct stiffening, and elevated LV end diastolic pressures (EDPs) typical after infarction, we developed a biophysical mechanistic computational model that addresses the impact of each of these factors on the post-MI remodeling process. In this chapter we build the most comprehensive FE model to date of post-infarction ventricular remodeling by implementing decreases in volume within the infarct scar, increases in scar stiffness, fluctuations in EDP, and changes in the unstressed configurations of newly deposited collagen within the scar region. This model investigates the hypothesis that volume loss within the scar is isotropic and that accounting for changes in reference state during collagen turnover along with changes in EDP is not sufficient to prospectively predict dimension changes during infarct healing.

2.2 Methods

2.2.1 Constructing a Finite-Element Model of the Rat LV

2.2.1.1 Geometry, Loading and Boundary Conditions

Finite-element models require a three-dimensional geometry, boundary and loading conditions, and a constitutive equation that describes the behavior of the material(s) under load. We built new finite-element models of the rat LV by creating an average geometry from CINE magnetic resonance imaging (MRI) scans of three different rats. After segmenting the endocardial (inner layer of the wall) and epicardial (outer layer of the wall) contours in 6-8 short axis slices obtained at end systole for each rat, we calculated the average geometry and defined a finite-element mesh using a pipeline previously developed in our lab[15]. We also added a ring of rigid-body elements adjacent to the basal-most (top) endocardial layer to simulate a valve ring and a ring of pentahedral rigid body elements to seal the apex. Our final mesh consisted of 9847 nodes and 8400 linear hexahedral elements. A physiologic myofiber structure ranging from -60° in the epicardium to 60° in the endocardium was assigned to the geometry. Using the open source finite-element solver FEBio[47], we simulated loading by applying realistic pressures to the endocardium to inflate the LV while fixing the displacement of the basal surface nodes longitudinally and the valve ring in all directions. Because the MRI contours used to generate the

model were obtained at end systole, we scaled the fitted mesh until we obtained an unloaded geometry that resulted in a simulated end-diastolic volume similar to experiments. This unloaded geometry was taken to be stress-free in all simulations. Finally, a representative infarct geometry derived from late-gadolinium enhancement (LGE) MRI was mapped to the mesh. The construction of the FE model of the rat LV is shown in **Figure 2.1**.

Figure 2.1 Construction of the Rat FE Model: Geometry, Loading and Boundary Conditions

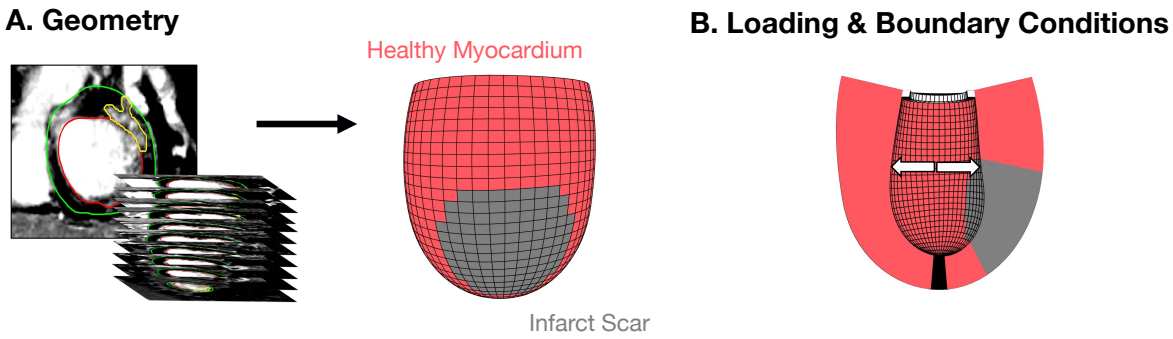

(A) The geometry of the FE model (right) was derived from cine-MRI scans (left), and a representative infarct geometry was incorporated based on LGE MRI. The endocardium is traced in red; the epicardium is traced in green; and the infarct scar is traced in yellow (right). (B) Realistic end-diastolic pressures were applied to the endocardial surface while the displacement of the basal (top) nodes was fixed longitudinally.

2.2.1.2 Material Behavior: Passive Myocardium

A Fung orthotropic constitutive equation was implemented to model the material behavior of the healthy rat LV. Fung elasticity refers to the constitutive relation proposed by Fung and colleagues for characterizing the behavior of biologic soft tissues undergoing finite deformation[48]. A frame-invariant formulation of this relation is implemented in FEBio and is advantageous as it can represent the behavior of tissues with material symmetries ranging from orthotropy to isotropy. The strain energy density function for the Fung orthotropic material is shown in **Equation 1**, and the original orthotropic formulation of Q in terms of the Lamé constants (λ and μ) and the Lagrangian strain components is defined in **Equation 2**[48]. In the implementation of the material law in FEBio, eleven parameters can be defined and related to the Lamé parameters as shown in **Equation 3**. Nine of the eleven FEBio parameters (the Young's moduli in the three orthotropic directions, the shear moduli in the three directions, and Poisson's ratios in the three planes) are

shown on the left-hand side of **Equation 3** while the two additional input parameters include coefficient ***c*** and bulk modulus ***k***.

$$W = \frac{1}{2}c(e^{Q} - 1) + U(J) \qquad \textbf{Equation 1}$$

$$Q = c^{-1}\begin{bmatrix} (\lambda_{11} + 2\mu_1)E_{11}^2 + (\lambda_{22} + 2\mu_2)E_{22}^2 + (\lambda_{33} + 2\mu_3)E_{33}^2 \\ +2\lambda_{23}E_{22}E_{33} + 2\lambda_{31}E_{33}E_{11} + 2\lambda_{12}E_{11}E_{22} \\ +2(\mu_2 + \mu_3)E_{23}E_{32} + 2(\mu_3 + \mu_1)E_{13}E_{31} + 2(\mu_1 + \mu_2)E_{12}E_{21} \end{bmatrix} \qquad \textbf{Equation 2}$$

$$\begin{bmatrix} \frac{1}{E_1} & -\frac{v_{12}}{E_1} & -\frac{v_{13}}{E_1} & 0 & 0 & 0 \\ -\frac{v_{21}}{E_2} & \frac{1}{E_2} & -\frac{v_{23}}{E_2} & 0 & 0 & 0 \\ -\frac{v_{31}}{E_3} & -\frac{v_{32}}{E_3} & \frac{1}{E_3} & 0 & 0 & 0 \\ 0 & 0 & 0 & \frac{1}{G_{12}} & 0 & 0 \\ 0 & 0 & 0 & 0 & \frac{1}{G_{23}} & 0 \\ 0 & 0 & 0 & 0 & 0 & \frac{1}{G_{31}} \end{bmatrix} = \begin{bmatrix} \lambda_{11} + 2\mu_1 & \lambda_{12} & \lambda_{13} & 0 & 0 & 0 \\ \lambda_{12} & \lambda_{22} + 2\mu_2 & \lambda_{23} & 0 & 0 & 0 \\ \lambda_{13} & \lambda_{23} & \lambda_{33} + 2\mu_3 & 0 & 0 & 0 \\ 0 & 0 & 0 & \frac{1}{2}(\mu_1 + \mu_2) & 0 & 0 \\ 0 & 0 & 0 & 0 & \frac{1}{2}(\mu_2 + \mu_3) & 0 \\ 0 & 0 & 0 & 0 & 0 & \frac{1}{2}(\mu_1 + \mu_3) \end{bmatrix}^{-1}$$

Equation 3

The myocardium is commonly modeled as transversely isotropic with a preferred fiber direction in which the material behavior is different compared to that in the other two perpendicular directions (the cross-fiber and radial directions)[49]. Therefore, we simplified the Fung orthotropic material to assume transverse isotropy, reducing the number of material parameters from eleven to five. We let orthogonal vectors $\mathbf{a_2}$ and $\mathbf{a_3}$ define the transverse plane of isotropy ***T*** so that $\mathbf{a_1}$ is normal to that plane and represents the fiber direction. We re-wrote the Lamé parameters to reflect transverse isotropy in **Equation Set 4** and substitute them back into Q as shown in **Equation 5**. This transversely isotropic form of Q can be equated to other widely used constitutive formulations[49–51], such as the one in **Equation Set 6**, by relating the material coefficients in **Equation Set 4** to those used in the other notation (**Equation Set 6**). Finally, in **Equation Set 7**, we relate the transversely isotropic Lamé parameters to the input FEBio parameters from **Equation 3**.

$$\mu_2 = \mu_3 = \mu_T \qquad \lambda_{22} = \lambda_{33} = \lambda_{23} = \lambda_T$$
$$\mu_1 = \mu \qquad \lambda_{21} = \lambda_{31} = \lambda_{23} = \lambda_L$$
$$\lambda_{11} = \lambda$$

Equation Set 4

$$Q = c^{-1}\begin{bmatrix} (\lambda + 2\mu)E_{11}^2 + (\lambda_T + 2\mu_T)E_{22}^2 + (\lambda_T + 2\mu_T)E_{33}^2 \\ +2\lambda_T E_{22}E_{33} + 2\lambda_L E_{33}E_{11} + 2\lambda_L E_{11}E_{22} \\ +4\mu_T E_{23}E_{32} + 2(\mu_T + \mu)E_{13}E_{31} + 2(\mu + \mu_T)E_{12}E_{21} \end{bmatrix}$$

Equation 5

$$Q = b_1 E_{FF}^2 + b_2(E_{RR}^2 + E_{CC}^2 + E_{RC}^2 + E_{CR}^2) + b_3(E_{RF}^2 + E_{FR}^2 + E_{CF}^2 + E_{FC}^2)$$

$$b_1 = c^{-1}(\lambda + 2\mu) \qquad \lambda_T = 0$$
$$b_2 = c^{-1}(\lambda_T + 2\mu_T) \qquad \lambda_L = 0$$
$$b_3 = c^{-1}(\mu_T + \mu) \qquad \lambda = c(b_1 + b_2 - 2b_3)$$
$$0 = c^{-1}(2\lambda_T) \qquad \mu_T = \frac{c}{2}b_2$$
$$0 = c^{-1}(2\lambda_L) \qquad \mu = c\left(b_3 - \frac{1}{2}b_2\right)$$

Equation Set 6

$$E_1 = \lambda + 2\mu \qquad G_{12} = \frac{1}{2}(\mu + \mu_T)$$
$$E_2 = 2\mu_T \qquad G_{23} = \mu_T = \frac{E_2}{2}$$
$$E_3 = 2\mu_T = E_2 \qquad G_{31} = \frac{1}{2}(\mu + \mu_T) = G_{12}$$

Equation Set 7

The parameters we chose to optimize to model the passive material behavior of the LV included $\boldsymbol{E_1}$, $\boldsymbol{E_2}$, $\boldsymbol{G_{12}}$, and $\boldsymbol{c}$ while holding $\boldsymbol{k}$ equal to 100 kPa. We ran 500 Monte Carlo simulations with different sets of material parameters and chose the parameter set that minimized the sum of the squared error between the simulated metrics corresponding to five experimental metrics from previously published experiments[28]: (1) end-diastolic volume (EDV) at an end-diastolic pressure of 0.69 kPa, which captured the overall compliance of the ventricle; (2) E_{max}, which refers to the high pressure slope describing the passive behavior of the ventricle at high pressures and calculated by taking the slope between the volumes at 11.3 kPa and 14.7 kPa; (3) shape index, which is the ratio of the short-axis length to the long-axis length at end-diastole and is influenced by the anisotropy of the myocardium; and (4) circumferential (E_{cc}) and (5)

longitudinal strain (E_{cc}), which describe the deformation of the ventricle in the circumferential and longitudinal directions at low pressures throughout inflation and were calculated from changes in distance between sonomicrometry crystals placed on the surface of rat LVs. **Figure 2.2** shows that the results of the optimized model agree well with the data and that the optimal material parameter set is similar to those previously published by Omens[52] as parameter ***c*** was approximately 1.1 kPa, $\boldsymbol{b_1}$ was the largest value of the ***b*** parameters (corresponding to the preferred fiber direction of myocardium), and $\boldsymbol{b_2}$ was the smallest of the ***b*** parameters.

2.2.1.3 Material Behavior: Infarct Scar

We used a Fung orthotropic material to model the material behavior of the infarct scar. We constructed a single element biaxial mechanical test in FEBio, prescribed equibiaxial stretches up to 1.06 in the X1 and X2 directions, and chose parameters to match experimental stresses from a piece of infarct scar subjected to the same biaxial protocol. Because the infarct scar exhibits in-plane isotropy, we set the $\boldsymbol{E_1}$ and $\boldsymbol{E_2}$ parameters, which govern the stress response in the fiber (X1) and cross-fiber (X2) direction respectively, equal and adjusted their value while holding the other material parameters at the levels chosen for myocardium. The results from the simulation with the best parameters ($\boldsymbol{E_1} = \boldsymbol{E_2} = 94$ kPa) match the experimental data as shown in **Figure 2.3**.

Figure 2.2 Material Behavior: Passive Myocardium

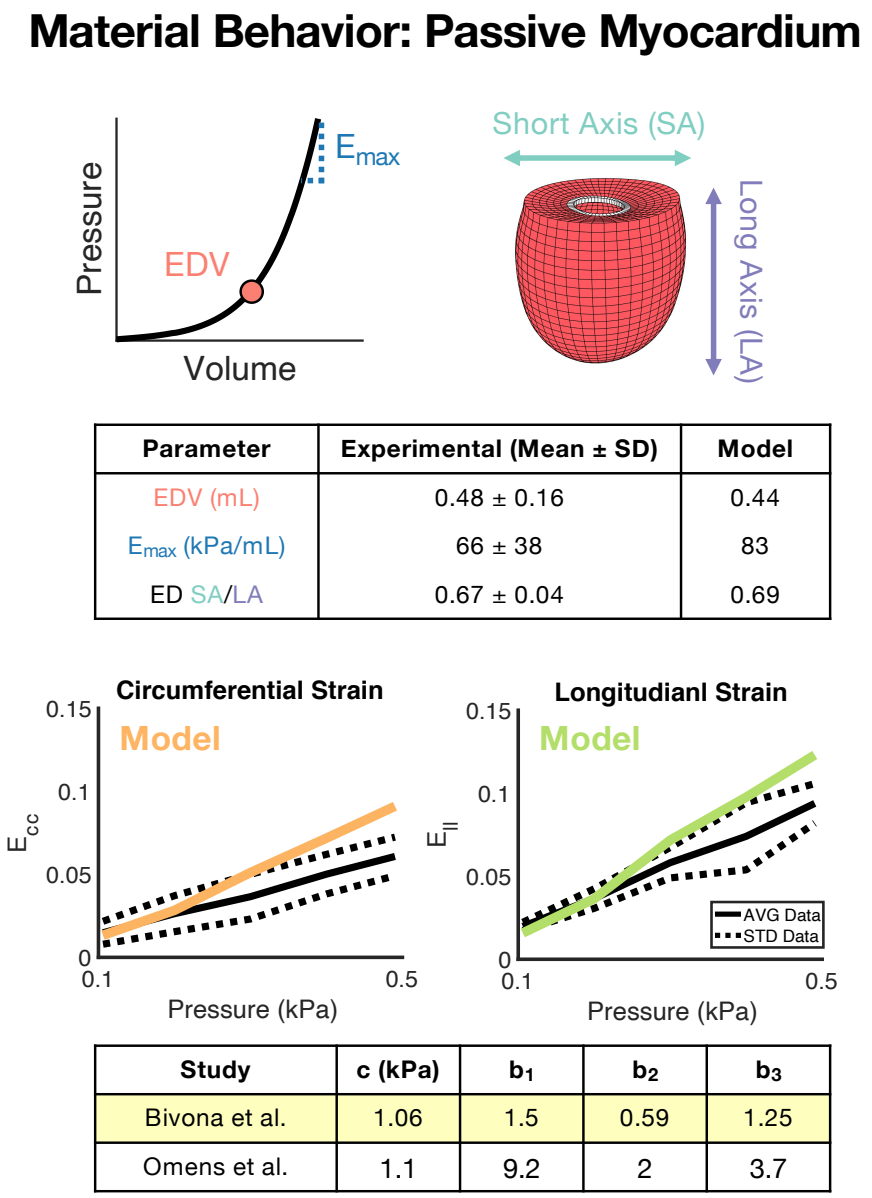

Parameter	Experimental (Mean ± SD)	Model
EDV (mL)	0.48 ± 0.16	0.44
E_{max} (kPa/mL)	66 ± 38	83
ED SA/LA	0.67 ± 0.04	0.69

Study	c (kPa)	b_1	b_2	b_3
Bivona et al.	1.06	1.5	0.59	1.25
Omens et al.	1.1	9.2	2	3.7

The EDV, E_{max}, and shape index (ED SA/LA) of the optimized model all fall close to the mean of the experimental data. The circumferential and longitudinal strain fall within one standard deviation of the mean of the data during early inflation but deviate slightly from the experimental range around a pressure of 0.25 kPa. The optimal material parameters (highlighted) are comparable to those previously published.

Figure 2.3 Material Behavior: Infarct Scar

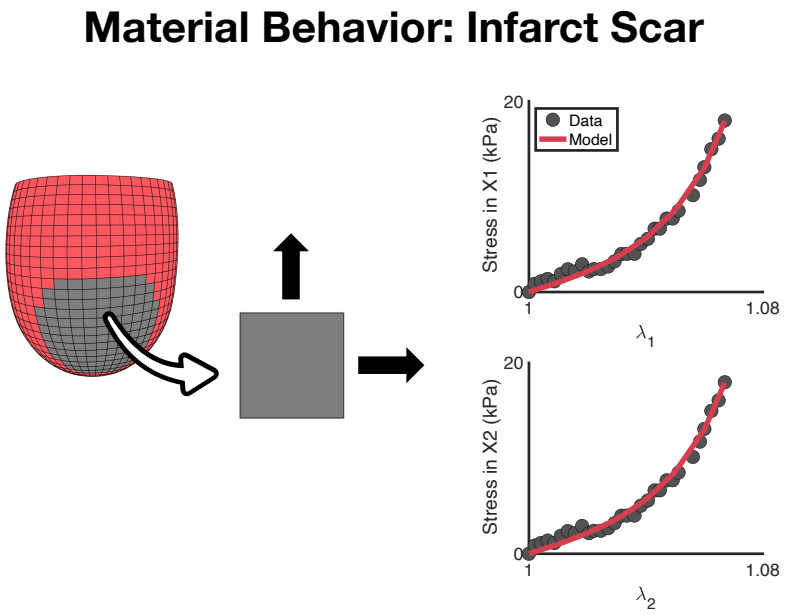

The stretch-stress response of the single element simulation representing infarct scar matches the experimental behavior.

2.2.2 Testing Three Different Approaches in Predicting Post-MI Scar Dimensions

Successfully predicting post-MI infarct dimensions requires accurate modeling of volume change, changes in collagen content and the associated increase in tissue stiffness, collagen deposition state, and changes in mechanical loading; however, it is unknown whether volume loss occurs isotropically or anisotropically and how the configuration in which collagen is deposited influences the post-MI dimensions and mechanics. Therefore, we developed and implemented three different models of scar remodeling in an attempt to match experimental post-MI infarct dimensions at multiple time points.

2.2.3 FEBio Material Plug-In

Changes in volume within the infarct scar occur in each of the three proposed models. To properly model volume change, we developed a custom FEBio material plug-in to prescribe volumetric growth and atrophy within the FE framework. We modified the compressible Fung orthotropic material to include user-defined growth or atrophy in the fiber, cross-fiber, and radial directions. Growth was implemented using the multiplicative decomposition method, or

kinematic framework, derived by Rodriguez et al.[53] (**Equation 8**). This framework defines the total deformation of a growing material as the product of a growth deformation and an elastic deformation. The framework states that the stress of a material depends only on the elastic stretch experienced by the material rather than total stretch. We introduced this framework into FEBio by redefining the stress and tangent definitions within the Fung material in terms of the elastic stretch; all tensors and invariants in the material plug-in were calculated using the elastic stretch as shown in **Equation Set 9**. Ultimately, this new growth Fung material allows the user to simulate growth or atrophy by inputting the components of the diagonal growth stretch tensor F_g as shown in **Equation 10** and then calculates stress based on the elastic tensor. We plan on making our plug-in available to the public by uploading it to https://febio.org/plugins/.

$$F_{total} = F_e \cdot F_g \qquad \textbf{Equation 8}$$

$$\sigma = \sigma(F_e)$$
$$F_e = F_{total} \cdot \left(F_g\right)^{-1} \qquad \textbf{Equation Set 9}$$

$$F_g = \begin{bmatrix} F_{g,fiber} & 0 & 0 \\ 0 & F_{g,cross-fiber} & 0 \\ 0 & 0 & F_{g,radial} \end{bmatrix} \qquad \textbf{Equation 10}$$

2.2.4 Candidate Model 1: Isotropic Kinematic Volume Loss

The first candidate model of post-infarction scar remodeling hypothesizes that volume is lost within the region isotropically (i.e., equal amounts of volumetric loss in the fiber, cross-fiber, and radial directions of the ventricle), and that reported differences between in-plane vs. radial remodeling in the loaded LV are due to the effects of anisotropic material properties. In this model, we prescribed the remaining scar volume based on experimental data with the constraint that the components of the diagonal growth stretch tensor F_g are the same and less than 1. We estimated the remaining scar volume throughout the healing process by multiplying together the average scar area values and the average scar thickness values reported in the literature[37–43]. We also prescribed collagen area fraction (CAF), based on experimental data from our lab[29], after first implementing a solid mixture of 15 materials within the elements representing scar. This

allowed us to prescribe experimental CAF values by declaring the appropriate number of materials in the solid mixture as collagen/scar and inputting the infarct scar material parameters found previously. For example, at 2-weeks post-MI, the average collagen area fraction within the scar region is ~26%[29]. Therefore, we defined 4 out of the 15 materials within the solid mixture as collagen and assigned the appropriate material parameters. Since the stress response of a solid mixture within FEBio is the sum of the stress responses of each of the materials within the solid mixture, we divided the appropriate material parameters by 15 to ensure accurate stress calculations. The derivation of the stress equations and explanation of the division by 15 is explained in **Appendix 2.6.1**. Additionally, we inflated the model to experimentally measured end-diastolic pressures which typically fluctuate throughout the healing process[28]. This approach of prescribing physiologically relevant isotropic volume loss, collagen area fraction, and end-diastolic pressure was performed at 2- and 6-week post-MI time points, and the values of each input at these time points, along with all other times during infarct healing, are shown in **Table 2.1** and correspond to mean values reported in experiments[28, 29, 33, 36–42]. In-plane scar area on the epicardial surface and average scar thickness were calculated at 2- and 6-weeks post-MI and were normalized to their respective values in the non-remodeled scar at a normal end-diastolic pressure. An example of isotropic kinematic volume loss within the FE model at 2 weeks post-MI, with a remaining scar volume of 92%, is shown in **Figure 2.4A**.

2.2.5 Model 2: Anisotropic Kinematic Volume Loss

In the second proposed model of post-infarction scar remodeling, we hypothesize that volume is lost within the scar region in an anisotropic manner, that is, volume loss occurs differently in the three different directions. Here, for each post-MI time point, we prescribed the anisotropic growth tensor that best fit the *in-vivo* scar dimensions through an optimization scheme that swept numerous combinations of the components of F_g with the constraint that the growth/atrophy in the cross-fiber direction was the same as that in the fiber direction. As in **Model 1**, we also prescribed the correct CAF and EDP at each post-MI time point and calculated the scar dimensions. The solution space for the anisotropic kinematic volume loss model is pictured in **Figure 2.4B.** The optimal growth tensor is the same for both the 2-week and 6-week models and is $F_g = \text{diag}[1.2 \quad 1.2 \quad 0.80]$.

Figure 2.4 Scar Remodeling Models: Isotropic & Anisotropic Kinematic Volume Loss

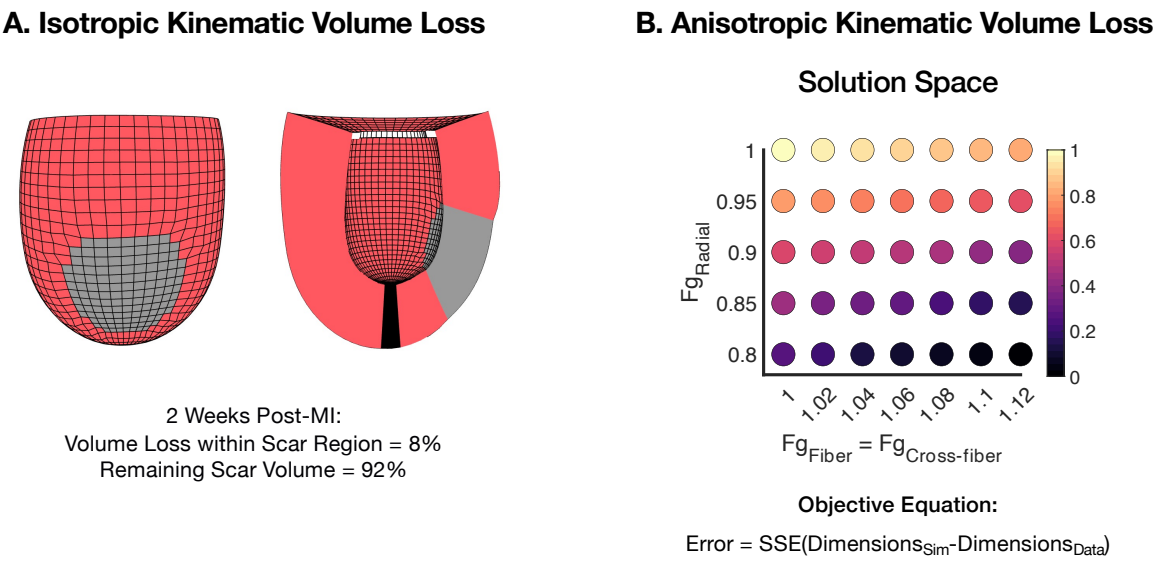

(A) The isotropic kinematic volume loss model exhibited equal amounts of volume loss in the plane of the scar and in scar thickness. The 2-week post-MI model is shown with a remaining scar volume of 92%. (B) The anisotropic kinematic volume loss model was prescribed different patterns of growth and volume loss in the different directions to match *in vivo* scar dimensions. The solution space from the optimization scheme is shown. Anisotropic growth tensors with an $F_{g,Fiber}$ values greater than one and $F_{g,Radial}$ values less than one best match experimental data.

2.2.6 Model 3: Reference Configuration Update + Isotropic Kinematic Volume Loss

The third proposed model of post-infarction scar remodeling theorizes that – like in **Model 1** – volume loss occurs isotropically within the scar region, but that collagen deposition at different unstressed (reference) lengths over time generates anisotropic changes in loaded post-MI dimensions. The reference length of collagen directly affects its material behavior[30]. For example, a collagen fiber with a reference length of 1 immediately exhibits a stress response upon loading. However, a fiber with a reference length of 1.15 shows no stress response (stress = 0) until an applied load causes the fiber to experience a stretch greater than 1.15. We can simulate different reference lengths (or reference configurations) within constituents in two different ways. First, we can prescribe the new reference configuration as a growth stretch, with the determinant of F_g equal to 1 to conserve volume, using the growth plug-in. On the other hand, we can find a new set of material parameters, for a fiber with no reference configuration update, that generates a stretch-stress response that is the same as the response in a fiber with a prescribed change in

reference configuration. This is shown in **Figure 2.5A**. Here, we constructed a single-element biaxial mechanical testing simulation, in which a stretch of 1.25 is applied in both the X and Y directions, for three different cases: (1) a material with no reference configuration update, (2) a material with a reference configuration update of $F_g = \text{diag}[1.15 \quad 1.15 \quad 0.76]$, and (3) a material without a reference configuration update but with a new set of material properties that match the stress-stretch behavior from case (2). These simulations show a rightward-shift of the original stress-stretch curve in Case 1, demonstrating that the stress response in Cases 2 and 3 is not triggered until a stretch greater than 1.15 is applied. We used this approach in the third model of post-infarction scar remodeling to capture the different reference configurations of collagen deposited at different times during infarct healing.

Running this third model involved an iterative process. Initially, the scar region began as a solid mixture of 15 materials, representing passive myocardium before any remodeling or deposition of collagen. In the first step of the simulation, the ventricle was loaded to the average acute end-diastolic pressure. At this loaded state, the configuration of the scar was computed. We calculated the fiber, cross-fiber, and radial stretches of the scar elements and averaged each of these three components, which we defined as the unstressed/reference configuration of the collagen to be deposited in the following step. Next, we simulated the reference configuration update by applying these stretches as growth, via the growth plug-in, in a single element biaxial mechanical test with collagen/scar material properties and calculated the stretch-stress response. In a separate single element simulation (with no prescribed reference configuration update), we optimized the $\boldsymbol{E_1}$ and $\boldsymbol{E_2}$ parameters to match the stress-stretch behavior from the model with the applied growth stretch. Then, to appropriately account for the deposition of collagen and the configuration at which it was deposited within the scar, the $\boldsymbol{E_1}$ and $\boldsymbol{E_2}$ values were updated for a specified number of materials within the infarct scar solid mixture in the full LV model. At the end of this step, the unstressed/reference configuration of this portion of materials was equal to the loaded configuration of the ventricle. Finally, isotropic volume loss was prescribed in the scar region to model the resorption of myocytes, which ended the first step in the series of simulations. This process was performed in iterative steps until 6 weeks of scar remodeling was simulated. Overall, the specific time course of healing (which includes the definition of unstressed configuration updates/collagen deposition and collagen content/area fraction along with changes in scar volume and loading) was based on data generated in our lab as presented in **Table 2.1**. The in-plane scar area and average scar thickness at 2- and 6-weeks

post-MI were calculated as in **Models 1** and **2** and compared to experimental data. A flow chart of this iterative process is depicted in **Figure 2.5B**

Figure 2.5 Scar Remodeling Model: Reference Configuration Update + Isotropic Kinematic Volume Loss

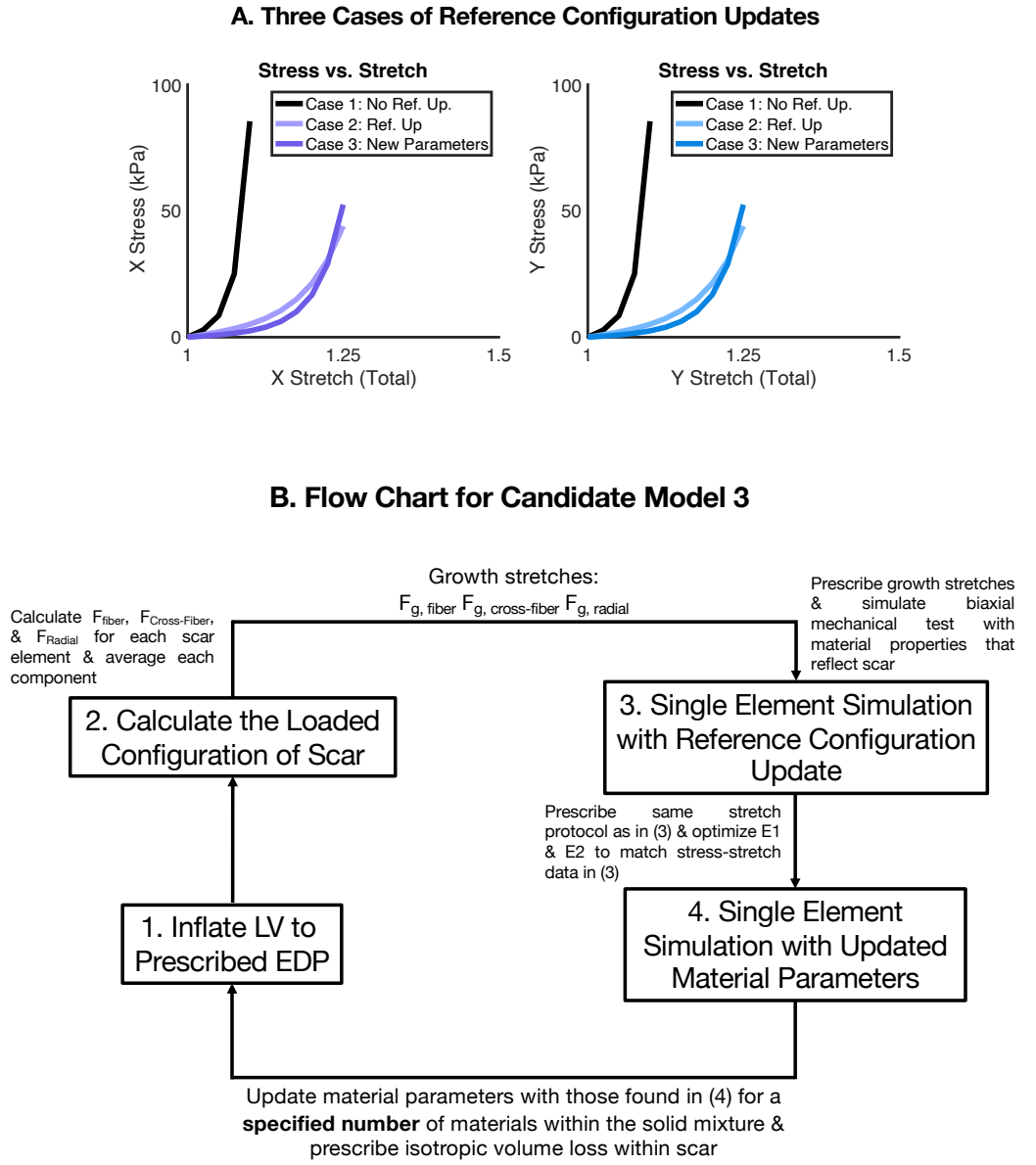

(A) The different approaches to simulating reference configurations updates are shown. First, we can prescribe the new reference configuration as a growth stretch (Case 2). On the other hand (Case 3), we can find a new set of material parameters, for a fiber with no reference configuration update, that generates a stretch-stress response that is the same as Case 2. The rightward-shift of the original stress-stretch curve from Case 1 demonstrates that the stress response in Cases 2 and 3 is not triggered until a stretch greater than the reference length is applied. (B). The flow chart for the model with reference configuration updates and isotropic kinematic volume loss displayed.

Table 2.1 Average Inputs for Scar Remodeling Simulations

Days Post-MI	Remaining Scar Volume (%)	Collagen Area Fraction (%)	End-Diastolic Pressure (kPa)
0	1	0	0.69
2	0.98	0	1.18
7	0.96	0.17	1.27
14	0.92	0.26	1.27
21	0.88	0.35	1.37
28	0.84	0.40	1.18
35	0.80	0.40	1.08
42	0.76	0.46	0.98

2.2.7 Sensitivity Analysis: Determining Main Driver of Scar Dimensions

To determine how each of the three inputs (remaining scar volume, CAF, and EDP) affect the loaded dimensions of the scar, we conducted a sensitivity analysis. For **Models 1** and **3**, after running simulations with the mean values for the model inputs, we ran six different cases in which we either increased or decreased one input by 50% of its mean value while holding the other inputs at their mean values and then calculated the scar dimensions. For **Model 2**, we varied only CAF and EDP as the remaining scar volume was prescribed by design.

2.2.8 Systolic Strain: Comparing Independent Predictions of Candidate Models

We computed and compared the systolic strains of the three different models to test how well the models matched independent data not used to build them. To properly simulate full cardiac cycles, we extended our Fung growth plug-in to include active contraction as done previously in our lab for a different material law[54]. The original Fung orthotropic material was designed to model only the passive properties of a material. Therefore, we reformulated the stress calculation of the material to be the sum of the passive stress component and a new active stress component formulated previously in our group[54]. The active stress component was derived from a length dependent active contraction model currently used in FEBio and a modified force velocity relationship based on Hunter, McCulloch, and ter Keurs[55]. Once we recompiled our plug-in with the active stress formulation, we simulated full cardiac pressure-volume loops by applying the average, acute experimental pressure time course as a boundary condition and optimizing the time-varying contractility curve in non-infarcted elements to match measured pressure-volume loops. **Figure 2.6** shows the pressure-volume loops for the experimental data and optimized model at the acute-MI time point. Once the time-varying contractility curve was optimized, we assumed that it did not change throughout remodeling, and input the average 2-week and 6-week post-MI pressure curves as boundary conditions to simulate full cardiac cycles at these time points. Finally, we calculated the longitudinal and circumferential strain from end-diastole to end-systole for each of the three mechanisms at the two post-MI time points and compared the predictions to experimental data.

Figure 2.6 Simulating Full Pressure-Volume Loops

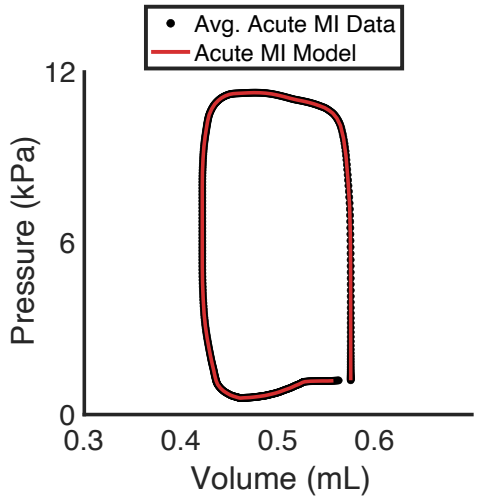

The pressure-volume (PV) loop of the optimized model matches the average acute-MI PV loop.

2.3 Results

2.3.1 Scar Dimension Predictions

At 2 weeks post-MI, the model with reference configuration updates performs the best as both predicted scar dimensions fall within one standard deviation of the mean of the data. The anisotropic kinematic volume loss predicted the scar area ratio to be within the experimental range and the scar thickness ratio to be closer to the data compared to that generated by the isotropic volume loss model. At 6 weeks post-MI the anisotropic kinematic volume loss model and the model reference configuration updates perform relatively the same. The anisotropic model produced a scar area ratio closest to the data range, but the model with reference configuration updates produced a scar thickness ratio closest to the data range. No model produced dimensions that fell within one standard deviation of the data. Based on the results of these simulations, the model with reference configuration updates seemed to be the best performing model.

However, after simulating a biaxial mechanical test in a single scar element pulled from the last iterative step within the model with reference configuration updates (that is, after all reference configuration updates were implemented via new $\boldsymbol{E_1}$ and $\boldsymbol{E_2}$ parameters), the observed stretch-stress behavior was significantly more compliant than the experimental data at the corresponding time point. Therefore, we initialized a stiffer scar and re-ran the entire process in order to end up with a final 6-week scar with appropriate material behavior. The results of this model were similar to those of the isotropic kinematic volume loss model. Consequently, we concluded that the model that best predicts scar dimensions while maintaining physiologically plausible mechanical properties was the anisotropic kinematic volume loss model. The results of these simulations (with mean input parameters) are shown in **Figure 2.7**. The original model with reference configuration updates that resulted in a scar more compliant than what was observed experimentally is shown in green with the “compliant” descriptor in the legend, and the reference configuration update model with scaled scar material parameters is shown in purple with the “stiff” descriptor in the legend.

Figure 2.7 Scar Dimension Predictions

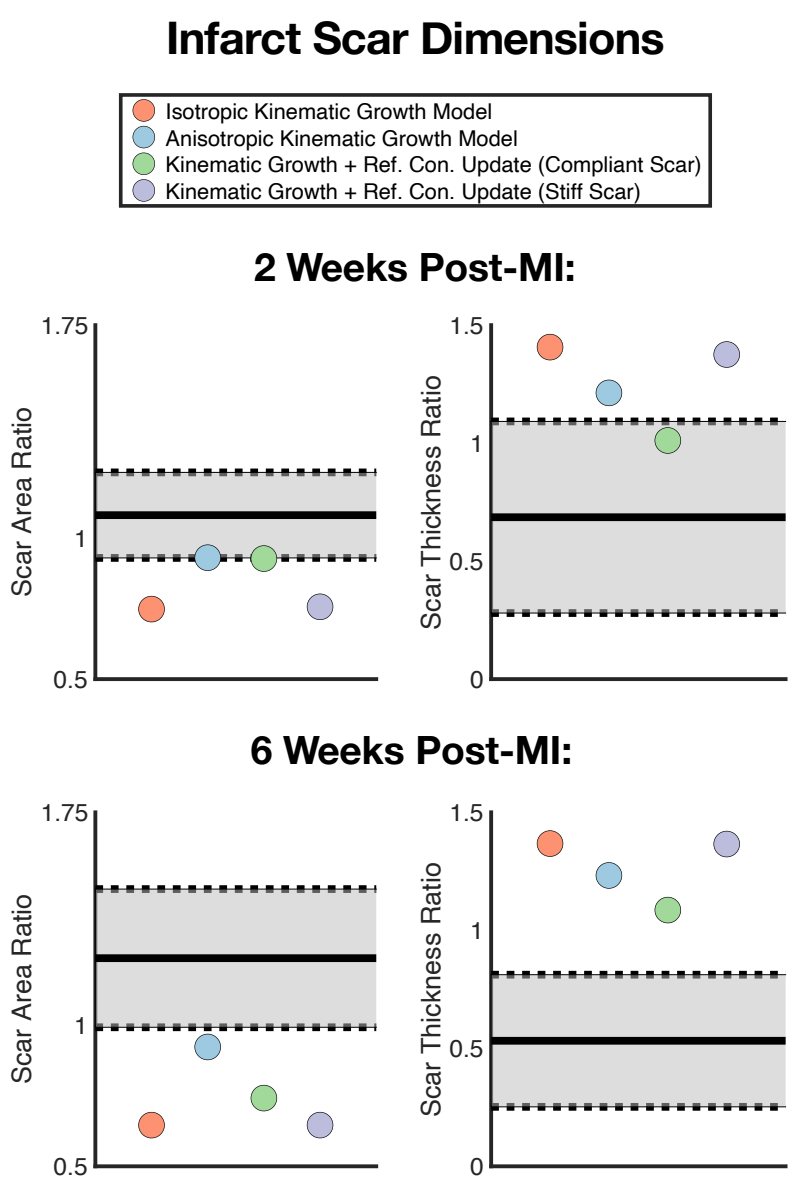

The scar area ratio and the scar thickness ratio as predicted by each model are shown along with the observed, *in-vivo* experimental range. The mean of the data is denoted by the solid black line, and one standard deviation above and below the mean is shaded in gray. The best performing model is the anisotropic kinematic growth model (in blue) as it predicted infarct scar dimensions closest to the observed experimental values.

2.3.2 Sensitivity Analysis Results

The results of the sensitivity analysis are shown in **Figure 2.8.** The model most sensitive to variations in input parameters was the original (compliant) model with reference configuration updates. The input parameter that most influenced the predicted scar dimensions was EDP. This is to be expected as EDP directly affects the loaded configuration of the scar which is equivalent to the prescribed reference configuration updates. Within all other models there is little deviation in predicted scar dimensions when the inputs are altered, though varying scar volume exhibited a noticeable influence on the calculated scar dimensions for these models at 6 weeks.

Figure 2.8 Sensitivity Analysis: Infarct Scar Dimensions

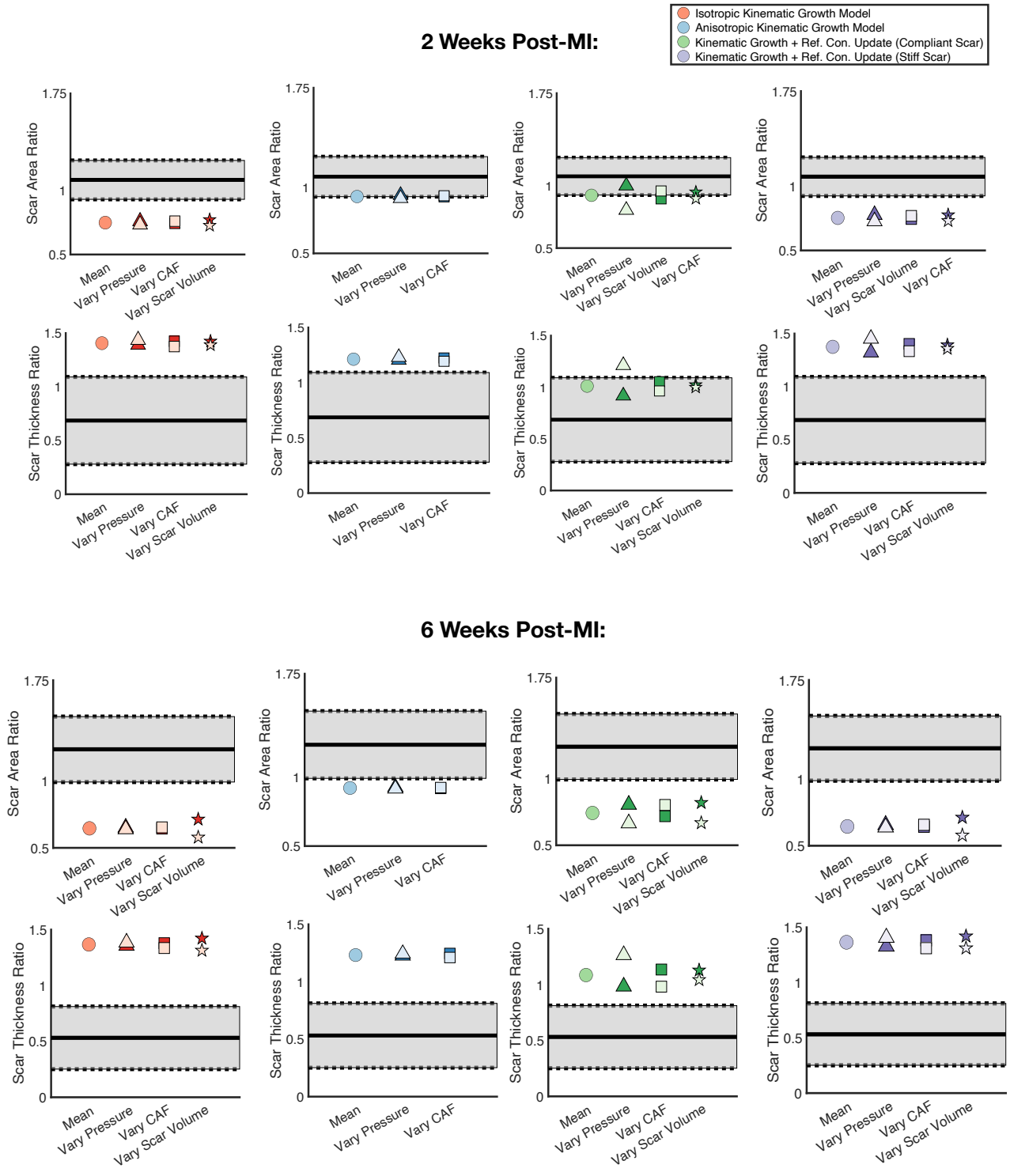

The scar area ratio and the scar thickness ratio as predicted by each model with a varied input parameter are shown along with the observed, *in-vivo* experimental range. The darker data points indicate that the varied parameter was 50% greater than its mean value, and the lighter data points indicate that the varied parameter was 50% less than its mean value.

2.3.3 Systolic Strain Comparison

We calculated the systolic strains at 2- and 6-weeks post-MI for each of the models, and the results are shown in **Figure 2.9**. At 2 weeks post-MI the isotropic kinematic volume loss model performed better than all other models as both the circumferential and longitudinal systolic strains fell near the mean of the data. At 6 weeks post-MI, three models produced circumferential and longitudinal systolic strains within the data range: the isotropic and anisotropic models along with the (stiffer) model with reference configuration updates. However, the strains produced by the anisotropic kinematic volume loss model fell closer to the mean of the data compared to the others. Considering that, for both time points, the anisotropic model predicted loaded scar dimensions closest to the *in-vivo* range (**Figure 2.7**) and produced systolic strains near the data range (**Figure 2.9**), we concluded that it is the model that best captures the geometric remodeling that occurs during post-infarction healing.

Figure 2.9 Systolic Strain Predictions

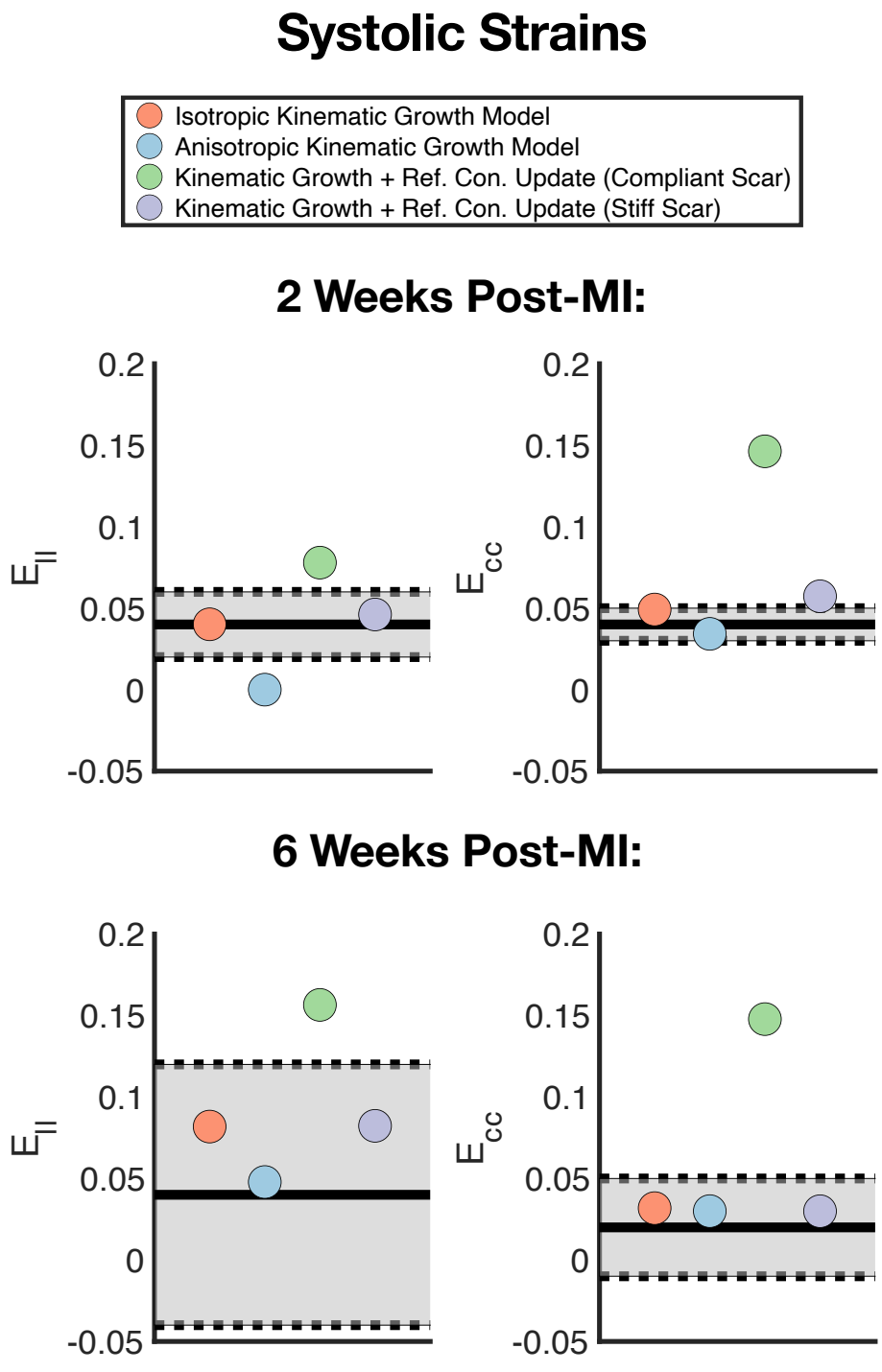

All models except for the one with reference configurations (compliant scar) predicted systolic strains well. The isotropic kinematic volume loss model produced systolic strains within the experimental range (and near the mean) in every case. However, because the anisotropic kinematic volume loss model predicted systolic strains in the data range in most cases and scar dimensions closest to the data range, we considered it the best model overall.

2.4 Discussion

The goal of this chapter was to develop a finite-element model capable of predicting the geometric remodeling that occurs during infarct healing. We constructed three candidate models that accounted for the factors that influence the loaded dimensions of the scar *in-vivo*, which include the end-diastolic pressure (EDP), collagen content/area fraction (CAF), the volume loss due to myocyte resorption, and the reference configuration at which the collagen is deposited in the infarct scar. We used these models to compute scar dimensions and compared the results to experimental data while also calculating the systolic strains to use as independent model validation criteria. We concluded that the anisotropic kinematic volume loss model best captures the geometric remodeling that occurs during post-infarction healing after demonstrating that, for both the 2-week and 6-week post-MI time points, it predicted loaded scar dimensions closest to the *in-vivo* range and produced systolic strains near the data range.

Even though it may be impossible to prove a hypothesis using a model, it is possible to refute one, or at least render it highly unlikely. Perhaps the clearest conclusion from the simulations outlined here is that our original hypothesis – that scar volume loss occurs isotropically, while deformation due to loading creates the apparent in-plane expansion and wall thinning – seems very unlikely to be true. Simulated scars with a stiffness on the same order of magnitude as actual healed rat infarcts simply do not stretch enough when loaded to explain prior observations, even at the elevated diastolic pressures typical post-infarction.

2.4.1 Phenomenologic Approach vs. Mechanistic Approach

While other published models have successfully predicted collagen content and structure throughout the scar remodeling process[43, 56, 57], to our knowledge no model currently exists that is capable of predicting scar dimension changes over time. While our anisotropic growth tensor results in dimensions closest to experimental data, we would not expect this phenomenologic approach to correctly predict infarct remodeling when the mechanics of the infarct are altered, which occurs with a number of therapeutic interventions such as the use of restraint devices or the injection of biomaterials into the infarct[13–15, 46]. Instead, models that consider volume loss plus changes in material properties and loading in combination with evolution of the scar reference state due to collagen turnover may perform better when the ventricular mechanics are altered.

Experiments that track infarct dimensions with and without mechanical interventions are needed to further evaluate the predictive capabilities of the models.

It is striking that some models that fail to accurately predict scar dimensions still correctly predict systolic strains and that the model that correctly predicts scar dimensions fails to predict systolic strain. We believe this finding raises interesting questions about how to model – or even conceptualize – the replacement of muscle by scar in three dimensions. It is not immediately apparent why degrading myocytes and replacing them with collagen and other extracellular matrix should be associated with a change in shape of a region of tissue in its stress-free state, or how load influences that final shape. Modeling at the level of the individual proteins and components may be necessary to understand the packing of these elements in the remodeling and loaded tissue.

2.4.2 Model Limitations

The models constructed within this chapter contain several limitations. First, with respect to the model with reference configuration updates, the unstressed/reference configurations of the scar constituents were updated based on the end-diastolic configuration, that is, we assumed that collagen is deposited only at end diastole. This may not always be the case, and collagen deposition at different time points during the cardiac cycle will influence the scar dimensions. Also, only 15 materials were used to define the solid mixture. Defining more materials within the solid mixture may allow for the healing process to be modeled more smoothly (with smaller steps in collagen content at more closely spaced time points), but computational cost would increase drastically.

A limitation related to the anisotropic model involved the failure of models to converge with anisotropic growth tensors with $F_{g,Fiber}$ greater than 1.12 and $F_{g,Radial}$ less than 0.8. If we were able to successfully implement greater in-plane growth stretches and more wall thinning, we believe we would be able to closely match the data. We made numerous attempts at overcoming this limitation: we increased the density of the FE mesh; we simplified the geometry of the scar; we implemented a gradient of volume change from scar to non-scar elements; we applied different amounts of growth per radial layer within the model; we changed the material of the apical elements from a rigid body to a Mooney-Rivlin material that allowed them to deform; we

tried different material parameters for the myocardium; we decreased the step size in our finite-element solver while also using the Full-Newton method for updating the stiffness matrix, which usually results in better convergence compared to the default method in FEBio but increases computational time. Unfortunately, none of these attempts solved the problem. The most promising approach was the gradient of volume change in which we identified three rings of elements outside the scar and specified volume change to be more continuous from scar to myocardium as shown in **Figure 2.10**. We were able to decrease volume in the radial direction by 40% while no volume loss occurred in the other directions; however, once we tried to apply growth in the fiber and cross-fiber directions, we ran into model convergence issues. We believe that a combination of this volume change gradient and adaptative remeshing (a technique not yet available in FEBio that refines the FE mesh during the simulation) may resolve this issue.

Figure 2.10 Gradient of Growth: Scar Border Zone

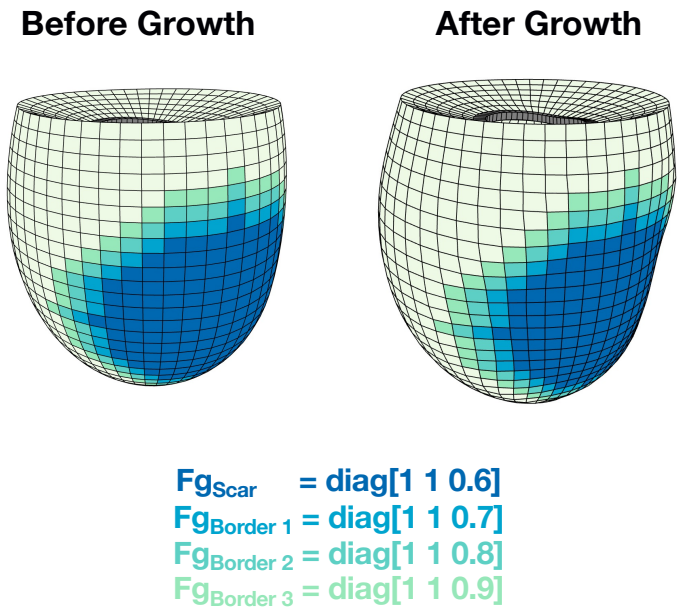

When we implemented a gradient of volume change, in which we identified three rings of elements outside the scar and specified volume change to be more continuous from scar to myocardium, we were able to decrease volume in the radial direction by 40% while no volume loss occurred in the other directions; however, once we tried to apply growth in the fiber and cross-fiber directions, we ran into model convergence issues.

A limitation prevalent to all models involves the way in which the scar material behavior was modeled. The data we used in our modeling of infarct scar was derived from a biaxial mechanical test that elucidated the in-plane deformation of the scar. We did not have data that described the deformation, especially in the radial direction, of the scar within the ventricle. Such information would have been valuable for modeling scar and may have improved scar thickness ratio predictions, though the systolic strains for three out of the four models were accurate. Another limitation common to each of the three models involves the use of only one representative infarct geometry. Infarcts of different size, location, and transmurality may exhibit different loaded dimension changes. Finally, in-plane area ratio is calculated in this study but is compared to normalized in-plane dimension changes from studies that reported a variety of infarct measurements, some of which may contain contributions from the infarct borderzone and remote remodeling.

2.5 Conclusion

Our FE models are the first to predict infarct scar dimension changes over time while incorporating the evolving physiologic processes that occur during infarct healing. Furthermore, our models are the first to explore the factors that originally determine the changes in dimensions and properties, and they help to interpret the reports of scar dimensions during healing. The models also provide the framework to simulate potential therapies aimed at altering the mechanics of the ventricle to prevent adverse remodeling. Our results show that scar volume loss is not isotropic and that accounting for changes in reference state during collagen turnover is not sufficient to prospectively predict dimension changes during healing. Instead, models that can account for how the replacement of necrotic myocytes by collagen and other ECM results in changes in stress-free shape of the infarct will be needed to understand why the scar dimensions change as they do and how those changes will be impacted by potential therapies.

2.6 Appendix

2.6.1 Derivation of Stress for the Fung Orthotropic Material in FEBio

$W = \frac{1}{2}c(e^Q - 1) + U(J) \rightarrow$ Strain Energy Density Function (FEBio User Manual)

$$Q = c^{-1}\begin{bmatrix} (\lambda_{11} + 2\mu_1)E_{11}^2 + (\lambda_{22} + 2\mu_2)E_{22}^2 + (\lambda_{33} + 2\mu_3)E_{33}^2 \\ +2\lambda_{23}E_{22}E_{33} + 2\lambda_{31}E_{33}E_{11} + 2\lambda_{12}E_{11}E_{22} \\ +2(\mu_2 + \mu_3)E_{23}E_{32} + 2(\mu_3 + \mu_1)E_{13}E_{31} + 2(\mu_1 + \mu_2)E_{12}E_{21} \end{bmatrix} \rightarrow \text{Equation (a) in Ex. 1 Ateshian \& Costa}$$

$U(J) = \frac{k}{2}(\ln J)^2 \rightarrow$ Equation (FEBio User Manual)

$p = -\frac{dU}{dJ} = -k\frac{\ln J}{J} \rightarrow$ Equation (In Ateshian & Costa footnote (3)under Equation 32)

$T = -pI + S = k\frac{\ln J}{J} + J^{-1}F \cdot S \cdot F^T \rightarrow$ Cauchy Stress (FEBio User Manual)

$S = \frac{\partial W}{\partial E} \rightarrow$ Second Piola-Kirchhoff Stress as shown in Equation (3) in Ateshian & Costa

Derive each component of stress

$$S_{11} = \frac{\partial W}{\partial E_{11}} = \frac{1}{2}c \cdot e^Q \cdot c^{-1}[2E_{11}(\lambda_{11} + 2\mu_1) + 2\lambda_{31}E_{33} + 2\lambda_{12}E_{22}]$$

$$S_{22} = \frac{\partial W}{\partial E_{22}} = \frac{1}{2}c \cdot e^Q \cdot c^{-1}[2E_{22}(\lambda_{22} + 2\mu_2) + 2\lambda_{23}E_{33} + 2\lambda_{12}E_{11}]$$

$$S_{33} = \frac{\partial W}{\partial E_{33}} = \frac{1}{2}c \cdot e^Q \cdot c^{-1}[2E_{33}(\lambda_{33} + 2\mu_3) + 2\lambda_{23}E_{22} + 2\lambda_{31}E_{11}]$$

$$S_{12} = S_{21} = \frac{\partial W}{\partial E_{12}} = \frac{1}{2}c \cdot e^Q \cdot c^{-1}[2(\mu_1 + \mu_2)E_{21}]$$

$$S_{13} = S_{31} = \frac{\partial W}{\partial E_{13}} = \frac{1}{2} c \cdot e^{Q} \cdot c^{-1}[2(\mu_3 + \mu_1)E_{31}]$$

$$S_{23} = S_{32} = \frac{\partial W}{\partial E_{23}} = \frac{1}{2} c \cdot e^{Q} \cdot c^{-1}[2(\mu_2 + \mu_3)E_{32}]$$

Using **Equation Sets 4** and **7**, the FEBio input parameters can be re-written in terms of the Lamé parameters. All the Lamé parameters (and all FEBio parameters) and ***c*** appear in tensor **S**. If a single material with a given set of material parameters needs to be split into a solid mixture with ***N*** materials, then to match the material behavior of the single material, each of the material properties for the materials within the solid mixture must be divided by ***N*** since FEBio defines the stress response of the solid mixture as the sum of the stress response of each material within it.

Chapter 3

3 Developing a Finite-Element Model of Remote Myocardium Growth Following MI

3.1 Introduction

3.1.1 Ventricular Growth & Remodeling in Disease

Heart function is compromised when one or more conditions alter its normal physiology. These include the conditions in which (1) the mechanical properties of the heart are altered as in viral myocarditis or myocardial infarction (MI), (2) the electrical properties of the heart are altered as in left bundle branch block, and (3) the load placed on the heart exceeds its capabilities as in hypertension. As a result of one or more of these conditions, the physical pump function of the ventricle suffers. At the cellular level, cardiomyocytes experience changes in mechanical stimuli (due to changes in hemodynamics) and receive different hormonal signals from the body. These changes in mechanical and hormonal stimuli interact through a complex network of intracellular pathways and drive the cells to respond by increasing sarcomeric protein synthesis and growing in size[19, 54]. This cellular remodeling leads to different patterns in the growth of the ventricle.

There are two common patterns of ventricular growth, or hypertrophy: concentric and eccentric[6, 58–63]. Concentric hypertrophy occurs due to increased afterload, such as pressure overload, which causes the wall of the left ventricle (LV) to thicken because sarcomeres are added in parallel within the cardiomyocyte as it thickens. On the other hand, eccentric growth occurs due to increased preload, such as volume overload, where the ventricle dilates as sarcomeres are added in series and lengthen cardiomyocytes. For example, MI places a volume overload on the heart, which forces the heart to pump higher volumes of blood at relatively normal pressures. This overload elicits eccentric hypertrophy, and the circumference of the LV increases more rapidly than the wall thickness, which results in dilated heart failure and eventual death[64, 65]. While the mechanism that determines exactly how hypertrophic signaling results in either cardiomyocyte thickening (in concentric hypertrophy) or in cardiomyocyte lengthening (in eccentric hypertrophy) is still unknown[58, 66], phenomenologic models that use mechanics (stress

or strain) to predict these patterns of cardiac growth have been successful[20, 22, 54, 59–61, 67–76]. Currently, numerous models exist that can correctly predict the patterns of growth due to different mechanical perturbations. These models have advanced the current state of cardiovascular research such that computational modeling can be plausibly utilized in the clinic to predict the time course of heart growth and remodeling in individual patients. The models' predictive capabilities may also be useful in designing effective interventions and therapies for various types of heart disease.

3.1.2 Mechanical Signals of Growth & Previous Models

Numerous models have proposed different mechanical signals, such as stress or strain, that can drive growth and have also utilized them to successfully predict hypertrophy. These mechanical signals are input into "growth laws," equations used to relate mechanical stimuli (deviations in mechanical signals from baseline values) to the amount and direction of growth expected from experimental data[59, 61, 70, 77]. Growth laws operate under the assumption that growth adaptations drive the signal back towards a homeostatic value; therefore, they prescribe larger amounts of growth in response to larger stimuli. In 1975, Grossman et al. theorized that the wall thickness of the ventricle increases in pressure overload to normalize systolic stress[78]. This hypothesis was based on the observation that patients with aortic stenosis, a form of pressure overload, exhibited peak systolic stresses similar to those of healthy patients; the sick patients had normal peak systolic stresses because the wall thickness of their ventricles offset the elevated ventricular pressure. Grossman concluded that concentric hypertrophy may be driven by systolic wall stress. Motivated by this finding, many models have been developed using stress as the stimulus for growth and have successfully captured growth trends during development, pressure overload, and even significant amounts of exercise[70, 77].

On the other hand, Emery and Omens argued that diastolic strain is the main driver of eccentric growth[79]. They discovered that wall stresses in rats remained elevated during eccentric hypertrophy, yet diastolic strains returned to normal at the end of 6 weeks. Emery and Omens concluded that strain, as opposed to stress, is a more appropriate signal for eccentric growth. Inspired by this finding, many models have used strain as the mechanical stimulus for growth to predict hypertrophy during volume overload and even post-natal heart growth[20, 22, 59, 61, 80]. Recent models have used these strain-based growth laws to predict chamber dilation in response to MI

and ventricular dyssynchrony. Impressively, Kerckhoffs et al. developed a law that was able to predict growth in response to both pressure and volume overload with a single set of growth parameters while also predicting regional differences in growth due to simulated dyssynchrony[61, 81]. Although this model agreed with experimental data *qualitatively*, Witzenburg and Holmes further implemented a version of the Kerckhoffs growth law and, using a single set of growth parameters, *quantitatively* matched canine ventricular growth data due to pressure overload, volume overload, and MI[20].

3.1.3 Factors Affecting Post-MI Remote Growth: Scar Size, Scar Stiffness, and End-Diastolic Pressures

While eccentric hypertrophy is the typical pattern of growth that follows myocardial infarction, factors such as the size and stiffness of the infarct scar and the degree to which the infarction increases end-diastolic pressure (EDP) may contribute individually, or in combination, to ventricular growth as each of these factors alters diastolic strain. Pfeffer et al. previously showed that large infarcts significantly raised EDP[31]. An elevated EDP increases diastolic strain and results in eccentric growth, yet it is not clear whether infarct size or EDP is the more significant factor in driving growth. Additionally, infarct size and stiffness may have a secondary impact on diastolic strains as these factors can change the overall size of the LV at a given EDP, which alters wall stress leading to changes in end-diastolic strain.

Currently, there are no experiments or models that have clearly separated the effects of hemodynamics (changes in EDP), scar size, and scar stiffness on ventricular growth following MI. Moreover, factors such as hemodynamics and scar stiffness change throughout infarct healing and must be considered when predicting growth in the remote myocardium. Therefore, in this chapter, we build a finite-element (FE) model of volume overload in the rat. We choose a strain-based growth law and tune its parameters to match experimental volume overload growth data in the absence of MI. We then use these parameters to predict growth in a model with infarction while varying infarct size, stiffness, and EDP to determine the main driver of growth. Finally, we predict growth in the remote region in the FE model from the previous chapter in which EDP, scar stiffness, and scar volume vary over time and compare our results to data generated in our lab. This results in the most comprehensive model to date of post-MI ventricular

remodeling, which allows for the prediction of ventricular growth following potential therapies, such as biomaterial injection within the infarct region and mechanical reinforcement of the infarct.

3.2 Methods

3.2.1 Growth Law Selection & Parameter Fitting for Non-MI Volume Overload

To predict growth in the remote myocardium of rats, we first selected a growth law that has been previously used to capture experimental growth patterns in the heart. Following MI, the cardiomyocytes primarily lengthen in their fiber direction, leading to progressive cavity dilation. Many growth laws define the stimulus for growth in the fiber direction as a function of the difference between the maximum fiber strain in the overloaded condition and the maximum fiber strain in the homeostatic state. In particular, the growth law implemented by Witzenburg and Holmes used this stimulus for fiber and cross-fiber growth, along with a function defining growth in the radial direction, to successfully predict the observed growth patterns in the myocardium due to pressure overload, volume overload, and MI[20]. We implemented the growth law for the fiber and cross-fiber direction, shown in **Equation 1A** and **1B**, in our FE model.

Equation 1A shows that the stimulus for growth along the fiber direction of the cardiomyocytes (s_l) was driven by the difference between the maximum fiber strain (E_{ff}), which occurs at end-diastole, and the homeostatic setpoint ($E_{f,set}$) at which no growth occurs. **Equation 1B** is the is the sigmoidal function for the incremental growth component in both the fiber ($F_{g,f}^{i+1}$) and cross-fiber ($F_{g,c}^{i+1}$) directions. The parameter $f_{ff,max}$ defines the maximum amount of growth allowed in a single step. The slope of the sigmoid is specified by f_f, and the parameter $s_{l,50}$ defines a small nearly quiescent region where no growth occurs. We kept $f_{ff,max}$ at the same value reported by Witzenburg and Holmes and tuned the parameters f_f, and $s_{l,50}$ to fit experimental volume overload growth data in the absence of MI. We chose to not prescribe growth in the radial direction as volume overload results in lengthening/growth primarily in the fiber and cross-fiber directions of cardiomyocytes.

$$s_l = \max(E_{ff}) - E_{f,set} \qquad \textbf{Equation 1A}$$

$$F_{g,f}^{i+1} = F_{g,c}^{i+1} = \begin{cases} F_{g,f}^{i} \cdot \sqrt{\dfrac{f_{ff,max}}{1 + \exp\left(-f_f \cdot \left(s_l - s_{l,50}\right)\right.} + 1} & s_l \geq 0 \\ F_{g,f}^{i} \cdot \sqrt{\dfrac{-f_{ff,max}}{1 + \exp\left(f_f \cdot \left(s_l + s_{l,50}\right)\right.} + 1} & s_l < 0 \end{cases} \qquad \textbf{Equation 1B}$$

$$F_{g,r} = 1$$

We first simulated normal inflation in our FE model of the rat LV by applying a healthy end-diastolic pressure of 0.69 kPa. At this loaded state, we calculated the elastic fiber stretches of every element, averaged these stretches, and set the resulting value as the homeostatic setpoint ($E_{f,set}$) at which no growth occurs. Next, we simulated volume overload by passively inflating our FE model to an elevated end-diastolic pressure of 1.1 kPa, which is approximately 63% greater than the control EDP. At the loaded state, we again calculated the average of the elastic fiber stretches of each element and used this value as $\max(E_{ff})$ in **Equation 1A** to compute the growth stimulus to calculate the incremental growth component for both the fiber ($F_{g,f}^{i+1}$) and cross-fiber ($F_{g,c}^{i+1}$) directions for a given $f_{ff,max}$, f_f, and $s_{l,50}$. Then, we applied these incremental growth values to our FE model with the material plug-in developed in the previous chapter, inflated the model to the same overloaded EDP of 1.1 kPa, and simulated 8 weeks of growth with step sizes of one day. We used the $f_{ff,max}$ value reported by Witzenburg and Holmes, and tuned f_f, and $s_{l,50}$ until our predicted growth matched the experimental growth trends[82].

3.2.2 Elucidating the Relative Impact of Scar Size, Scar Stiffness & End-Diastolic Pressure on Post-Infarction Growth in the Remote Myocardium

To understand the effects of scar size, scar stiffness, and EDP on ventricular growth following MI, we used the growth law with the optimized parameters from the previous section to predict hypertrophy in the remote myocardium region while varying these factors. We constructed an FE model for every combination of the following input variables: small (10% of LV wall volume), intermediate (30%), or large (53%) infarct scar, which fell within the size ranges as described by

Pfeffer et al.[31]; collagen area fractions (CAF) of 0%, 13.3%, or 33.3% which produced different scar stiffnesses[28, 29]; and high (3.5 kPa), intermediate (1.5 kPa), or low (0.8 kPa) EDP, which were also observed by Pfeffer et al.[31] We simulated and compared the growth rate during the first three days of volume overload among all the models.

For each simulation, we calculated and prescribed growth within the remote region in a similar manner as was done in the previous section. We first simulated normal inflation in our FE model by applying the healthy end-diastolic pressure of 0.69 kPa. At this loaded state, we calculated the average of the elastic fiber stretches of the elements within the remote region (i.e., not scar). Next, we simulated post-infarction diastolic mechanics by passively inflating our FE model to the prescribed EDP with the prescribed scar size and CAF. At the loaded state, we calculated the average of the elastic fiber stretches of all remote myocardium elements and computed and applied the incremental growth. We simulated 3 days of growth, iterating with a growth step of one day (i.e., re-inflating the LV and re-calculating strains at each step), and quantified the initial growth rate for each combination of factors.

3.2.3 The Comprehensive MI Model: Scar Remodeling + Remote Growth

Our final simulation integrated the FE model of scar healing from the previous chapter with the FE model of remote myocardium growth. This combined model accounts for the interplay between post-MI remodeling processes, in which the infarct scar volume and stiffness, along with EDP, vary over time while the remote region remodels. To simulate the effects of scar healing on remote growth, we prescribed the time course of infarct healing from acute MI with a scar size of 30% to 4 weeks post-MI in our FE model. At the acute state, we prescribed an EDP of 1.18 kPa with neither volume loss within the infarct region nor infarct stiffening. Using the same method from the previous section, we calculated and applied incremental growth for 7 days. At the end of 7 days, we increased EDP to 1.27 kPa, decreased scar volume by 4%, and prescribed a collagen area fraction of 20% by updating the material parameters of 3 out of the 15 materials within the solid mixture as demonstrated in the previous chapter. We again calculated and applied incremental growth for 7 days. This process, outlined in **Figure 3.1**, was repeated with the appropriate input scar healing parameters until 4 weeks of growth was simulated. Finally, we compared the growth predicted by our simulation to the growth observed in the same experimental data set from which we calculated the scar healing parameters[28].

Figure 3.1 Outline of the Comprehensive MI Model: Scar Remodeling + Remote Growth

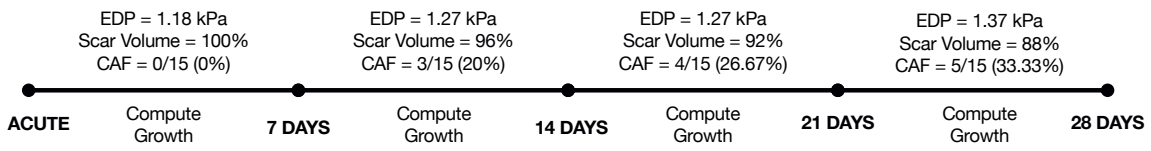

The input parameters of the scar remodeling FE model from the previous chapter are updated every 7 days for 28 days while the growth within the remote region is calculated and applied each day for 28 days.

3.3 Results

3.3.1 Growth Law Tuning & Predicting Growth in Non-MI Volume Overload

Witzenburg and Holmes optimized their growth law parameters to match experimental growth in canines and determined that the optimal values for the parameters f_f and $s_{l,50}$ were 31 and 0.215, respectively. Because our goal was to predict hypertrophy in rats, we re-optimized the parameters to match rat-specific data. We performed a parameter sweep during which we ran 8 weeks of growth for every combination of growth parameters within the following ranges: $f_f = [10, 20, 30, 40, 50, 60, 70, 80]$ and $s_{l,50} = [0.1, 0.2, 0.3]$. The optimal values for f_f and $s_{l,50}$ were 80 and 0.1, respectively, and the resulting simulated time course of growth using these parameters is shown in **Figure 3.2A**. Our model results fell within the experimental ranges of growth at 1, 2, 4, and 8 weeks post-volume overload[82].

In **Figure 3.2B** the black line illustrates the sigmoidal shape of the stimulus-growth stretch curve specified by our growth law with the optimized rat parameters. The dots represent the stimuli and the incremental growth stretch for each step in the simulation with the darker dots representing early time points and the lighter dots representing later time points. The first growth step is the highest, most-purple dot on the sigmoid and depicts the largest increase in growth due to the largest stimulus (i.e. the largest difference between the overloaded fiber strain value and the homeostatic setpoint). The last growth step, represented by the lowest, most-yellow dot depicts the smallest increase in growth as the stimulus is the smallest due to accumulated growth that has slightly decreased the end-diastolic elastic fiber strain in the overloaded case. The end-diastolic elastic fiber strain throughout growth is shown in **Figure 3.2C**. Overall, fiber

strain slightly decreased and nearly plateaued because the incremental growth value ($F_{g,fiber\text{-}i}$) reached an approximate final value of 1. Finally, **Figure 3.3** shows the configurations at matched EDP of the LV before growth (left) and after 8 weeks of growth (right).

Figure 3.2 Predicting Growth in Non-MI Volume Overload

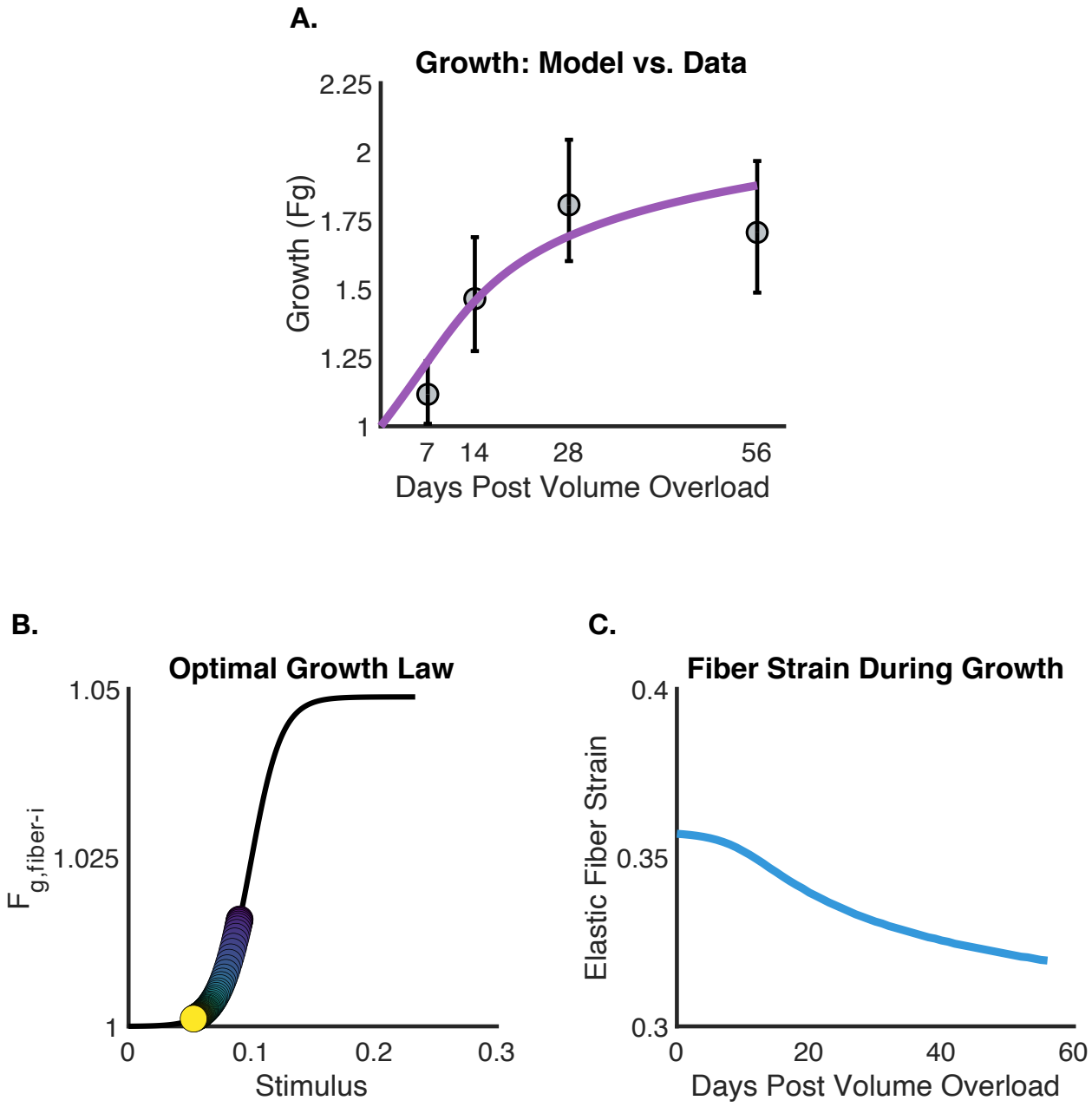

(A) With the optimal growth law parameters, the simulated growth (purple line) due to volume overload in the absence of MI fell within the experimental range at all time points. (B) The incremental growth stretch and stimuli for each growth step were plotted on the sigmoidal growth curve and demonstrated more growth at the earlier time points (darker dots) and less growth at the later time points (lighter dots). (C) The elastic fiber strain decreased slightly over time and nearly plateaued because the incremental growth value ($F_{g,fiber\text{-}i}$) reached an approximate final value of 1.

Figure 3.3 FE Model of Non-MI Volume Overload

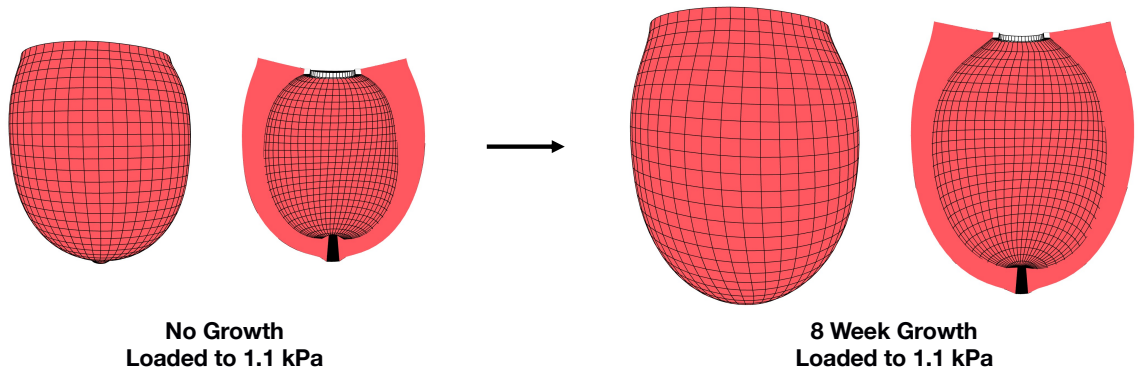

The configurations of the FE models at matched EDP of the LV before growth (left) and after 8 weeks of growth (right) are shown.

3.3.2 Factors Influencing Growth Following MI

With the optimized growth law parameters, we ran growth simulations in models with simulated infarcts. Infarcts varied in size (small, moderate, and large) and stiffness (CAF = 0, 13.3, or 33.3%) while EDP also varied (high, intermediate, and low). We constructed a model for every combination of the aforementioned factors and simulated 3 days of growth with each model to determine how each factor affected growth. **Figure 3.4** shows the results of all 27 simulations. For each of the three infarct sizes simulated, rows present simulations at a given EDP (increasing from bottom to top) while the columns reflect simulations at a given infarct stiffness (increasing from left to right). The growth curves are shown in black, and the background of the plots are colored based on the magnitude of growth on the third/final day, with darker green representing more growth.

We determined that the main driver of predicted growth within our models was the end-diastolic pressure. No matter the infarct size or stiffness, the growth increased the most as EDP increased (bottom to top). For models inflated to the largest EDP, the amount of growth at 3 days was similar for each infarct stiffness except in the case of the large scar, in which the growth decreased slightly with stiffening. For models inflated to the intermediate EDP, scar stiffness played a more significant role in growth. As the infarct became stiffer, less growth occurred because the increase in stiffness hindered the ventricle's ability to inflate and deform. For models

inflated to the lowest EDP, nearly no growth was observed no matter the size of the infarct nor its stiffness. This pressure resulted in stimuli values on the near-quiescent portion of the growth curve.

Figure 3.4 Drivers of Growth Following MI: Effect of Scar Size, Stiffness, and EDP

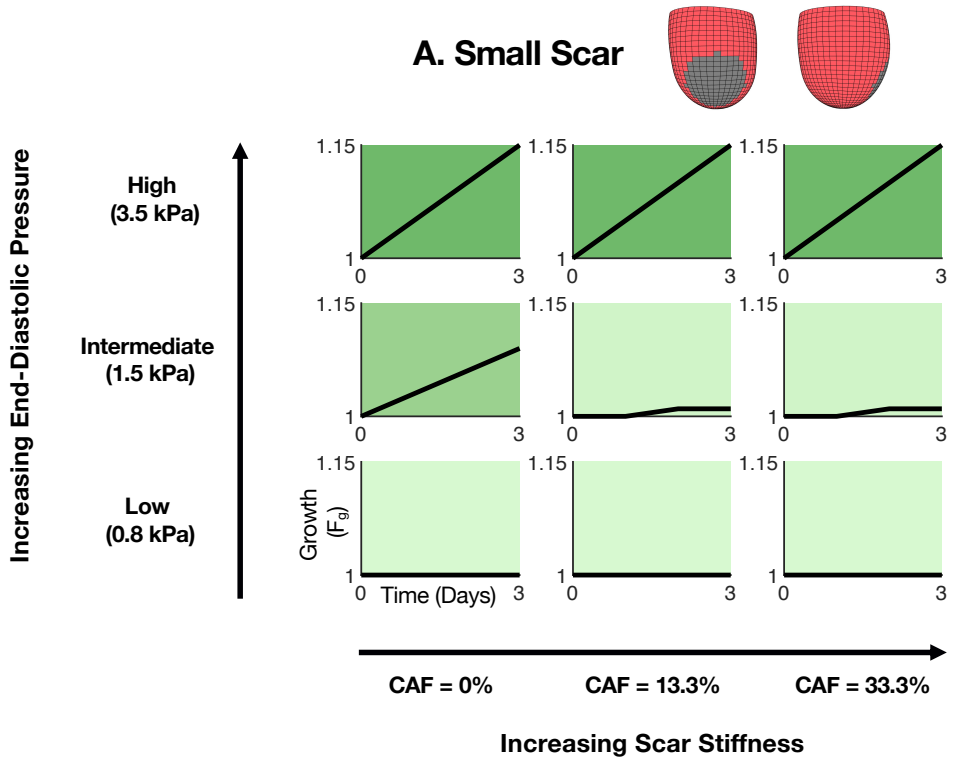

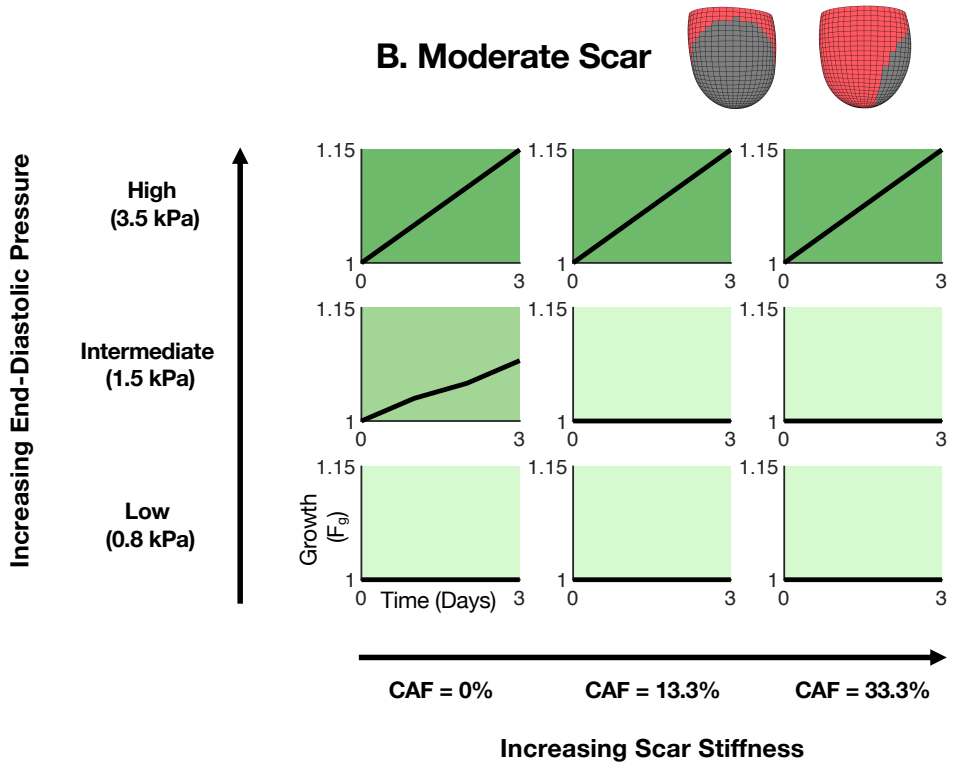

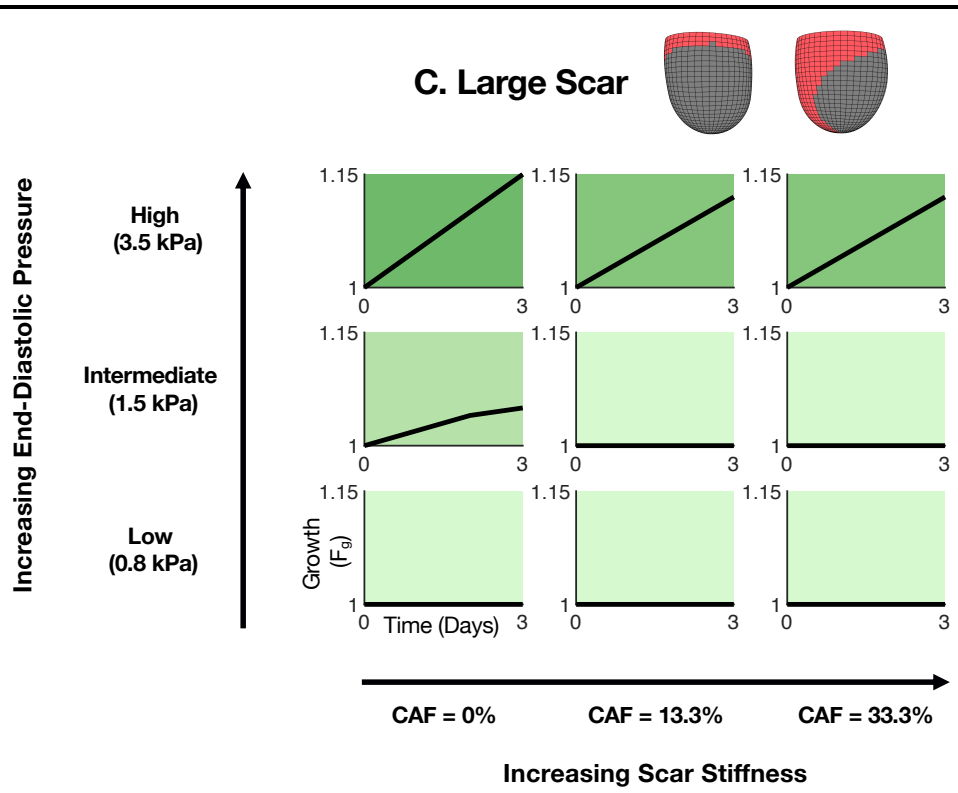

Across all infarct sizes, there was more change in growth (differences in the shades of green) from the top to bottom of the nine plots rather than from left to right, indicating that elevated EDP has a much greater effect on predicted growth than changes in infarct stiffness. The amount of predicted growth for a given EDP and infarct stiffness was also similar for all infarct sizes, suggesting that infarct size per se has little effect on growth, though slightly less growth occurs in larger infarcts. For models inflated to the intermediate EDP, scar stiffness played a more significant role in growth.

3.3.3 Scar Remodeling and Remote Growth Match Experimental Data

In our final model, we implemented the changes that occur over time within the infarct during post-MI healing and computed growth within the remote myocardium. This model incorporated elements from both the previous and current chapters. We accounted for changes in infarct scar volume, stiffness, and end-diastolic pressure while we also computed and prescribed the growth within the remote region. The results of our simulation fell within the experimental data range as shown in **Figure 3.5A**. Most of the growth occurs within the first week post-MI as EDP is elevated with no increase in stiffness within the infarct region. However, even as EDP remained elevated (see **Figure 3.1**), growth was nearly halted after 1 week as the infarct scar stiffened over time. **Figure 3.5B** and **Figure 3.5C** explain this result in terms of the stimulus, incremental growth, and fiber strain. In the first 7 days following MI, the fiber strain is elevated, and the stimuli (represented by the dark dots) are large enough to cause growth. At 7 days post-MI, there is a sudden decrease in fiber strain and corresponding downward jump on the growth curve (**Figure 3.5B**). The stiffening of the infarct is responsible for this decrease in fiber strain and reduction in growth. At this time point in the simulation, the infarct is stiffened and the EDP is increased. Larger EDPs increase fiber strain, yet the stiffness of the infarct prevented this. This trend continues throughout the remaining time points and results in stimuli on the quiescent portion of the growth curve. The infarct in this model fell within the ranges of EDP and stiffness in which stiffness affects growth as shown previously in **Figure 3.4** (middle rows).

Figure 3.5 Predicting Growth in the Comprehensive MI Model

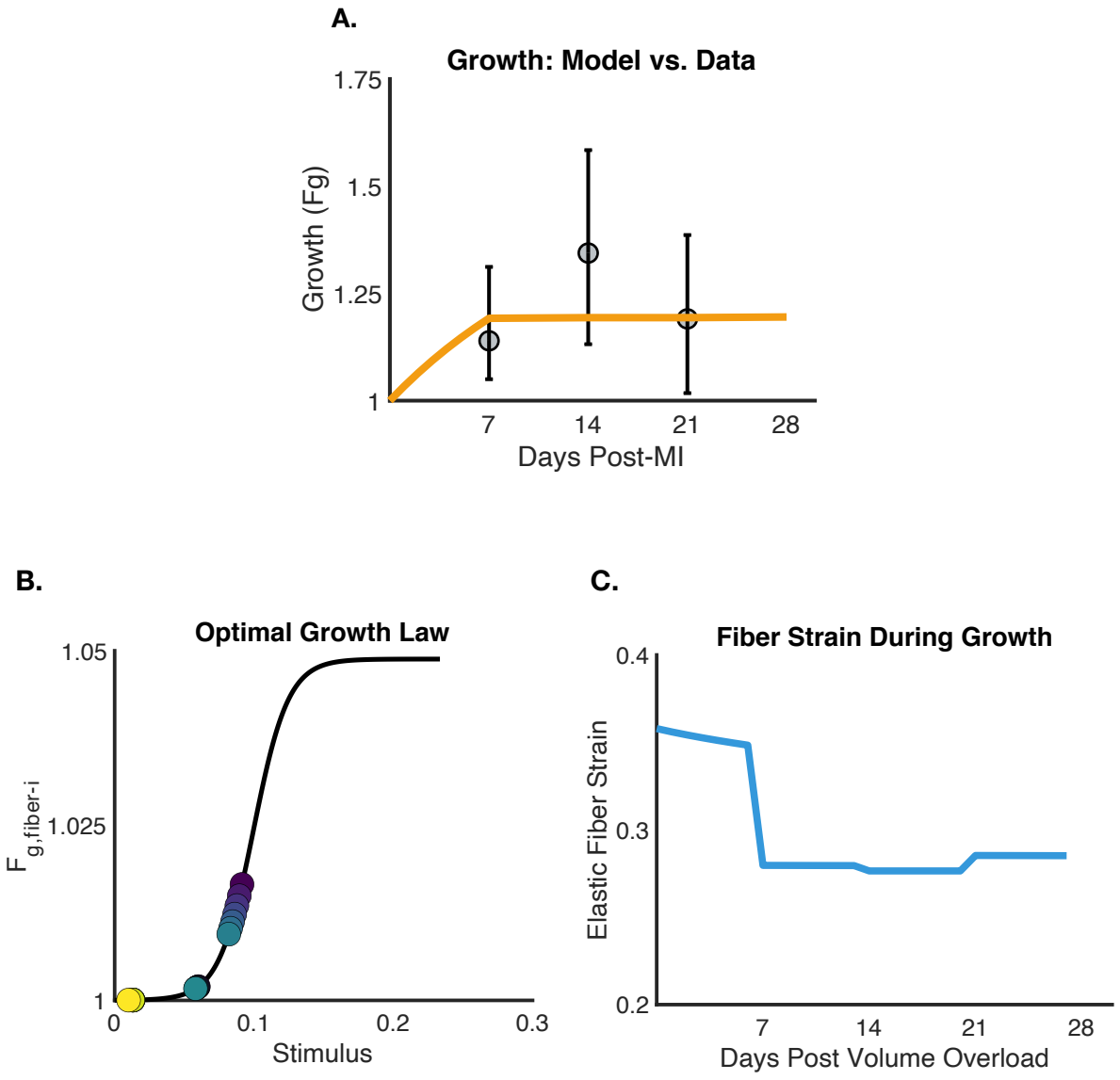

(A) After accounting for the changes that occur over time during infarct healing (changes in scar volume and stiffness along with fluctuations in EDP) and computing growth in the remote non-infarcted region, the results of our simulation fell within the experimental data range. (B) There were jumps along growth curve as the infarct stiffened over time; initially, in the presence of no stiffening, the stimulus and resulting growth were large (darker purple-green dots). However, when the infarct became stiffer, there was a downward jump on the growth curve, resulting in nearly no incremental growth. (C) The fiber strain was large before stiffening and decreased as the infarct was stiffened.

3.4 Discussion

3.4.1 Stability of Heart Growth

Using the growth law developed by Witzenburg and Holmes, our initial simulations of cardiac hypertrophy following volume overload demonstrate that our model continues to grow at later times when the experimental data plateaus (**Figure 3.2A**). One way of modifying our growth law to better match the data involves the implementation of an evolving homeostatic setpoint. An evolving homeostatic setpoint allows the myocardium to gradually adjust its state at which no growth occurs rather than using one fixed value ($E_{f,set}$ in **Equation 1A**). These adjustments result in setpoints closer to the growth stimulus, thus decreasing the amount of growth.

Yoshida et al. recently implemented an involving setpoint that improved predictions of the regression of cardiac growth following the release of pressure overload while still allowing appropriate predictions of the initial 'forward' growth due to overload[22]. The authors used a weighted moving average of the elastic strains from the previous 15 growth steps (2 weeks) to specify the current setpoint. This average was based on the biological observation that the half-life of assembled actin and myosin in cardiac sarcomeres is 1 week[83]. The elastic strain from 8 growth steps prior to the current time was weighted most heavily, with strains from more recent and more distant time points exerting less influence on the setpoint. This equation is shown in **Equation 2**. To examine the effect of an evolving setpoint on the growth predicted in our simulations, we implemented the same assumptions and re-ran our volume overload simulations from **Figure 3.2**. Our results are shown in **Figure 3.6**. The evolving setpoint blunted growth and allowed the LV to reach a steady size but did so prematurely. The new setpoints were larger than the original homeostatic setpoint and similar in value to the growth stimuli, so no growth nor change in fiber strain occurred after the new setpoints were engaged at day 15. Applying evolving setpoints in the infarct models was not necessary to match the trends in experimental data (**Figure 3.5A**), yet they warrant further investigation as they offer a more biologically-grounded basis for the approach to a new ventricular steady state and have already proven more effective at simulating treatments that reduce hemodynamic overload.

$$E_{f,set}^{i} = \frac{1}{64}\max\left(E_{ff}^{i-15}\right) + \frac{2}{64}\max\left(E_{ff}^{i-14}\right) + \frac{3}{64}\max\left(E_{ff}^{i-13}\right) + \frac{4}{64}\max\left(E_{ff}^{i-12}\right) + \frac{5}{64}\max\left(E_{ff}^{i-11}\right) + \frac{6}{64}\max\left(E_{ff}^{i-10}\right) + \frac{7}{64}\max\left(E_{ff}^{i-9}\right) + \frac{8}{64}\max\left(E_{ff}^{i-8}\right) + \frac{9}{64}\max\left(E_{ff}^{i-7}\right) + \frac{10}{64}\max\left(E_{ff}^{i-6}\right) + \frac{11}{64}\max\left(E_{ff}^{i-5}\right) + \frac{12}{64}\max\left(E_{ff}^{i-4}\right) + \frac{13}{64}\max\left(E_{ff}^{i-3}\right) + \frac{14}{64}\max\left(E_{ff}^{i-2}\right) + \frac{15}{64}\max\left(E_{ff}^{i-1}\right)$$

Equation 2

Figure 3.6 Implementing the Evolving Setpoint

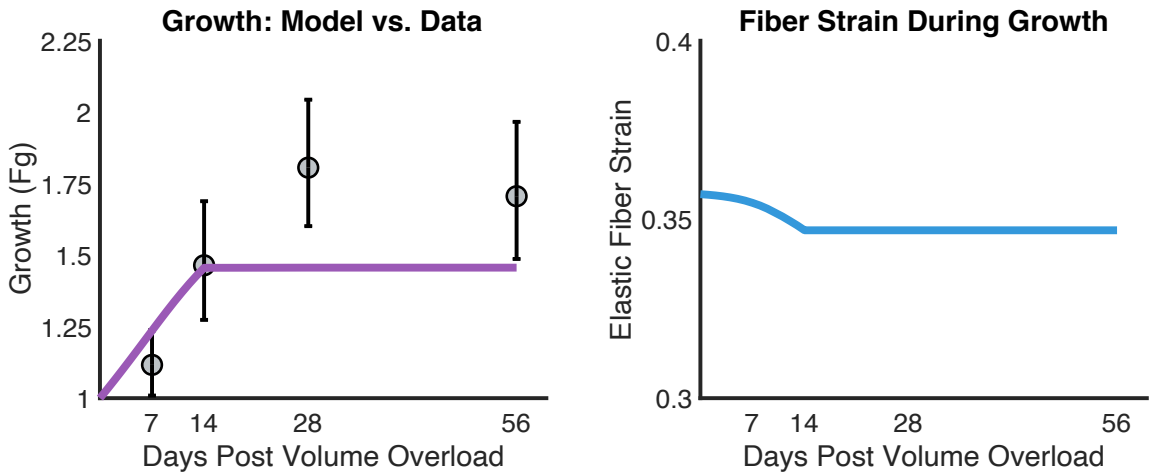

The evolving setpoint blunted growth and allowed the LV to reach a steady size but did so prematurely, matching trends at 1 and 2 weeks post-volume overload but underestimating growth between 4 and 8 weeks post-volume overload. The new setpoints were larger than the original homeostatic setpoint and similar in value to the growth stimuli, so no growth nor change in fiber strain occurred after the new setpoints were engaged at day 15.

3.4.2 Effect of Infarct Stiffness on Growth Following MI

The main driver of predicted growth within our models was the end-diastolic pressure. No matter the infarct size or stiffness, the growth increased the most as EDP increased. However, for models inflated to an intermediate EDP, scar stiffness played a more significant role in growth. In **Figure 3.7**, we plotted the transmural fiber strains in models at a matched EDP of 1.5 kPa with (A) no stiffening and (B) stiffening that represents a CAF of 33.3%. This figure shows that the remote myocardium in the model with the stiffer infarct (B) undergoes less fiber strain (darker colors) compared to the model with no stiffening, especially adjacent to the infarct and near the epicardium. As the infarct becomes stiffer, less growth occurs because the increase in stiffness impedes the ability of those regions deform in the fiber direction. Overall, the differences are not as large as expected after considering the differences in predicted growth. This suggests that the fitted growth law is sensitive to very small changes in stimulus (i.e., steep sigmoid). Additionally, the average elastic fiber strain of all the non-infarcted elements is input into the growth law. The smaller strains that occur adjacent to the infarct and around the epicardium drive that average down enough to result in a small stimulus with less growth. Prescribing growth element by element may help confirm the effect that infarct stiffness impedes growth.

Figure 3.7 Remote Fiber Strain in FE Models: Non-Stiff Infarct vs. Stiff Infarct

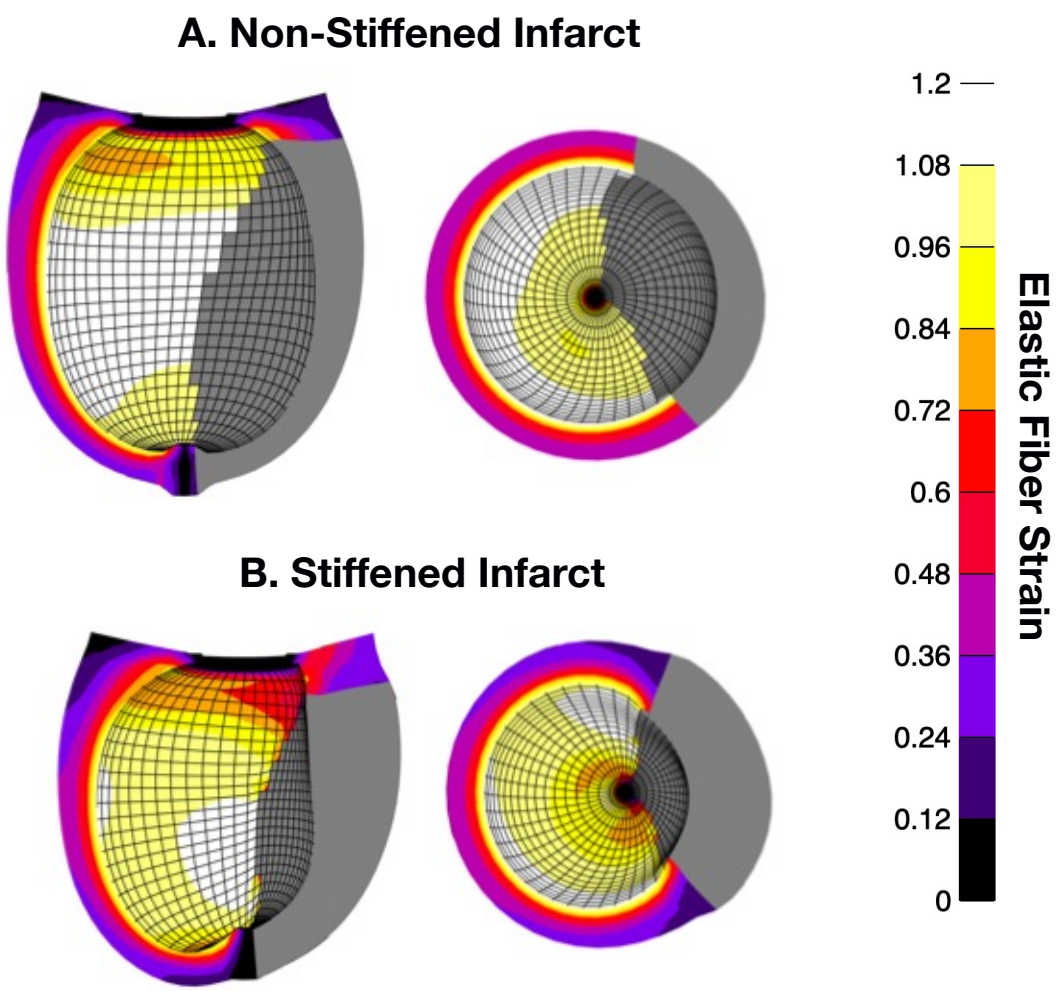

This figure shows that the remote myocardium in the model with the stiffer infarct (B) undergoes less fiber strain (darker colors) compared to the model with no stiffening (A), especially adjacent to the infarct and near the epicardium.

3.4.3 Accounting for the Effects of Evolving Hemodynamics, Hormones & Drugs

We determined that end-diastolic pressure, rather than scar size or stiffness, was the biggest driver of cardiac hypertrophy within the infarct models. However, EDP is related to infarct size as Pfeffer et al. demonstrated that, in a rodent model with large infarcts (>53% by LV wall volume), the EDP was nearly 5 times larger than the EDP for moderately sized or small infarcts. The hemodynamic changes that occur following a large infarct greatly affect EDP and induce substantial growth. Our finding highlights the importance of correctly modeling hemodynamics as an essential step in predicting heart growth. In fact, other groups have drawn similar conclusions. For example, in the case of dyssynchrony caused by left bundle branch block, Kerckhoffs et al. were able to match experimentally reported growth only when they accounted for the hemodynamic compensations that maintained a constant mean arterial pressure[81]. Additionally, a recent study from our group utilized a compartmental model that included complex hemodynamic changes to accurately predict the time course of heart growth[20]. Realistic models of the evolution of the hemodynamic loads placed on the heart may not only be important for modeling ventricular response to injury, but they may also be necessary to predict the effect of potential therapies that affect hemodynamics.

While we somewhat accounted for changes in hemodynamics as variations in EDP, we did not explore the effects of hormones and drugs on growth. At the cellular level, cardiomyocytes grow due to perturbations within the complex intracellular signaling network. Hormones and drugs, as well as mechanical stimuli, can perturb this network and cause hypertrophy. Several hormones or drugs that stimulate key hypertrophic pathways can cause cardiomyocyte growth even in the absence of altered mechanical stimuli[19]. Ryall et al. constructed a computational model of the intracellular signaling pathways within cardiomyocytes and showed that the pathways activated by mechanical stimuli (stretch) overlap with those that respond to hormones and chemokines associated with hypertrophy[19]. Furthermore, experiments such as aortic banding, which is a form of pressure overload, are often used to calibrate growth models and alter not only heart mechanics but also the levels of many hypertrophy-associated hormones[84–90]. Our group recently constructed a multiscale model that connected an FE model of concentric growth to a cell-level network model of hypertrophic signaling pathways accounting for changes in both mechanics and hormones[54]. The model was able to match growth caused by isoproterenol infusion (i.e., a drug that alters the gene

expression of hypertrophy-associated genes) and transverse aortic constriction (i.e., a mechanical intervention that increases aortic pressure and generates pressure overload) along with the attenuation of growth caused by other genetic and pharmacologic interventions. The most striking conclusion of the model was that the hormonal inputs were responsible for most of the growth. These findings suggest that models relying solely on the kinematic framework for growth with dependence only on changes in mechanics may perform poorly when changes in the hormonal environment occur. Since many therapies aimed at preventing the progression of heart growth or reversing it alter hormones in the form of drugs, mechanical models of growth like the one presented in this chapter may need to be expanded to capture the hormonal response along with the mechanical response.

3.4.4 Model Limitations

The major limitation of the model presented in this chapter is that it does not account for more complex changes in hemodynamics or hormonal and drug activity. However, our model still fits the observed growth data in the case of volume overload with the absence of MI as well as the case of growth caused by MI. We expect that our model can predict growth trends following potential therapies that primarily alter mechanics, such as mechanical reinforcement or biomaterial injection. However, we cannot currently simulate the effects of drugs that alter the hormonal environment and thus cannot predict the effects of drug interventions. Another limitation includes our assumption that growth in the radial direction of the cardiomyocytes does not occur. While experimental data show that the most prominent pattern of growth following MI is dilation (i.e. growth in the fiber and cross-fiber directions), some data demonstrate modest growth in the radial direction. Also, if growth in the radial direction is sufficient, the growth in our model may better fit the data (i.e. simulated growth may plateau like the experimental growth). Therefore, it may be advantageous to implement radial growth within our models in the future. Finally, in the case of the comprehensive MI model, the remodeling processes that occur in the infarct scar region were altered only at 4 distinct points during the 4 weeks of growth. In future iterations, it may be advantageous to prescribe volume loss within the infarct scar, collagen deposition/increase in stiffness, and changes in EDP in a more continuous, gradual manner.

3.5 Conclusion

Our FE model can capture 8 weeks of growth following volume overload in the absence of MI after optimizing only two parameters within a previously developed growth law. These models are also the first to explore the effects that infarct scar size and stiffness and end-diastolic pressure have on growth following MI. We conclude that for infarction, as in a number of other cardiac pathologies, hemodynamics is the main driver of growth and must be accounted for in growth models. Furthermore, our MI growth model that accounts for the interplay between post-MI remodeling processes, in which the remaining infarct scar volume and stiffness along with EDP vary over time while the remote region remodels, is to our knowledge the most comprehensive model of post-MI ventricular remodeling to date. This model provides the framework to (1) capture the changes that occur in the ventricle following MI, and (2) simulate how potential therapies that alter the mechanics of the evolving scar will affect the growth and remodeling of both the infarct scar and remote myocardium regions.

Chapter 4

4 A Statistical Modeling Framework to Predict Ventricular Remodeling and Patient Outcome Following Cardiac Resynchronization Therapy

4.1 Introduction

In the previous chapters we built a biophysical mechanistic model of an infarcted left ventricle (LV) that predicted long-term growth and remodeling following myocardial infarction (MI). Such models may help prioritize potential treatments, such as polymer injection or local reinforcement with a patch, before the onset of heart failure (HF); however, once HF occurs, a different approach is needed to optimize current therapies aimed at reversing HF and to predict responses to such therapies.

4.1.1 Dyssynchronous Heart Failure

According to the American Heart Association, nearly six million Americans suffer from HF each year[7]. Many of these patients with HF (and/or MI) develop ventricular dyssynchrony[91]. The chambers of their hearts no longer contract synchronously, which prevents their hearts from efficiently pumping oxygen-rich blood to the rest of their bodies, worsens symptoms, and decreases survival. One of the most common types of dyssynchrony is left bundle branch block (LBBB)[92]. LBBB refers to the delay or blockage of electrical impulses to the left side of the heart and is often present in patients with HF and MI, as the non-conductive infarct scar slows or even blocks the electrical signal. This leads to both inter and intraventricular mechanical dyssynchrony in which the LV free/lateral wall experiences delayed contraction and increased stretching compared to the septal wall[93–98]. Consequently, LV pump function is impaired[92] while LV dilation and asymmetric wall thickening occur[98–100]. Ventricular dilation exacerbates mechanical dyssynchrony, which triggers a downward spiral of further pump impairment and LV dilation[81]. If left untreated, LBBB results in a 3-year mortality risk of up to 58%[92, 94].

4.1.2 Cardiac Resynchronization Therapy

Fortunately, a revolutionary procedure called cardiac resynchronization therapy (CRT) offers lifesaving benefits to patients by using pacemakers with electrical leads to alter the mechanics of the heart, resynchronize contraction, and reverse HF. CRT is offered to patients in sinus rhythm with moderate to severe heart failure (New York Heart Association [NYHA] Classification for Symptom Severity: Classes II-IV), an ejection fraction (EF) less than or equal to 35%, and a QRS duration greater than 150 milliseconds[101, 102]. A CRT pacing device is used to restore coordinated contraction of the heart by electrically stimulating multiple locations on the heart at appropriate times. Multiple clinical trials have shown that CRT can improve the health of patients by: reversing LV dilation (decreasing left ventricular end systolic volume [LVESV]), improving NYHA functional class, decreasing HF hospitalizations, improving LVEF, and improving overall survival[103–108]. Clinically, a CRT responder is defined as a patient who experiences a 15% or more reduction in LVESV measured at 6 months post-procedure. While approximately 50,000 patients undergo this procedure annually, an alarming 30-50% of patients selected to receive the procedure under current guidelines fail to respond to the treatment[101, 102, 109].

4.1.3 Important Factors of CRT Response

Anticipating the success of CRT is important for guiding treatment, yet difficult due to numerous procedural possibilities and complex interactions between patient variables/factors. Theoretically, CRT can account for patient-to-patient variability as clinicians can tailor the therapy with specific lead locations, timing, and/or pacing protocols. However, far too many strategies exist to test during the implantation procedure, and the acute changes in electrical activity measured during implantation do not always accurately predict patient response and long-term remodeling.

On the other hand, complex interactions between multiple clinical variables/factors of patients, including a patient's genetics, comorbid conditions, medications, blood testing results, hemodynamics, exercise capacity, cardiac electrical function, and cardiac mechanical function further complicate CRT response predictions. Previous work has shown that parameters such as a patient's CURE-SVD score (a measure of ventricular dyssynchrony), QLV (a measure of the time from QRS onset to the electrogram at the LV lead location), the presence of scar at the LV

lead location, and the mechanical stretch (delayed circumferential contraction) at the LV lead location are the four most important factors in accurately predicting binary response to CRT (responder versus non-responder)[16]. While these parameters are able to predict binary outcome to CRT, they do not successfully predict the degree of reverse remodeling (the reduction in LVESV). Additional factors not included in this study, such as exercise capacity and neurohormonal activity, may improve predictions of CRT outcome, ventricular remodeling, and long-term survival, and will be included in this chapter.

Cardiac strain curves may also provide helpful information in anticipating CRT success. Cardiac strain curves quantify the deformation of 18 spatial sectors within a short-axis slice of the LV throughout the cardiac cycle. These curves are derived from DENSE-MRI[110] and used to compute the CURE-SVD score, which is a single value between 0 and 1 that strongly predicts CRT response[16]. Reducing the dimensionality of the strain curves from 18 sectors $\times$ ~30 MR frames to one single value may result in the loss of information useful in predicting response. Therefore, consideration of entire strain curves may improve CRT prediction by capturing complete regional mechanics of the ventricle. Additionally, because previous mechanistic growth models have estimated cardiac growth using differences in strain between overloaded and homeostatic conditions[59], calculating changes in strain curves from pre-CRT to post-CRT may allow for the prediction of reverse growth following the therapy.

4.1.4 Previous Attempts at Predicting CRT Response

Previous work employed logistic regression to successfully predict binary response to CRT. Parameters such as the CURE-SVD score, QLV, the presence of scar at the LV lead location, and the mechanical stretch at the LV lead location accurately predicted CRT response with an area under the receiver operating characteristic curve (AUC) of 0.95[16]. This study also demonstrated that patients with CURE-SVD scores less than 0.70, no scar at the left-ventricular lead placement site, and delayed contraction at the lead location had a 100% response rate to CRT. Another study used a similar approach and demonstrated that the CURE-SVD score along with the Seattle Heart Failure Model (SHFM), one of the most widely used risk stratification models for overall survival in patients with HF and implantable cardioverter-defibrillators[111], informed survival after CRT[112]. In fact, patients with CURE-SVD less than 0.60 and SHFM score less than 0.70 had a greater 4-year survival compared to the other cohort of patients.

Other studies have used more complex machine learning models to stratify patients based on common clinical parameters, LV volumes, LV deformations, and QRS waveforms while predicting response and mortality. One study used baseline (pre-CRT) demographic and clinical information, electrocardiogram- and echo-derived parameters, laboratory values, medications, and longitudinal strain tracings of 1106 HF patients to identify the phenotypes of CRT responders[113]. Dimensionality reduction was applied to this matrix of parameters and k-means clustering was utilized to generate 4 distinct phenotypes of CRT responders. This study showed that some of the best responders to CRT included patients who were female, had LBBB, and non-ischemic cardiomyopathy (ICM) while some of the worst included ICM patients without LBBB. Another study performed principal component analysis (PCA) on the baseline 12-lead QRS waveforms to identify two groups of CRT patients with different outcomes[114].

Although these approaches are promising, no study has integrated all previously mentioned variables into one comprehensive data set and developed a framework to predict CRT outcomes, ventricular remodeling, and long-term survival. Furthermore, few studies include parameters gathered several months after implantation. Statistical models are capable of uncovering patterns in such complicated and comprehensive data. Successful implementation of these models can improve CRT delivery and identify viable CRT candidates. Accurate models can also help clinicians use pre-CRT parameters and post-CRT response measures to identify patients with the most unfavorable expected outcomes, which will allow the clinicians to refer these patients to more advanced HF therapies such as mechanical circulatory support or heart transplantation. Therefore, in this chapter we combine clinical data into a single, statistical analysis to (1) identify the pre-CRT information most capable of predicting post-CRT response measures and (2) utilize the pre- and post-CRT parameters to predict long-term survival.

Furthermore, this statistical analysis is useful in testing current, physics-based theories of CRT response. Because the application of CRT alters the regional mechanics of the ventricle and it is hypothesized that changes in regional mechanics drive cardiac growth and remodeling, changes in mechanics from pre- to post-CRT may be helpful in predicting CRT response. Rather than constructing a computationally expensive biophysics-based mechanistic model that accounts for a patient's ventricular geometry, regional deformation, and electrical conduction pathways to test this hypothesis, we will instead use a statistical modeling framework. This

approach will allow us to correlate the components of changes in regional ventricular strain derived from DENSE-MRI with ventricular remodeling.

4.2 Methods

4.2.1 Gathering a Clinically Relevant Data Set

Before receiving CRT at the University of Virginia Health System, 198 patients completed intake forms which described their demographics along with comorbid conditions and medications, underwent laboratory studies and vital sign measurements along with exercise testing, and received contrast-enhanced CMR imaging, echocardiography, and electrocardiograms (ECG). At 6 months post-CRT, they received echocardiography or CMR imaging along with laboratory studies and exercise testing to quantify three response measures: fractional change in the left ventricular end-systolic volume index (Δ LVESVI), serum BNP levels, and change in peak VO_2 (Δ peak VO_2). The patients were then followed for survival with routine interrogations up to five years post-procedure. All patients were NYHA functional class II to IV and met the established guidelines for CRT. All patients provided informed consent for this study, which was approved by the Institutional Review Board for Human Subjects Research at the University of Virginia.

1. **Patient Characteristics**: Demographic characteristics (age, sex, and race), comorbid conditions in addition to HF (ischemic cardiomyopathy, hypertension, atrial fibrillation, chronic kidney disease, diabetes mellitus, and prior coronary artery bypass graft), and medications (beta-blocker, ace inhibitor/angiotensin receptor blocker, loop diuretic dosage, digoxin, and statin) at the time of CRT were documented from intake data during enrollment in the study and information accessible medical records. The SHFM score, which is calculated based on multiple patient covariates and characteristics, was recorded for each patient.

2. **Laboratory Studies, Vital Sign Measurements & Exercise Testing**: Patients underwent laboratory studies, vital sign measurements, and exercise testing before the CRT procedure. The laboratory studies included blood tests for serum sodium, creatinine, hemoglobin, and B-type natriuretic peptide (BNP). Glomerular filtration rate (GFR) was estimated from the results of the laboratory studies. Vital sign measurements included

systolic blood pressure readings, and peak oxygen output was assessed through exercise testing.

3. **CMR Imaging Protocol & Echocardiography**: Prior to the CRT procedure, complete CMR examinations were performed for all patients. The CMR protocol included cine imaging and cine DENSE for all patients, and those with prior infarcts also received late gadolinium enhancement (LGE). Circumferential strain from a mid-ventricular 2-dimensional cine DENSE short-axis slice was calculated semiautomatically to determine the CURE-SVD score (with a value between 0 and 1 where 0 represents full dyssynchrony and 1 represents full synchrony). Standard 2D echocardiographic images with Doppler were obtained for all patients at baseline and 6 months after CRT. Where appropriate, images from either CMR or echocardiography were used to determine ventricular volumetric measurements such as the left and right ventricular ejection fractions (LVEF & RVEF), left and right ventricular end-diastolic volumes indexed for body surface area (LVEDVI & RVEDVI), and left and right ventricular end-systolic volume index (LVESVI & RVESVI).

4. **ECG Analysis**: All patients underwent 12 lead ECG procedures to obtain electrical conduction parameters such as QRS duration and the QRS to left ventricular intrinsic activation interval (QLV). Conduction delays such as LBBB or RBBB were also recorded along with whether a paced rhythm was present. Further, patients who received a new device (De Novo) as well as those who received an upgraded device (Upgrade) from previous implantable cardioverter-defibrillators (ICDs) at the time of CRT were noted.

5. **Post-CRT Response Measures**: At 6 months post-CRT, LVESVI was calculated for all patients with either CMR or echocardiographic images, and the fractional/percent change in LVESVI (Δ LVESVI) was calculated with **Equation 1**. The change in peak oxygen output (Δ peak VO_2) was computed 6 months after CRT by subtracting the exercise testing results obtained pre-CRT from those obtained post-CRT. Serum levels of BNP were also quantified with blood tests 6 months post-CRT (BNPP). Favorable CRT response measures include: (1) a 15% or more reduction in LVESVI (Δ LVESVI $\leq$ -0.15), (2) an increase in peak oxygen output, and (3) low levels of BNP. Finally, determination of

death at 4-years post-CRT was based on clinical follow-up, reports of death from families, and a regional death index.

$$\Delta\text{LVESVI} = \frac{\text{LVESVI}_{\text{Post-CRT}} - \text{LVESVI}_{\text{Pre-CRT}}}{\text{LVESVI}_{\text{Pre-CRT}}} \qquad \textbf{Equation 1}$$

6. **Missing Data**: With respect to the parameters gathered before the CRT procedure, missing data for QLV, CURESVD, SHFM, LVEDVI, LVESVI, RVEDVI, RVESVI, LVEF, RVEFB, peak VO_2, and BNP ranged from 1 to 11% and were imputed with each respective median value. Concerning the parameters gathered 6-months after CRT, missing data for Δ LVESVI and BNP ranged from 2.5 to 10% and were also imputed with each respective median value. Δ peak VO_2 exhibited the largest percentage of missing data (20%) often due to the inability of the patients to exercise. We imputed the post-CRT VO_2 values as those at baseline, under the assumption there was no improvement in exercise capacity and calculated Δ peak VO_2 accordingly.

4.2.2 Assessing Baseline Characteristics & Identifying Pre-CRT Parameters that Strongly Associate with Post-CRT Response Measures

39 baseline variables were identified and used as input for the analysis. These variables included both categorical and continuous data, and, to limit redundancy in our linear models, we constructed a correlation matrix with the continuous variables to identify collinearity and eliminate unnecessary variables. Stepwise linear regression models were implemented for each of the three post-CRT response parameters (Δ LVESVI, BNPP, and Δ peak VO_2) to identify the pre-CRT clinical parameters that are strongly associated with the response measures. The stepwise linear regressions determined the necessary parameters to remain in each of the three models based on the Akaike information criterion (AIC) while also identifying parameters strongly associated with each response measure. The parameters associated with at least one of the three response measures were then included in a multivariate multiple regression (MANOVA) in which the dependent variable was the linear combination of the three response parameters. Pillai trace values and F-statistics were calculated for each of the inputs.

4.2.3 Predicting Long-Term Survival of Patients with Gaussian Mixture Modeling and Logistic Regression

A Gaussian mixture model (GMM) was optimized to cluster patients using the three post-CRT response parameters as inputs. A GMM is a probabilistic model that assumes all data points are generated from a mixture of a finite number of Gaussian distributions. This model assigns data points to a specific Gaussian-shaped cluster described by a mean and variance/covariance. More specifically, a Gaussian mixture model is parameterized by two types of values: (1) the mixture component/cluster weights and (2) the component means and variances/covariances. For a Gaussian mixture model with *K* components, the k^{th} component has a mean of $\vec{\mu}_k$ and covariance matrix of $\sum_k$ for the multivariate case. The mixture component weights are defined as $\emptyset_k$ for component C_k, with the constraint that $\sum_{i=1}^{K} \emptyset_i = 1$ so the total probability distribution normalizes to 1.

Expectation maximization (EM) is the technique most commonly used to estimate the parameters of the GMM and consists of two steps. The first step is the expectation (E) step and involves calculating the expectation component assignment C_k for each data point with given the model parameters $\emptyset_k$, $\vec{\mu}_k$, and $\sum_k$; in other words, for each data point, the probability of it belonging to each component (cluster) is computed. The second step is the maximization (M) step in which the expectations in the previous step are maximized by updating $\emptyset_k$, $\vec{\mu}_k$, and $\sum_k$ and weighted using the probabilities. This is an iterative process that repeats until the algorithm converges and gives a maximum likelihood estimate for the parameters of each distribution. A more detailed explanation is as follows:

1. Initialization Step: Assign initial values for $\emptyset_k$, $\vec{\mu}_k$, and $\sum_k$.

    a. Randomly assign samples without replacement from the given dataset $X = \{\vec{x}_1, \dots, \vec{x}_N\}$ (where $\vec{x}$ is a length *d* row vector) to the component mean estimates $\vec{\mu}_1, \dots \vec{\mu}_K$. For example, for 3 components (clusters) and 200 data points/observations (*K* = 3 and *N* = 200), set $\vec{\mu}_1 = \vec{x}_{45}$, $\vec{\mu}_2 = \vec{x}_{32}$, and $\vec{\mu}_3 = \vec{x}_{10}$.

b. Set all component covariance estimates equal to the sample variance $\sum_1, \ldots \sum_K = \frac{1}{N}\sum_{i=1}^{N}(\vec{x}_i - \vec{x})^T(\vec{x}_i - \vec{x})$, where $\vec{x}$ is the mean of X.

c. Set all component distribution prior estimates to the uniform distribution $\widehat{\emptyset}_1, \ldots \widehat{\emptyset}_K = {}^1/_K$.

2. Expectation (E) Step: For each data point, calculate the probability that it is generated by each component C_k.

a. $\hat{\gamma}_{iK} = \frac{\widehat{\emptyset}_K \cdot \mathcal{N}(\vec{x}_i|\vec{\mu}_K, \sum_K)}{\sum_{j=1}^{K} \widehat{\emptyset}_j \cdot \mathcal{N}(\vec{x}_i|\vec{\mu}_j, \sum_j)}$ and thus $\hat{\gamma}_{iK} = p\left(C_k|\vec{x}_i, \widehat{\emptyset}, \vec{\mu}, \sum\right)$

where $\mathcal{N}(\vec{x}|\vec{\mu}_i, \sum_i) = \frac{1}{\sqrt{(2\pi)^d \det(\sum_i)}} \exp\left(-\frac{1}{2}(\vec{x} - \vec{\mu}_i)^T(\sum_i)^{-1}(\vec{x} - \vec{\mu}_i)\right)$ is the probability density function of a multivariate Gaussian distribution.

3. Maximization (M) Step: Using the previously calculated $\hat{\gamma}_{ik}$, update $\widehat{\emptyset}_K$, $\vec{\mu}_K$ and $\sum_K$.

a. $\widehat{\emptyset}_K = \sum_{i=1}^{N} \frac{\hat{\gamma}_{iK}}{N}$

b. $\vec{\mu}_K = \frac{\sum_{i=1}^{N} \widehat{\gamma_{ik}} \vec{x}_i}{\sum_{i=1}^{N} \hat{\gamma}_{iK}}$

c. $\sum_K = \frac{\sum_{i=1}^{N} \hat{\gamma}_{iK}(\vec{x}_i - \vec{\mu}_K) \cdot (\vec{x}_i - \vec{\mu}_K)^T}{\sum_{i=1}^{N} \hat{\gamma}_{iK}}$

4. This process is repeated until the log likelihood of the data under the current model's parameters does not improve by a user-specified tolerance.

Within these models the structure of the covariance matrix is unknown and can be specified as spherical, diagonal, and full. A spherical structure designates that the covariance matrix is diagonal with *equal* elements along the diagonal whereas a diagonal structure is one in which the covariance matrix is diagonal with *different* elements along the diagonal. A full covariance matrix allows for correlation between random variables (i.e., non-zero off diagonal values). In addition to not knowing the structure of the covariance matrices, the optimal number of clusters (components) is unknown. Therefore, we ran multiple GMMs while varying the covariance structure (spherical, tied, diagonal, and full) and number of clusters (1-6). The covariance structure and number of clusters that minimized the Bayesian information criterion (BIC) were implemented in the final GMM. Once the data points were assigned to the appropriate clusters, chi-square tests were used to compare categorical variables between groups while an ANOVA was used to compare continuous variables between groups. Then, a Kaplan-Meier analysis was performed to construct the survival curve for each of the clusters to examine the model's ability to predict long-term survival. Log-rank tests were used to measure significance between survival curves.

In a 5-fold cross-validation framework, multivariable logistic regression models were utilized to predict survival at four years post-CRT. In the first model, the input data consisted of three pre-CRT parameters (CURE-SVD, peak VO_2, and BNP levels) which were determined to be the best predictors of 4-year death through a separate regression model. In the second model, the input data consisted of the aforementioned pre-CRT parameters plus the three response variables (ΔLVESVI, BNPP, and Δ peak VO_2). ROC curves for each fold within the cross-validation were generated, and areas under the ROC curves were calculated to compare model performances.

4.2.4 Testing if the Change in Mechanics from Pre- to Post-CRT Can Predict Remodeling

We gathered pre- and post-CRT cardiac strain curves from a subgroup of 25 patients within the existing cohort. We derived different metrics from the strain data to determine if any were predictive of long-term remodeling. Because previous mechanistic growth models have defined the stimulus for growth as a difference in the maximum fiber strain in the overloaded case and the fiber strain under homeostatic conditions[59], we calculated the difference (delta) in

circumferential strain (E_{cc}) from pre-CRT to post-CRT. The strain data was extracted from the mid-wall of short axis MRI slices, so the circumferential direction (E_{cc}) is the fiber direction and thus agrees with the previous mechanistic models. Delta strain curves existed for each of the 18 spatial sectors. We calculated the peak, minimum, and average of each of these curves to help generalize the change in mechanics due to CRT. We then fit a linear regression model to each metric with the percent change in LVESV as the independent variable and examined the R^2 values for each to elucidate the predictive power of the strain-based metrics.

4.3 Results

4.3.1 Baseline Characteristics

Demographic characteristics, comorbid conditions, medications, laboratory findings, vital signs, exercise testing results, and imaging findings for the 198 patients (age 67.4 ± 11.3 years; 27.3% female; 13.6% African American) are shown in **Table 1**. The median Δ LVESVI was -18% (interquartile range -33% to 1%). A total of 58% met echocardiographic criteria for favorable CRT response based on at least a 15% decrease in the LVESVI 6 months after the procedure. The median Δ peak VO_2 was 0 mL/kg/min (interquartile range -1.4 to 1.3 mL/kg/min), and the median BNPP level was 195.0 pg/mL (interquartile range 77.3 to 599.0 pg/mL). At 4 years post-CRT, 25.3% of the total cohort had died.

The correlation matrix between all continuous variables is shown in **Figure 4.1** in which red represents a positive Pearson standard correlation coefficient and blue represents a negative Pearson standard correlation coefficient. Input variables with coefficients greater than or equal to 0.8 included (1) weight and BMI, (2) LVEDVI and LVESVI, and (3) RVEDVI and RVESVI. To avoid collinearity and redundancy within the linear regression models, we removed BMI, LVESVI, and RVESVI from the analysis. Creatinine and GFR had a correlation coefficient of -0.77 and were subsequently both included in the analysis.

Figure 4.1 Correlation Matrix for Continuous Pre-CRT Variables

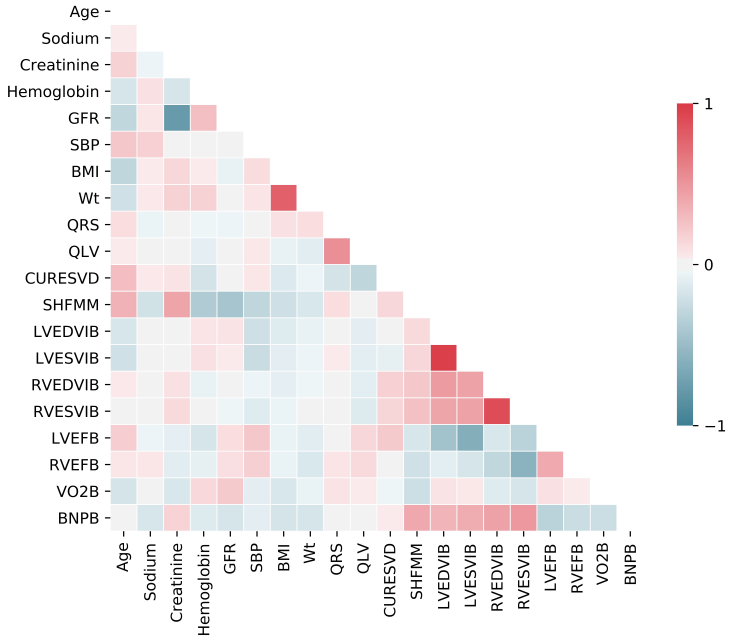

Weight and BMI, LVEDVI and LVESVI, and RVEDVI and RVESVI exhibited Pearson standard correlation coefficients greater than 0.8, thus BMI, LVESVI, and RVESVI were removed from the analysis.

Table 1	Patient Characteristics				
	Cohort (N = 198)	Group 1 (N = 113)	Group 2 (N = 51)	Group 3 (N = 34)	p Value
Demographics					
Age, years	67.4 (58.0-73.6)	66.6 (57.0-72.7)	68.1 (61.3-74.6)	68.5 (60.9-74.8)	0.68
BMI	28.7 (25.4-33.7)	30.3 (26.5-34.5)	28.3 (24.8-32.3)	26.1 (22.6-30.2)	0.007
Wt (kg)	89.2 (74.8-102.9)				
Female	54 (27.3)	36 (32.9)	12 (23.5)	6 (17.6)	0.21
NYHA Heart Failure Class					
II	72 (36.4)	48 (42.5)	20 (39.2)	4 (11.8)	
III	125 (63.1)	65 (57.5)	31 (60.8)	29 (85.3)	
IV	1 (0.50)	0 (0)	0 ()	1 (2.9)	
SHFM Score	0.36 (-0.025-0.84)	0.2 (-0.12-0.6)	0.50 (-0.01-0.98)	0.90 (0.56-1.20)	<0.0001
Race					0.12
African American	27 (13.6)	15 (13.3)	9 (17.6)	8 (23.5)	
White/Other	171 (86.4)	98 (86.7)	42 (82.4)	26 (76.5)	
Comorbid Conditions					
Ischemic Cardiomyopathy	87 (43.9)	41 (36.3)	32 (62.7)	14 (41.2)	0.006
Hypertension	113 (57.1)	75 (66.4)	21 (41.2)	17 (50.0)	0.007
Atrial Fibrillation	51 (25.8)	32 (28.3)	9 (17.6)	10 (29.4)	0.60
Chronic Kidney Disease	62 (31.3)	32 (28.3)	14 (27.5)	16 (47.1)	0.09
Diabetes Mellitus	70 (35.4)	36 (31.9)	19 (37.3)	15 (44.1)	0.40
Prior CABG	33 (16.7)	16 (14.2)	13 (25.5)	4 (11.8)	0.14
Medications					
Beta-Blocker	190 (96.0)	108 (95.6)	49 (96.1)	33 (97.1)	0.93
ACE Inhibitor or ARB	173 (87.4)	102 (90.3)	45 (88.2)	26 (76.5)	0.10
Loop Diuretic Dose, mg					
0	58 (29.3)	35 (31.0)	16 (31.4)	7 (20.6)	
20-40	87 (43.9)	54 (47.8)	21 (41.2)	12 (35.3)	
60-80	35 (17.7)	16 (14.2)	8 (15.7)	11 (32.4)	
> 100	18 (9.1)	8 (7.1)	6 (11.8)	4 (11.8)	
Digoxin	17 (8.6)	7 (6.2)	5 (9.8)	5 (14.7)	0.28
Statin	120 (60.6)	69 (61.0)	31 (60.8)	20 (58.8)	0.97
Laboratory Studies, Vital Signs & Exercise Testing					
Systolic BP, mm Hg	118.5 (104.0-130.0)	118.0 (102.0-128.0)	124.0 (109.5-135.0)	111.0 (104.0-129.3)	0.31
Sodium, mEq/L	138.0 (137.0-140.0)	139.0 (137.0-140.0)	139.0 (137.0-141.0)	137.5 (136.0-139.8)	0.18
Creatinine, mg/dL	1.1 (0.9-1.3)	1.0 (0.9-1.2)	1.1 (1.0-1.40)	1.3 (1.1-1.5)	0.0002
Hemoglobin, g/dL	13.25 (12.3-14.7)	13.7 (12.5-14.8)	13.5 (12.3-15.0)	12.9 (12.1-14.0)	0.24
GFR, mL/min/1.72m^2	66.8 (54.0-84.1)	74.0 (59.4-88.2)	64.0 (51.1-72.3)	59.2 (46.5-72.6)	0.0003
BNP, pg/mL	272.0 (135.3-637.0)	167 (88-275)	333 (247-592)	1148 (778-2533)	<0.0001
Peak VO_2, mL/kg/min	14.4 (12.5-15.7)	14.4 (13.0-16.5)	13.8 (10.7-15.5)	14.2 (12.6-14.4)	0.013
CMR & Echocardiography Assessment Parameters					
LVEF, %	24.4 (17.7-30.4)	25.6 (18.9-31.0)	24.0 (18.0-29.6)	20.4 (14.6-27.1)	0.049
LVEDVI, mL/m^2	125.8 (102.8-152.7)	117.5 (98.6-137.0)	131.9 (109.5-151.5)	163.5 (121.9-192.0)	<0.0001
LVESVI, mL/m^2	93.6 (73.9-123.0)	89.1 (68.6-112.0)	96.9 (81.3-119.4)	128.0 (90.7-161.5)	<0.0001
RVEF, %	37.9 (25.3-45.6)	38.7 (32.0-49.0)	35.6 (21.2-43.8)	27.3 (18.2-38.6)	0.003
RVEDVI, mL/m^2	65.4 (52.8-82.7)	57.0 (48.1-74.2)	68.2 (58.4-81.6)	97.6 (76.0-120.6)	<0.0001
RVESVI, mL/m^2	38.6 (29.7-55.1)	35.7 (25.1-45.7)	40.9 (33.7-56.3)	62.9 (47.2-90.2)	<0.0001
LGE Presence	95 (48.0)	48 (42.5)	28 (54.9)	19 (55.9)	0.20
CURE-SVD	0.59 (0.45-0.76)	0.54 (0.40-0.69)	0.65 (0.47-0.80)	0.735 (0.57-0.84)	<0.0001
ECG Parameters					
QRS, ms	157.5 (141.3-175.0)	160.0 (147.0-178.0)	152.0 (134.5-160.0)	158.0 (137.0-180.0)	0.088
QLV, ms	119.0 (85.5-148.0)	130.0 (98.0-150.0)	100.0 (77.5-125.0)	102.5 (72.5-150.0)	0.006
LBBB	149 (75.3)	86 (76.1)	41 (80.4)	22 (64.7)	0.25
RBBB	22 (11.1)	9 (8.0)	5 (9.8)	8 (23.5)	0.038
Paced Rhythm	29 (14.6)	19 (16.8)	4 (7.8)	6 (17.6)	0.28
Upgrade or New Device					0.17
De Novo Device	150 (75.8)	80 (70.8)	43 (84.3)	27 (79.4)	
Upgrade Device	48 (24.2)	33 (29.2)	8 (15.7)	7 (20.6)	
Response Measures at 6-Months Post-CRT					
Fractional Change in LVESVI	-0.18 (-0.33-0.01)	-0.24 (-0.43 - -0.14)	-0.09 (-0.19-0.07)	0.005 (-0.18-0.10)	<0.0001
Change in Peak VO_2, mL/kg/min	0.0 (-1.4-1.3)	0.0 (-0.8-1.9)	0.0 (-1.63-1.1)	-0.35 (-2.5-0)	0.098
BNP, pg/mL	195.0 (77.3-599.0)	95.3 (43.0-164.0)	456 (333-700)	2030 (1445-2740)	<0.0001
Survival Status at 4 Years					<0.0001
Alive	148 (74.4)	102 (90.3)	33 (64.7)	13 (38.2)	
Dead	50 (25.3)	11 (9.7)	18 (35.3)	21 (61.8)	

Values are median (interquartile range) or n (%).
ACE = angiotensin-converting enzyme; ARB = angiotensin receptor blocker; BMI = body mass index; BNP = B-type natriuretic peptide; BP = blood pressure; CABG = coronary artery bypass graft; CURE-SVD = circumferential uniformity ratio estimate with singular value decomposition; GFR = glomerular filtration rate; LBBB = left bundle branch block; LGE = late gadolinium enhancement; LVEDVI = left ventricular end-diastolic volume index; LVEF = left ventricular ejection fraction; LVESVI = left ventricular end-systolic volume index; MLHFQ = *Minnesota Living with Heart Failure* Questionnaire; NYHA = New York Heart Association; QLV = QRS-LV electrogram time; RBBB = right bundle branch block; RVEDVI = right ventricular end-diastolic volume index; RVEF = right ventricular ejection fraction; RVESVI = right ventricular end-systolic volume index; SHFM = Seattle Heart Failure Model, Wt =weight.

4.3.2 Stepwise Linear Regression to Identify Key Pre-CRT Parameters

The stepwise linear regression analyses showed that different pre-CRT parameters were associated with each of the three response variables of interest, which describe cardiac function (Δ LVESVI), neurohormonal activity (BNPP), and oxygen output (Δ peak VO2) following CRT. The pre-CRT parameters most associated with each response variable are shown in **Table 2**.

Based on the p-values from stepwise linear regression, the pre-CRT parameters most significantly associated with Δ LVESVI are shown in **Table 2A** and include CURE-SVD, RVRF at baseline, QLV, age, and ischemic cardiomyopathy. The coefficient value for CURE-SVD was positive; therefore, larger CURE-SVD values result in a more positive fractional change in LVESVI which is unfavorable. This agrees with previously published work which demonstrated that patients with lower CURE-SVD scores (more dyssynchronous ventricular contractions) respond better to CRT as they achieve a more negative fractional change in LVESVI[16].

The pre-CRT parameters most associated with BNPP levels are shown in **Table 2B** and include BNP levels at baseline, CURE-SVD, ischemic cardiomyopathy, RVEDVI at baseline, the presence of LGE, age, loop diuretic dosages greater than 100 mg, and the SHFM score. The coefficient value for the BNP level at baseline was positive. Because the favorable response in this case is low levels of BNP, lower levels of BNP before CRT indicate better response.

Table 2C shows the pre-CRT parameters that are strongly associated with Δ peak VO_2, and they include the peak VO_2 at baseline, systolic BP, the presence of LGE, NYHA Class III, QRS duration, the presence of an upgraded device, and hemoglobin. The coefficient for having an NYHA classification of III was negative; therefore, the presence of NYHA Class III results in less change in peak VO_2 following CRT, which is unfavorable. NYHA classes are based on the severity of heart failure symptoms, such as a patient's ability to climb stairs without getting out of breath. Patients with Class III HF struggle with such activities and may have symptoms too severe to experience improvement from CRT as compared to those belonging to Class II.

With respect to both Δ LVESVI and BNP response measures, the presence of ischemic cardiomyopathy was significant. This parameter was associated with less favorable LVESVI response as a '1' for this variable drove the predicted value of the LVESVI change to be more

positive (due to the positive coefficient estimate). On the other hand, the presence of ischemic cardiomyopathy was associated with a more favorable BNP response due to the negative coefficient estimate that results in lower post-CRT BNP levels.

Table 2A	**Multivariable Linear Regression Model for Δ LVESVI**		
Model Variable	**Model Coefficient**	**Standard Error**	**p Value**
CURE-SVD	0.43	0.15	<0.0001
RVEF at Baseline	-0.0032	0.002	0.002
QLV	-0.0013	0.0008	0.005
Age	-0.0033	0.003	0.02
Ischemic Cardiomyopathy	0.067	0.063	0.04
Table 2B	**Multivariable Linear Regression Model for BNPP**		
Model Variable	**Model Coefficient**	**Standard Error**	**p Value**
BNP at Baseline	0.62	0.11	<0.0001
CURE-SVD	850	388	<0.0001
Ischemic Cardiomyopathy	-269	188	0.005
RVEDVI at Baseline	4.3	3.2	0.008
LGE	253	192	0.01
Age	-10.6	8.0	0.01
Loop Diuretic Dose > 100	-341	303	0.03
SHFMM	186	174	0.04
Table 2C	**Multivariable Linear Regression Model for Δ Peak VO_2**		
Model Variable	**Model Coefficient**	**Standard Error**	**p Value**
Peak VO_2 at Baseline	-0.42	0.11	<0.0001
Systolic BP	-0.028	0.023	0.02
LGE	-1.2	1.06	0.03
NYHA Class III	-0.94	0.91	0.04
QRS	0.02	0.019	0.04
Upgraded Device	-1.06	1.04	0.05
Hemoglobin	0.27	0.27	0.05

Additionally, the Pillai trace values obtained from the multivariate multiple linear regression are shown in **Table 3** and indicate that the five variables most associated with all the post-CRT response measures were the BNP pre-CRT, pre-CRT peak VO_2, CURE-SVD score, the presence of ischemic cardiomyopathy, NYHA Class, the presence of LGE, age, and RVEF and RVEDVI at baseline.

Table 3	**Multivariate Multiple Linear Regression for All Response Parameters**		
Model Variable	**Pillai Trace Value**	**F Statistic**	**p Value**
BNP at Baseline	0.41	37.7	<0.0001
VO_2 at Baseline	0.24	16.7	<0.0001
CURE-SVD	0.14	8.73	<0.0001
Ischemic Cardiomyopathy	0.10	5.60	0.001
NYHA	0.09	2.57	0.02
LGE	0.06	3.44	0.02
Age	0.05	2.86	0.04
RVEF at Baseline	0.05	2.78	0.04
RVEDVI at Baseline	0.05	2.71	0.05

4.3.3 Gaussian Mixture Model Clustering & Survival Analysis

Using the three response measures as input, the GMM that resulted in the lowest BIC included 3 clusters with a diagonal covariance structure as demonstrated in **Figure 4.2A**. The three clusters/groups of patients are displayed in **Figure 4.2B**. The summary of the 6-month post-CRT response measures, along with the baseline characteristics for each cluster of patients, is shown in **Table 1**.

Figure 4.2 Gaussian Mixture Model

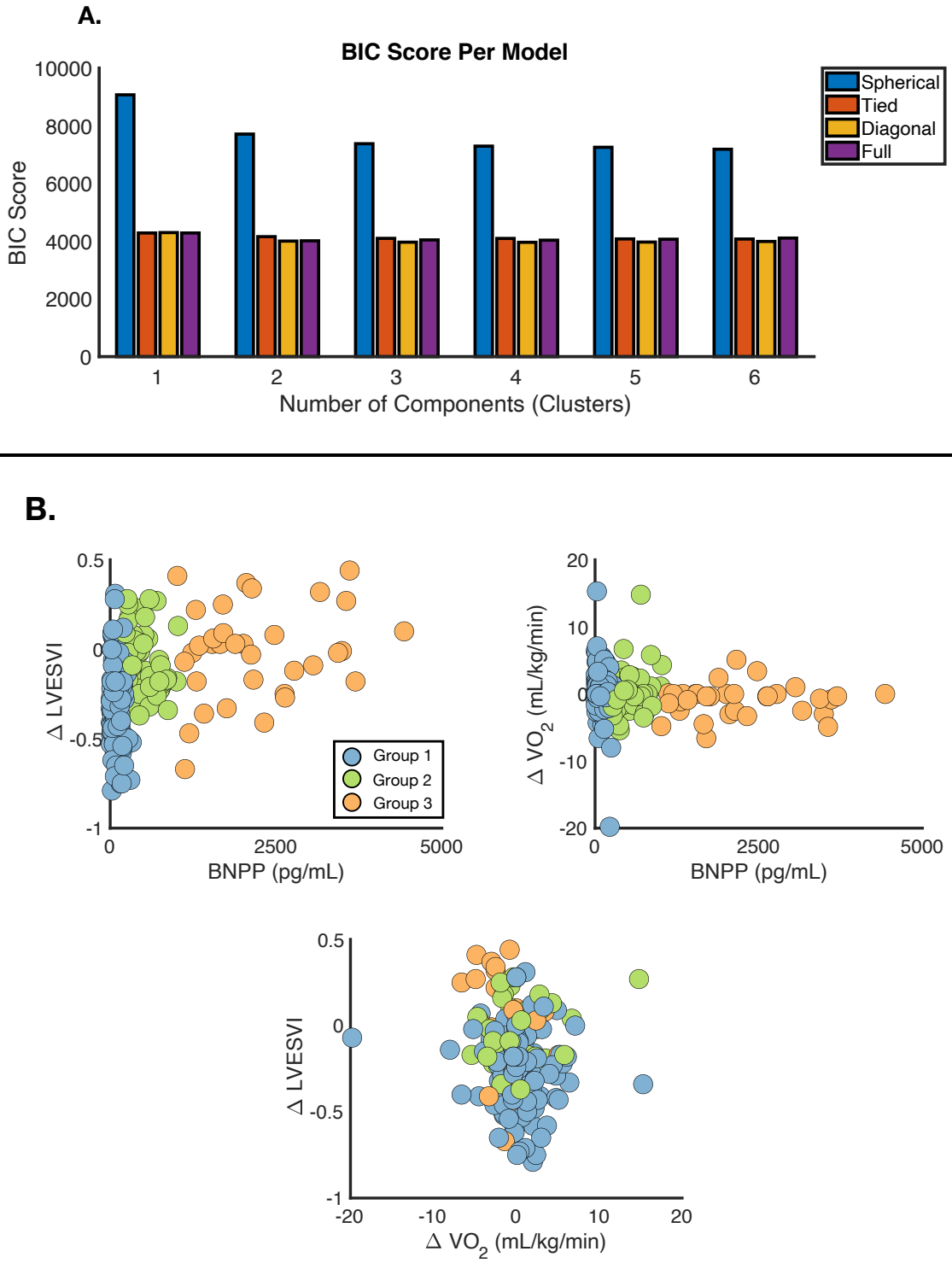

(A) The BIC scores for each of the GMMs tested are shown. Except for those with the spherical covariance matrix, all models exhibited similar BIC scores. The minimum score occurred in the GMM with 3 clusters with a diagonal covariant structure. (B) The optimal GMM stratified the patients within our cohort into 3 distinct groups.

The model clustered 113 patients into Group 1, and this group exhibited a median change in the LVESVI 6 months after CRT of -24% (interquartile range -43% to -14%). A total of 72.6% of patients within this group met echocardiographic criteria for favorable CRT response. The median change in peak VO_2 was 0 mL/kg/min (-0.8 to 1.9 mL/kg/min), and the median BNP level was 95 pg/mL (43 to 64 pg/mL) in this group.

The model assigned 51 patients into Group 2, which exhibited a median change in the LVESVI 6 months after CRT of -9% (-19% – 7.0%). 45.1% of patients within this group met echocardiographic criteria for favorable CRT response. The median change in peak VO_2 was 0 mL/kg/min (-1.63 – 1.1 mL/kg/min), and the median BNP level was 456 pg/mL (333 – 700 pg/mL) in this group.

The model placed 34 patients into Group 3, and this group exhibited a median change in the LVESVI 6 months after CRT of 0.5% (-18% – 10%). Only 29.4% of patients within this group met echocardiographic criteria for favorable CRT response. The median change in peak VO_2 was -0.35 mL/kg/min (-2.5 – 0 mL/kg/min), and the median BNP level was 2030 pg/mL (1445 – 2740 pg/mL) in this group.

While the baseline characteristics of the cohort were not used in the cluster analysis, several of these variables were significantly different among the groups following stratification (with p-values < 0.01). These variables include BMI, SHFM score, ischemic cardiomyopathy, hypertension, creatinine, GFR, BNP at baseline, LVEF, LVEDVI, LVESVI, RVEF, RVEDVI, RVESVI, CURE-SVD, QLV, and RBBB.

The Kaplan-Meier survival analysis is displayed in **Figure 4.3A** and demonstrated that patients in Group 1 had the best survival, patients in Group 2 had intermediate survival, and patients in Group 3 had the worst survival. Using the log-rank test, p-values for the differences in survival among the clusters were significant.

Patients in Group 1 demonstrated the largest decrease in LVESVI with the smallest BNP values, which aids in explaining this cluster's highest probability of survival. Group 3 showed a slightly positive change in LVESV and the highest BNP levels, and a decrease in peak VO_2; these outcomes are unfavorable and explain this cluster's poorest survival. Patients in Group 2

experienced a slight decrease in LVESVI with modest BNP levels, which illustrates this cluster's intermediate survival.

Additionally, because it may be critical to predict the group of patients at highest risk with the greatest mortality after CRT, patients in Group 1 and 2 were condensed into a single group while Group 3 patients remained the same. The Kaplan-Meier survival analysis was re-performed, is displayed in **Figure 3B**, and demonstrated significant separation between the survival curves.

Figure 4.3 Kaplan-Meier Survival Curves

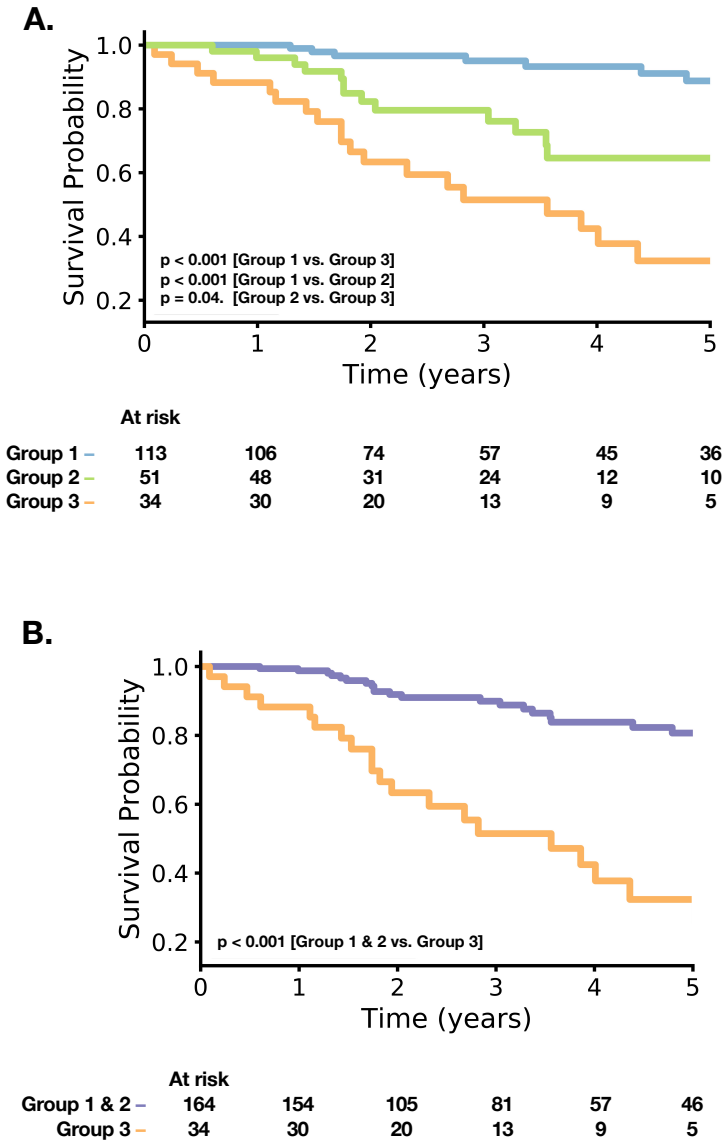

(A) Kaplan-Meier curves demonstrating the probability of survival at 5 years are presented for each of the three cluster groups. Patients in group 1 had a greater survival probability than patients in group 2 ($p < 0.001$) and in group 3 ($p < 0.001$). Patients in group 2 had a greater survival probability than patients in group 3 ($p = 0.04$). (B) Kaplan-Meier curves demonstrating the probability of survival at 5 years are presented for the condensed group (consisting of patients in cluster groups 1 and 2) and cluster group 3. Patients in the condensed group had a greater survival probability than patients in group 3 ($p < 0.001$)

4.3.4 Predictive Models of Survival

The ROC curves of the logistic regression model with the CURESVD score, pre-CRT BNP levels, and pre-CRT peak VO_2 levels as inputs are shown in **Figure 4.4A**. The area under the ROC curve for each fold within the cross-validation is displayed along with the area under the average ROC curve (0.78 ± 0.03). The results of the logistic regression model that incorporated the aforementioned variables plus the three response measures are displayed in **Figure 4.4B**. For each fold within the cross-validation, the area under the ROC curve was slightly higher in this model compared to the previous model. The area under the average ROC curve for this model (0.84 ± 0.03) is larger than that of the previous model, thus demonstrating that the CRT response measures add valuable information when predicting death at 4 years post-procedure.

Figure 4.4 Receiver-Operating Characteristic Curves for 4-Year Survival Prediction

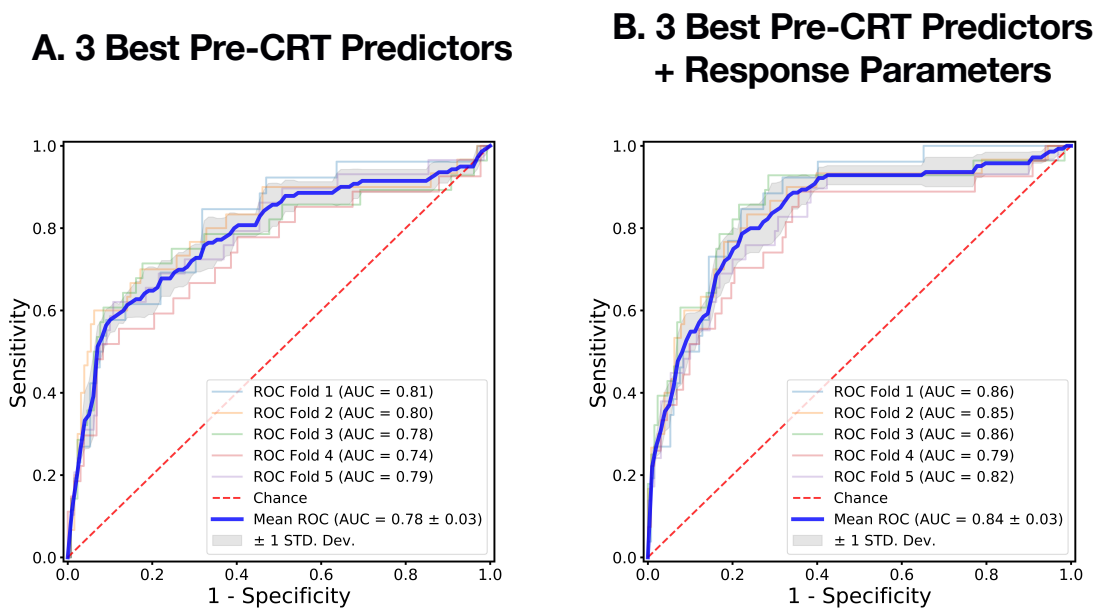

Receiver-operating characteric curves from logistic regression are shown for 2 models: one that takes into account the three best pre-CRT predictors (CURE-SVD, pre-CRT BNP levels, pre-CRT peak VO_2 levels) and one that takes into account those same three pre-CRT parameters plus the three response measures gathered 6 months post-CRT (fractional change in LVESVI, change in peak VO_2, and post-CRT BNP levels). The model incorporating both post-CRT and pre-CRT information displays an average area under the ROC curve (AUC) of 0.84 and slightly outperforms the model that includes only pre-CRT information with an AUC of 0.78.

4.3.5 Testing if the Change in Mechanics from Pre- to Post-CRT Can Predict Long-Term Remodeling

We obtained pre- and post-CRT strain data from 25 patients. 16 of these patients responded to CRT and demonstrated a reduction in LVESVI of 15%. **Figure 4.5A** illustrates a short-axis slice of the LV while labeling the 18 sectors. The strain data of a healthy patient (**Figure 4.5B**) along with a patient (with ventricular dyssynchrony)selected to receive CRT (**Figure 4.5C**) are shown. In the healthy patient, with MRI frame 1 representing the reference configuration at end-diastole (end-filling), all sectors of the heart begin to contract as marked by a negative slope. At end-systole (end-contraction), each sector reaches a minimum at roughly the same frame and then follows a positive slope to return to a value of 0 as the ventricle again fills with blood. However, these curves differ in patients who are selected to undergo CRT and do not change in concert. For example, strain data of the CRT patient in **Figure 4.5C** is characterized by a delay in contraction within the anterior-lateral region and by bulging within the posterior and posterior-septal region.

Figure 4.5 Overview of Strain Data

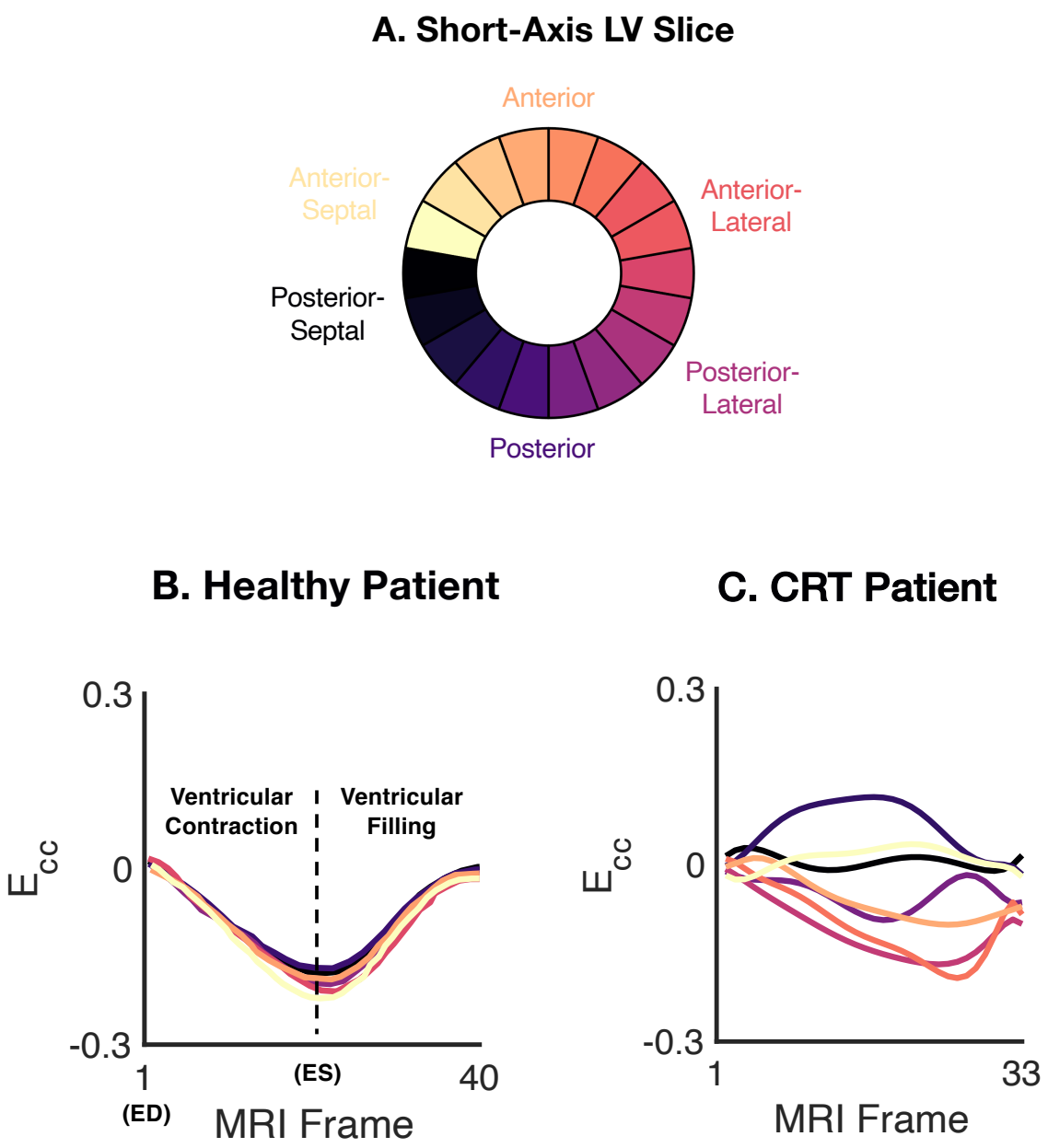

(A) The 18 different sectors of a short-axis slice of a ventricle are shown. Sector 1 is the posterior-septal region, sector 6 is the posterior sector, and so on. (B) The strain curve per sector of a healthy patient is shown, in which ED is end-diastole (end-filling) and ES is end-systole (end-contraction), and exhibits synchronous ventricular contraction (the curves lie on one another). (C) The strain curves of a patient selected for CRT are shown and do not overlay on another, demonstrating dyssynchronous contraction.

The pre- and post-CRT strain data of a responder (**Figure 4.6A**) and non-responder (**Figure 4.6B**) along with their respective delta strain curves are illustrated. While the pre-CRT strain data of the responder demonstrates a delay in contraction within the anterior-lateral region and bulging within the posterior and posterior-septal region, this patient's post-CRT strain data exhibits less delay in contraction, larger contraction (a more negative E_{cc}), and less bulging. The pre-CRT strain data of the non-responder is characterized by a delay in contraction within the anterior-lateral and posterior-lateral regions and by slight bulging within the posterior region. This patient's post-CRT strain data demonstrates more delay in contraction and more bulging. The delta strain curves show the difference in mechanics between the pre- and post-CRT strain. When comparing the delta strain curve of the responder to the non-responder, there are more negative minimums, and the average value of each curve seems to be greater. We derived metrics from these curves of all 25 patients, including the minimum, peak, and average of each curve, to characterize the changes in mechanics in each of the sectors and to relate them to long-term remodeling.

Figure 4.7 is a scatter plot of the minimum of each delta strain curve for every patient in this cohort. The line of best fit for each sector is also shown. Sectors 8 and 3 (which represent the posterior-lateral and posterior-septal sectors, respectively) exhibit promising trends between the minimum of the delta strain curves and LVESVI. Within both of these sectors, a small trend exists such that, as the minimum of the delta strain curve decreases, the LVESVI decreases. More negative minimums signify that the E_{cc} of the sector is more negative post-CRT than pre-CRT, which suggests that the sector contracts to a higher degree. A larger contraction may lead to better pump function and subsequently smaller end-diastolic volumes (EDV) over time. Based on mechanistic growth models, the growth stimulus would be negative as EDV (and thus fiber strain) is smaller after CRT than before. This negative growth stimulus may drive reverse cardiac growth. Scatter plots of the peak of the delta curve and the average of the delta strain curve versus Δ LVESVI were also constructed and shown in **Appendix 4.6.2**. Ultimately, changes in regional mechanics had less than expected predictive power (with respect to cardiac growth) on a patient-by-patient basis.

Figure 4.6 Strain Data of Responder vs. Non-Responder

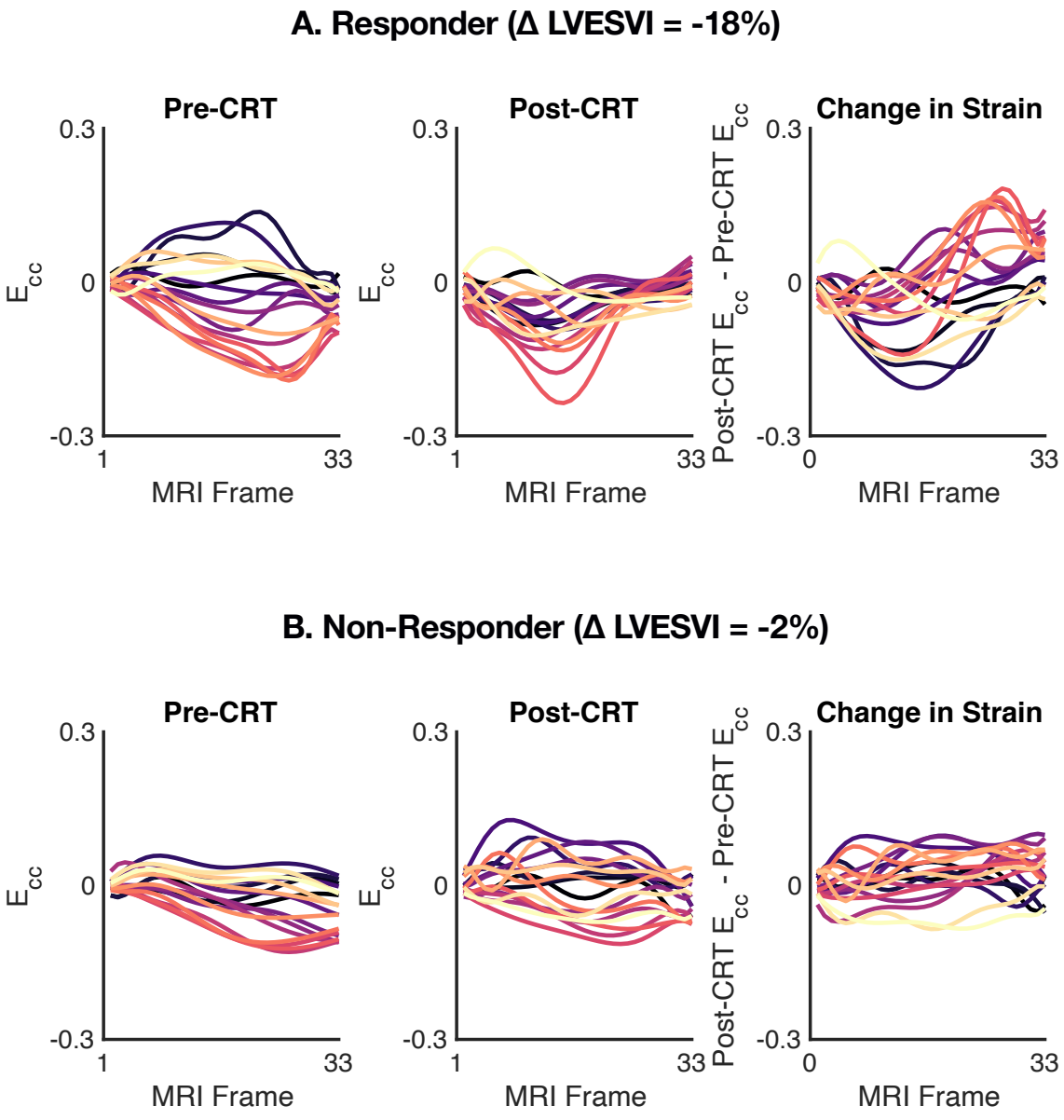

The strain curves before and after CRT along with the change in strain curves (delta strain curves) for a responder are shown in (B) and for a non-responder in (C). The delta strain curves show the difference in mechanics between the pre- and post-CRT strain. When comparing the delta strain curve of the responder to the non-responder, there were more negative minimums, and the average value of each curve seems to be greater.

Figure 4.7 Scatter Plot of the Minimums of the Delta Strain Curves

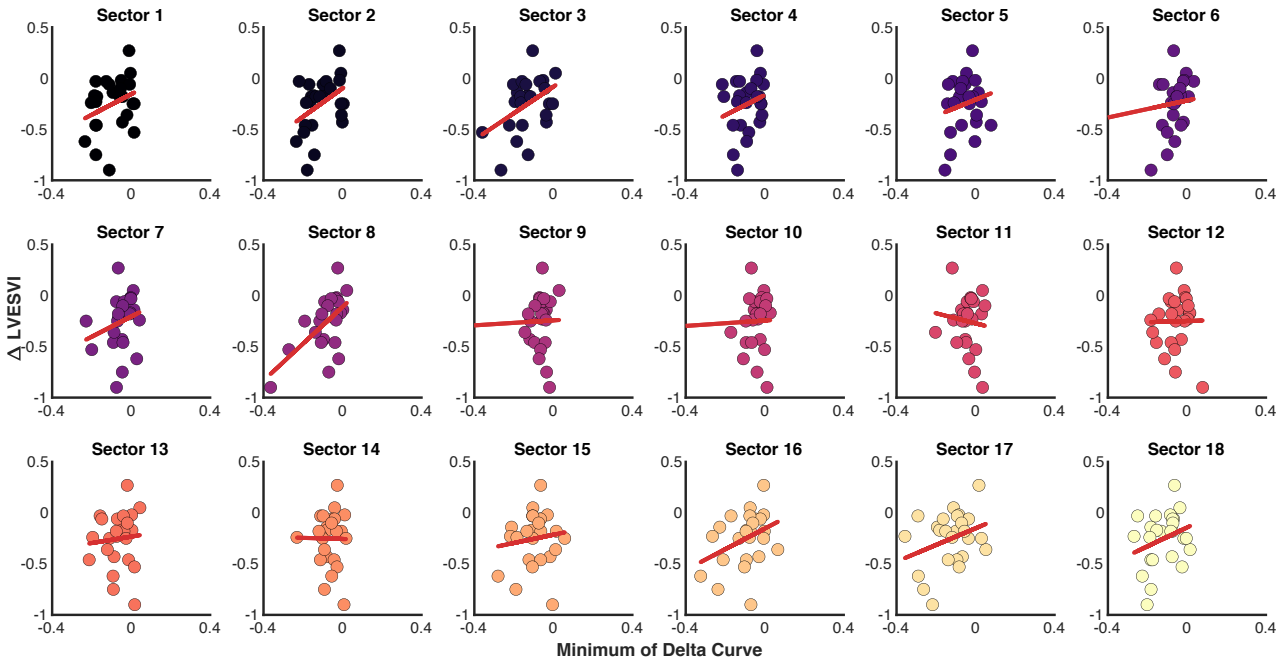

Scatter plots of the minimum of each delta strain curve per sector for every patient in this cohort are shown.

Finally, we compared our best strain-based predictor of Δ LVESVI (minimum of delta strain curve of sector 8) to the previously demonstrated best predictor of Δ LVESVI, which was the CURE-SVD score calculated before the procedure. CURE-SVD scores closer to 0 indicate more dyssynchronous ventricular contraction and are associated with greater reductions in Δ LVESVI compared to scores closer to 1. We fit a linear regression to the CURE-SVD scores of the 25 patients and Δ LVESVI, calculated its R^2 value, and compared it to that of the strain-based predictor. **Figure 4.8** shows the R^2 values for both predictors; while no strong correlation exists between either variable and Δ LVESVI, a promising trend exists such that smaller minimums of the delta strain curves result in greater reductions (more negative values) in LVESVI.

Figure 4.8 Scatter Comparing Predictors of Δ LVESVI: Strain-based vs. CURE-SVD

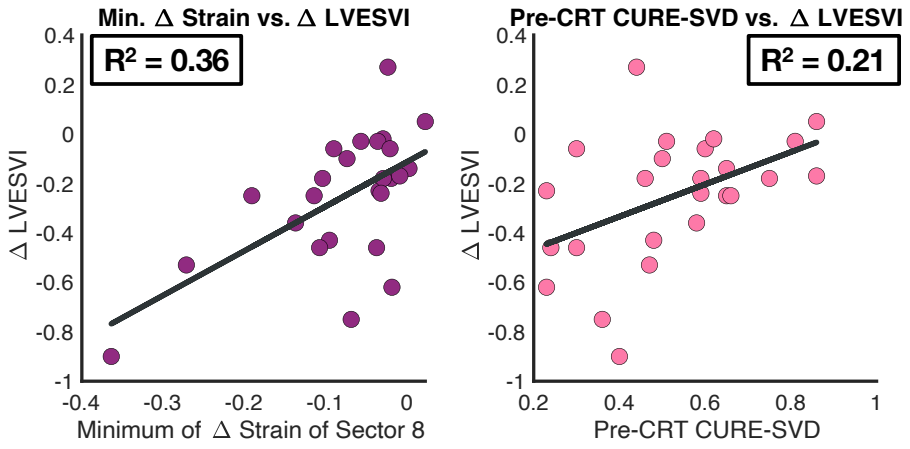

The R^2 values for both predictors show no strong correlation between either variable and Δ LVESVI.

4.4 Discussion

The goal of this chapter was to develop a statistical modeling framework to predict ventricular remodeling and patient outcome following cardiac resynchronization therapy (CRT). We gathered 39 clinical parameters (describing patient demographics, comorbid conditions, medication dosages, laboratory studies, vital signs, exercise capacity, ventricular assessments, and cardiac electrical function) from 198 patients before receiving CRT at the University of Virginia Health System. We then obtained the fractional change in LVESVI, BNP levels, and the change in peak VO_2 recorded 6 months after the procedure along with survival data from routine interrogations up to five years post-procedure. With this comprehensive data set, we were able to (1) to identify the pre-CRT information important in predicting post-CRT response measures and (2) utilize the pre- and post-CRT parameters to predict long-term survival. Additionally, for 25 patients within this cohort, we acquired mid-ventricular cardiac strain curves at both pre- and post-CRT time points. We ultimately demonstrated that changes in regional mechanics had less than expected predictive power (with respect to cardiac growth) on a patient-by-patient basis.

4.4.1 Linear Regression Identifies Pre-CRT Parameters Most Strongly Associated with Response Measures

The stepwise linear regressions identified the pre-CRT parameters most strongly associated with each of the three response measures. The best predictor of post-CRT BNP levels was pre-CRT BNP levels, and the best predictor of Δ peak VO_2 was the peak VO_2 measured before the procedure. These results show that the baseline values of the response measures greatly influence their change following CRT, suggesting that patients with less severe heart failure (lower BNP levels and higher peak VO_2 values) at the time of CRT will have more favorable outcomes to the therapy. Early intervention may be crucial for preventing poor outcomes.

The presence of ischemic cardiomyopathy (ICM) was significant to both Δ LVESVI and BNPP response measures. This parameter resulted in less favorable LVESVI response as a '1' for this variable drove the predicted value of Δ LVESVI to be more positive (due to the positive coefficient estimate). On the other hand, the presence of ischemic cardiomyopathy was associated with a more favorable BNP response due to the negative coefficient estimate that results in lower post-CRT BNP levels. This highlights the complicated role ischemia plays in ventricular dyssynchrony and CRT response. Ischemia may inhibit electrical signaling and result in poor remodeling especially if scar is present and the ventricular lead is placed within this region. Further, ischemia increases end-diastolic pressure which subsequently increases ventricular wall stress, and BNP is released in response to this increase in wall stress[115]. Thus, in patients with ICM, CRT may decrease wall stress to a greater degree than in patients without ICM and result in more favorable BNP outcomes.

In our final attempt to elucidate the pre-CRT parameters most important in determining the 6-month response measures, we implemented a multivariate multiple linear regression in which the dependent variable was the linear combination of the response measures and the dependent/predictor variables were those from the individual linear regression models. BNP, pre-CRT peak VO_2, and CURE-SVD were the most significant variables, agreeing with the results from the individual regressions. Interestingly, right ventricular assessment parameters (RVEF and RVEDVI) were significant in the multiple regression analysis along with the individual linear regressions for Δ LVESVI and BNPP. Few studies have examined the relationship between the function (and size) of the RV and dyssynchrony caused by LBBB[116, 117]. This is important because

the contraction of the LV has been shown to be responsible for about 20-40% of RV systolic pressure and volume load[118]. Therefore, since LBBB impairs LV function, it may also impair RV function. Thus, assessing RV function and size provides additional information on the severity of dyssynchronous heart failure and can aid in predicting CRT outcome, as shown in this chapter. Our results agree with other studies and suggests that RV function informs CRT response[116, 117].

4.4.2 Clustering of Post-CRT Response Measures & Long-Term Survival

We utilized a clustering approach, with the three response measures (Δ LVESVI, BNP levels, and Δ peak VO_2) gathered 6-months post-CRT as input, to predict the long-term survival of patients following the therapy. Initially, we implemented the common k-means clustering model and our results are shown in the **Appendix 4.6.1**. K-means clustering simply divides a data set into *k* clusters in a way that attempts to minimize the average Euclidean distance from a point to the center of its cluster and makes no assumption about how the data points were generated. We observed that the k-means model with the optimal number of clusters did not generate survival curves with significant separation, and consequently decided to implement the slightly more complex Gaussian mixture model (GMM). The GMM assumes that the clusters within a data set were generated by normal Gaussian distribution. These models allow for the shapes of the clusters to be elliptical and overlapping, as opposed to those formed by k-means in which the clusters are spherical. Gaussian mixture models are also probabilistic, which allows us to express the confidence of a point belonging to one specific cluster. While GMMs are robust, they are computationally more expensive and may converge to a local minimum. However, given the size of our data set and our results, these problems were avoided. Our optimal GMM was able to stratify the patient population into 3 distinct groups, and their survival curves were significantly separated, suggesting that there may be three inherent groups of CRT responders (those who improve, those who do not improve, and those who worsen).

Upon examination of the clusters (and the p-value between groups), BNPP seemed to be a strong separator. BNP has been previously shown to reflect end-diastolic wall stress in patients with systolic heart failure and patients with diastolic heart failure[115]. This parameter has become more popular in clinical assessment and management of HF[119, 120] and has been previously shown to provide important prognostic implications in patients with mildly symptomatic HF who receive CRT[121]; our results further highlight its importance.

Finally, because it may be critical to predict the group of patients at highest mortality risk following CRT, patients in Group 1 and 2 were condensed into a single group while Group 3 patients remained the same, and their survival curves were generated. Again, significant separation was demonstrated; therefore, this model may serve as a helpful tool for clinicians in assessing long-term CRT outcome and referring patients in Group 3 to more advanced HF therapies such as mechanical circulatory support and heart transplantation to improve prognosis.

4.4.3 Testing if Strain Can Predict Reverse Growth

We tested the popular biomechanics hypothesis that changes in regional mechanics can predict changes in cardiac hypertrophy. Numerous mechanistic growth laws operate under the assumption that a change in mechanical signal (strain or stress) from a biological tissue's homeostatic state triggers growth[59]. This change in mechanical stimuli can be positive and cause growth. For example, in the case of volume overload, the end-diastolic strain of the ventricle is increased, and the heart chamber dilates (grows in the fiber direction). In the case of HF patients who respond to CRT, the change in mechanical signal is negative and reverses growth. The diastolic strain within these ventricles are already large due to HF and dyssynchrony, and it is hypothesized that, since CRT resynchronizes contraction, it decreases fiber strain and subsequently triggers reverse growth.

With the available data set of cardiac strain curves measured at pre- and post-CRT, we were able to test this hypothesis. We computed the difference between these curves (delta strain curves), which is equivalently the change in mechanics caused by CRT, and attempted to correlate different metrics that characterize these curves with Δ LVESVI (ventricular size). Furthermore, we compared one strain-based predictor to CURE-SVD, the predictor shown previously to be most significantly associated with Δ LVESV. Ultimately, changes in regional mechanics had less than expected predictive power (with respect to cardiac growth) on a patient-by-patient basis. This suggests that considering only mechanics may not be sufficient when predicting the reversal of growth caused by CRT. A model that incorporates more factors, such as hormonal activity reflected in BNP measurements, is likely needed for successful cardiac growth prediction.

4.4.4 Model Limitations

Several limitations within this chapter should be recognized. The results of the models are confined to the selected population of patients from a single center (UVA Health System). While our conclusions would most likely hold true, it would be advantageous to apply our framework to a cohort of patients who received CRT at another institution to ensure robustness of our approach. Furthermore, a common limitation of cardiac imaging studies applies to our study as well: the quality of the data relies on the quality of acquired images. We minimized the consequences of this limitation by selecting images, no matter the modality, with the best quality when calculating parameters of interest. For example, DENSE-MR images for approximately 4% of the patients were of such poor quality that we could not use them to calculate CURE-SVD score. Instead, we substituted DENSE-MRI with cine images and utilized strain tracking software to generate strain curves and ultimately calculate CURE-SVD. Another limitation involved information about ventricular scars. We included the presence of LGE (a binary variable) to inform the models of whether the patient had scar, but we lacked more detailed information such as scar mass and location. Finally, we neglected the pacing protocol each patient received, which can be either biventricular pacing (pacemaker leads are placed on both the right and left ventricle) or left ventricular pacing (leads are placed only on the LV), and this may influence CRT outcome. We plan on including these parameters in future analyses.

4.5 Conclusion

Our linear regression models were able to identify clinical parameters gathered before CRT that were strongly associated with CRT response measures calculated 6 months after the procedure. Some of these important parameters included the CURE-SVD score, BNP levels, peak VO_2, the presence of ischemic cardiomyopathy, RVEF, and RVEDVI. Our results suggest that the consideration of these variables is crucial when evaluating the clinical benefit of patients selected to receive CRT. Our clustering model was able to stratify our cohort of patients into three distinct groups based on their 6-month response measures. This model could be used in the clinic to help physicians determine the patients most at risk for a cardiac event five years after CRT and plan for a left-ventricular assistive device or heart transplant. We were also able to accurately predict whether a patient would be alive four years after CRT with information gathered pre- and post-procedure. Finally, we tested one of the fundamental theories in biomechanics: changes in

mechanics leads to the growth of biological tissue. We obtained cardiac strain curves before and after CRT, calculated the actual change in mechanics (the delta strain curves), and demonstrated that changes in regional mechanics had less than expected predictive power yet show promising trends.

4.6 Appendix

4.6.1 K-Means Clustering

In our first attempt at clustering the cohort of patients based on the 6-month response measures, we implemented the k-means model. We computed the optimal number of clusters k with the elbow method. We ran the k-means model with k ranging from 1 to 14 and, for each model, calculated sum of the squared Euclidean distances (SSD) all points to the center of their clusters. The elbow method suggests picking the value of k at which the SSD starts to decrease in a linear fashion. In our case, this occurred at $k = 3$ as shown in **Figure 4.9A**. The three clusters are shown in **Figure 4.9B**, and the resulting survival curves constructed with a Kaplan-Meier analysis are show in **Figure 4.9C**. The separation between the curve for Group 1 is significant compared to Groups 2 and 3; however, the survival curves for Groups 2 and 3 are very similar, which is the reason we implemented the GMM.

Figure 4.9 K-Means Clustering

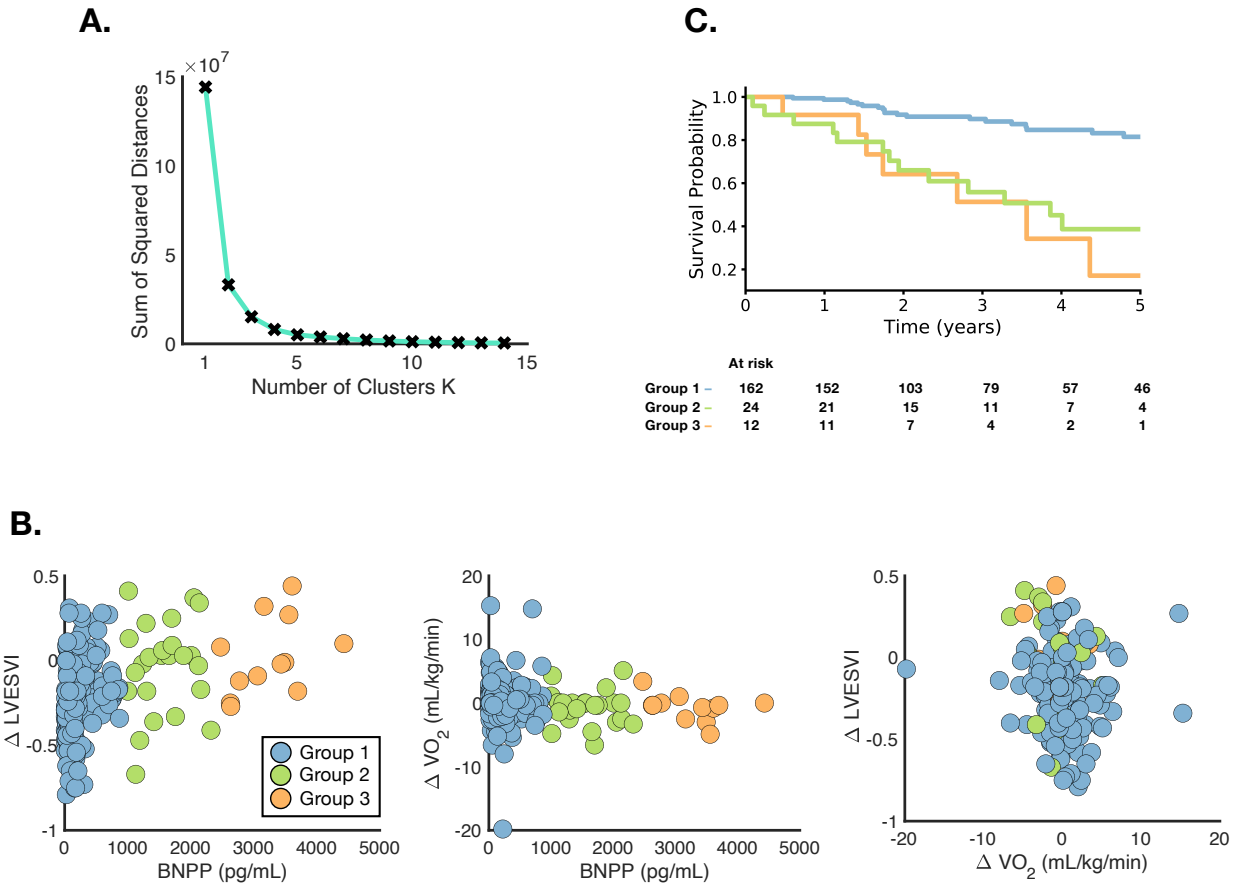

The k-means model stratified patients into three clusters. However, the survival probability curves were not significanty separated.

4.6.2 Scatter Plots of the Peak and Average of the Delta Strain Curves VS. Δ LVESVI

Figure 4.10 Scatter plots of the peak of the delta curve and the average of the delta curve versus Δ LVESVI

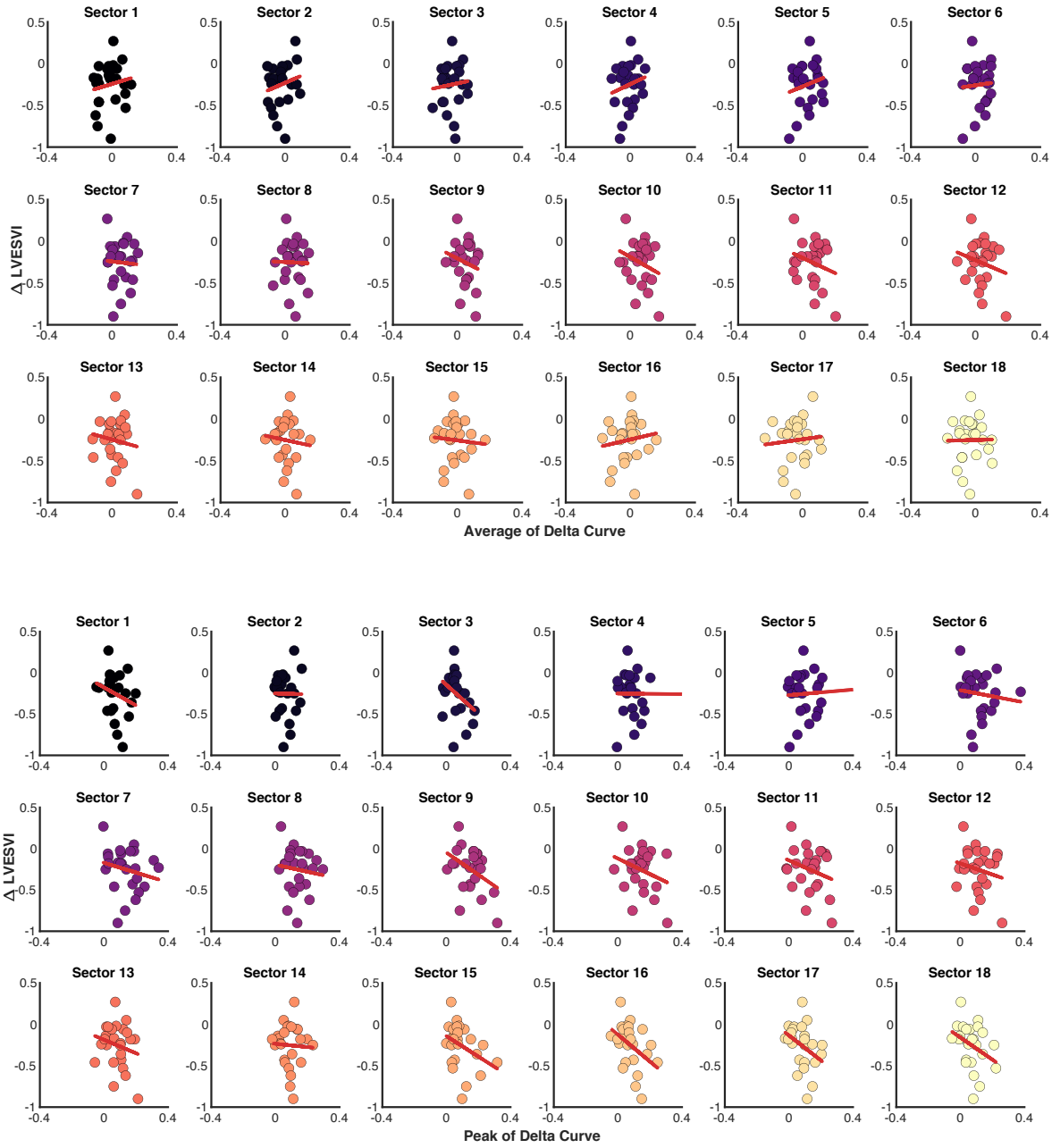

Scatter plots of the average and peak of each delta strain curve per sector for every patient in this cohort are shown.

Chapter 5

5 Conclusion & Future Directions

Computational modeling is a powerful tool for simulating cardiac injury and therapy. Researchers build biophysical mechanistic models by assembling equations that govern a physical system, validating predictions against observed data, and in many cases designing new experiments to measure key parameters. These models are often used to develop a better understanding of a system and to test the effect of a change or intervention within a system. Researchers also employ statistical models to uncover patterns within data generated by a physical system, which aids in predicting the likelihood of specific outcomes given a set of inputs. These models are often used to investigate and quantify the association of several different factors with an outcome of interest. Both modeling approaches provide a low-risk, low-cost, highly iterative framework that allows researchers to gain a better understanding of cardiac diseases and consider the likely impact of potential therapies. I advanced the current state of cardiac research in this dissertation by utilizing computational modeling to predict the progression and regression of heart growth with: (1) a biophysical mechanistic model of the infarcted left ventricle (LV) that predicted remodeling during post-infarction healing and (2) a statistical modeling framework that predicted patient outcome following CRT. While my work explored the concept that regional mechanics can be used to predict cardiac growth, it the future it could be extended to better capture the effects of hormones, intracellular signaling, and drug therapies that target relevant receptors and signaling pathways.

In Chapter 2, we built a biophysical model of the rat LV and explored different approaches to predicting changes in infarct scar dimensions and composition during infarct healing. In Chapter 3, we extended this model to predict the amount of growth that occurs in the non-infarcted (remote) region. Our most striking results included (1) the difficulty in predicting and interpreting scar dimensions over time, (2) the notable impact of hemodynamics on post-infarction LV dilation, and (3) the importance of scar stiffening in determining predicted cardiac growth following myocardial infarction (MI); these results provide guidance to the direction of future work.

With respect to scar formation and dimensions, the implementation of an agent-based model that uses autonomous agents (i.e. fibroblasts) to simulate variations in the deposition rate, accumulation, and orientation of collagen within the scar region may better mimic scar physiology compared to our single-element FE approach. Our FE LV model could be coupled to a recently published ABM of collagen deposition[43, 56, 57], and scar remodeling simulations could be re-run and scar dimensions re-calculated. However, our results suggest that a truly mechanistic model that can explain changes in infarct geometry during healing will also need to consider the three-dimensional arrangement of tissue components and how those components interact under cyclic mechanical loading. As a myocyte necroses and the membrane is disrupted, cytoplasm is no longer physically confined; the material(s) occupying that space and the loss of membrane integrity may influence the arrangement of the surrounding cells and extracellular matrix. Conceptually, it may seem reasonable that replacing relatively short and thick myocytes with much longer and thinner collagen fibers would result in a thinner scar with a larger surface area, but without a mechanistic model of the process it will be very difficult to predict how interventions such as polymer injection will alter remodeling. Development of a three-dimensional, space-filling, mechanically realistic model of healing infarct tissue would be a significant and worthwhile project potentially worthy of a doctoral thesis.

In terms of the important role hemodynamics play in cardiac growth, connecting the FE model to a circulation model of systemic and pulmonary circulation[122, 123] would better account for changes in hemodynamic loading observed over time following MI and may lead to more realistic growth patterns. Many circulatory models accurately describe the short-term changes in preload (i.e. the amount of blood in the ventricle at end-filling) and afterload (i.e. the resistance the ventricle must overcome to pump blood). However, models of long-term growth must include circulatory systems that account for the realistic regulation of the circulation over time[32, 124, 125]. Some features of circulatory regulation, like blood volume regulation by the kidney, are important targets of drug therapies – including ACE inhibitors and loop diuretics - often prescribed to patients with heart failure. Representing such mechanisms is especially important when attempting to make clinically relevant, long-term predictions.

Finally, as for our finding that scar stiffness influences remote growth, therapies that alter the stiffness of the scar region can be explored. For example, Ifkovits[13] demonstrated that injection of a stiff hydrogel into the scar region produced a smaller infarct area compared to a

more compliant hydrogel. Based on our conclusion from Chapter 3 that stiffer infarcts lead to reduced LV dilation, interesting future work includes re-performing Ifkovits' experiments but focusing on the growth of the remote myocardium. These experiments would serve as independent validation of our model prediction, and they have the exciting potential for translation into the clinic.

In Chapter 4, we took a different approach to predict the regression of cardiac growth. Rather than using biophysical mechanistic modeling, we employed statistical models to quantify the association of numerous patient-specific factors with ventricular remodeling and outcome following CRT. Our linear regression models were able to identify clinical parameters gathered before CRT that were strongly associated with response measures calculated 6 months post-CRT. Our clustering model was able to stratify our cohort of patients into three groups with distinct survival probabilities. We also demonstrated that changes in regional mechanics had less than expected predictive power. The framework in this chapter could be extended in terms of complexity. For example, a convolutional neural network could be optimized to predict the degree of ventricular remodeling using DENSE-MRI as input. A high-quality model with adequate prediction accuracy, sensitivity, and specificity would assumably require a larger sample size[126], so more DENSE-MRI would be needed. However, this approach can take as input the full dimensionality of the data and allows the model to determine the information most important in predicting reverse growth. It may reveal aspects of cardiac strain novel to predicting CRT response that CURE-SVD cannot capture due to its reduction in dimensionality[110].

Because computational modeling is low-risk, low-cost, and highly iterative, its application to cardiovascular research is endless. We could even switch up our modeling approaches, using statistical modeling to predict ventricular growth following MI and biophysical mechanistic modeling to predict regression of cardiac growth following CRT. If sufficient data describing ventricular growth post-MI exist in the presence of multiple scar sizes and stiffnesses and hemodynamic conditions, linear regression and other supervised statistical models could be applied to uncover the combinations of parameters that lead to specific cardiac growth patterns. Additionally, a biophysical mechanistic model to predict regression of cardiac growth following CRT may be favorable. Integrating a cell-signaling model that incorporates pathways involving BNP (the hormone we showed to be significant in predicting CRT response) with a mechanics-based model that addresses the amount of dyssynchrony represented by CURE-SVD (another

parameter we showed to be significant in predicting CRT response) provides a promising approach for predicting cardiac remodeling in cases in which mechanics, hormones, and drug treatments interact[54, 127].

Overall, the work in my dissertation explored the prevailing concept in biomechanics that the long-term remodeling of mechanically active biologic tissues such as the myocardium can be predicted based on regional mechanics, using two complementary approaches: biophysical models that explicitly link mechanics to remodeling, and statistical models that inform how much of the observed remodeling can be explained by mechanics. In the finite-element model, I was able to accurately predict growth during volume overload and MI using only regional mechanics. However, in my statistical model, changes in regional mechanics had less than expected predictive power on a patient-by-patient basis. One explanation of these findings is that, in animal models where sudden changes in loading occur, mechanics-based growth laws are successful because the factors that affect growth, like mechanics and hormones, are homogenous at baseline and change in unison over time. In other words, the multiple equations that represent mechanics and hormones rise and fall in parallel, making growth predictions more straightforward. Conversely, in patients being treated at different ages and stages of disease, who are taking different combinations and doses of medications, mechanics and hormonal activity vary much more at baseline and may all change differently following treatment. Therefore, a model that represents more of those independent factors is likely needed for successful cardiac growth prediction; in other words, a more sophisticated biophysical mechanistic model or a statistical model trained on much larger datasets to account for a sufficient number of growth altering factors may be necessary to predict the long-term remodeling of biologic tissues in patients.

6 References

[1] H. Huxley and J. Hanson, “Changes in the Cross-Striations of Muscle during Contraction and Stretch and their Structural Interpretation,” *Nature*, vol. 173, no. 4412, pp. 973–976, May 1954, doi: 10.1038/173973a0.

[2] E. W. Hsu, A. L. Muzikant, S. A. Matulevicius, R. C. Penland, and C. S. Henriquez, “Magnetic resonance myocardial fiber-orientation mapping with direct histological correlation,” *Am. J. Physiol.-Heart Circ. Physiol.*, vol. 274, no. 5, pp. H1627–H1634, May 1998, doi: 10.1152/ajpheart.1998.274.5.H1627.

[3] A. F. Huxley and R. Niedergerke, “Structural Changes in Muscle During Contraction: Interference Microscopy of Living Muscle Fibres,” *Nature*, vol. 173, no. 4412, pp. 971–973, May 1954, doi: 10.1038/173971a0.

[4] M. H. Drazner, “The Progression of Hypertensive Heart Disease,” *Circulation*, vol. 123, no. 3, pp. 327–334, Jan. 2011, doi: 10.1161/CIRCULATIONAHA.108.845792.

[5] E. Surkova *et al.*, “Left bundle branch block: from cardiac mechanics to clinical and diagnostic challenges,” *EP Eur.*, vol. 19, no. 8, pp. 1251–1271, Aug. 2017, doi: 10.1093/europace/eux061.

[6] O. V. Savinova and A. M. Gerdes, “Myocyte Changes in Heart Failure,” *Heart Fail. Clin.*, vol. 8, no. 1, pp. 1–6, Jan. 2012, doi: 10.1016/j.hfc.2011.08.004.

[7] S. S. Virani *et al.*, “Heart Disease and Stroke Statistics—2020 Update: A Report From the American Heart Association,” *Circulation*, vol. 141, no. 9, pp. e139–e596, Mar. 2020, doi: 10.1161/CIR.0000000000000757.

[8] P. Libby and P. Theroux, “Pathophysiology of Coronary Artery Disease,” *Circulation*, vol. 111, no. 25, pp. 3481–3488, Jun. 2005, doi: 10.1161/CIRCULATIONAHA.105.537878.

[9] E. Anter, M. Jessup, and D. J. Callans, “Atrial Fibrillation and Heart Failure: Treatment Considerations for a Dual Epidemic,” *Circulation*, vol. 119, no. 18, pp. 2516–2525, May 2009, doi: 10.1161/CIRCULATIONAHA.108.821306.

[10] W. H. Gaasch and T. E. Meyer, “Left Ventricular Response to Mitral Regurgitation: Implications for Management,” *Circulation*, vol. 118, no. 22, pp. 2298–2303, Nov. 2008, doi: 10.1161/CIRCULATIONAHA.107.755942.

[11] C. M. Witzenburg and J. W. Holmes, “Biomechanics of Myocardial Ischemia and Infarction,” in *Biomechanics: Trends in Modeling and Simulation*, vol. 20, G. A. Holzapfel and R. W. Ogden, Eds. Cham: Springer International Publishing, 2017, pp. 233–269. doi: 10.1007/978-3-319-41475-1_6.

[12] J. W. Holmes, T. K. Borg, and J. W. Covell, “Structure and Mechanics of Healing Myocardial Infarcts,” *Annu. Rev. Biomed. Eng.*, vol. 7, no. 1, pp. 223–253, Aug. 2005, doi: 10.1146/annurev.bioeng.7.060804.100453.

[13] J. L. Ifkovits *et al.*, “Injectable hydrogel properties influence infarct expansion and extent of postinfarction left ventricular remodeling in an ovine model,” *Proc. Natl. Acad. Sci.*, vol. 107, no. 25, pp. 11507–11512, Jun. 2010, doi: 10.1073/pnas.1004097107.

[14] J. Leor *et al.*, “Intracoronary Injection of In Situ Forming Alginate Hydrogel Reverses Left Ventricular Remodeling After Myocardial Infarction in Swine,” *J. Am. Coll. Cardiol.*, vol. 54, no. 11, pp. 1014–1023, Sep. 2009, doi: 10.1016/j.jacc.2009.06.010.

[15] A. C. Estrada, K. Yoshida, S. A. Clarke, and J. W. Holmes, “Longitudinal Reinforcement of Acute Myocardial Infarcts Improves Function by Transmurally Redistributing Stretch and Stress,” *J. Biomech. Eng.*, vol. 142, no. 2, p. 021009, Feb. 2020, doi: 10.1115/1.4044030.

[16] K. C. Bilchick *et al.*, “Impact of Mechanical Activation, Scar, and Electrical Timing on Cardiac Resynchronization Therapy Response and Clinical Outcomes,” *J. Am. Coll. Cardiol.*, vol. 63, no. 16, pp. 1657–1666, Apr. 2014, doi: 10.1016/j.jacc.2014.02.533.

[17] R. L. Winslow, N. Trayanova, D. Geman, and M. I. Miller, “Computational Medicine: Translating Models to Clinical Care,” *Sci. Transl. Med.*, vol. 4, no. 158, pp. 158rv11-158rv11, Oct. 2012, doi: 10.1126/scitranslmed.3003528.

[18] G. C. Y. Peng *et al.*, “Multiscale Modeling Meets Machine Learning: What Can We Learn?,” *Arch. Comput. Methods Eng.*, vol. 28, no. 3, pp. 1017–1037, May 2021, doi: 10.1007/s11831-020-09405-5.

[19] K. A. Ryall, D. O. Holland, K. A. Delaney, M. J. Kraeutler, A. J. Parker, and J. J. Saucerman, “Network Reconstruction and Systems Analysis of Cardiac Myocyte Hypertrophy Signaling,” *J. Biol. Chem.*, vol. 287, no. 50, pp. 42259–42268, Dec. 2012, doi: 10.1074/jbc.M112.382937.

[20] C. M. Witzenburg and J. W. Holmes, “Predicting the Time Course of Ventricular Dilation and Thickening Using a Rapid Compartmental Model,” *J Cardiovasc. Transl. Res.*, vol. 11, no. 2, pp. 109–122, Apr. 2018, doi: 10.1007/s12265-018-9793-1.

[21] J. M. Guccione, K. D. Costa, and A. D. McCulloch, “Finite element stress analysis of left ventricular mechanics in the beating dog heart,” *J. Biomech.*, vol. 28, no. 10, pp. 1167–1177, Oct. 1995, doi: 10.1016/0021-9290(94)00174-3.

[22] K. Yoshida, A. D. McCulloch, J. H. Omens, and J. W. Holmes, “Predictions of hypertrophy and its regression in response to pressure overload,” *Biomech. Model. Mechanobiol.*, vol. 19, no. 3, pp. 1079–1089, Jun. 2020, doi: 10.1007/s10237-019-01271-w.

[23] A. Gertych *et al.*, “Convolutional neural networks can accurately distinguish four histologic growth patterns of lung adenocarcinoma in digital slides,” *Sci. Rep.*, vol. 9, no. 1, p. 1483, Dec. 2019, doi: 10.1038/s41598-018-37638-9.

[24] R. P. K. Poudel, P. Lamata, and G. Montana, “Recurrent Fully Convolutional Neural Networks for Multi-slice MRI Cardiac Segmentation,” in *Reconstruction, Segmentation, and Analysis of Medical Images*, vol. 10129, M. A. Zuluaga, K. Bhatia, B. Kainz, M. H. Moghari, and D. F. Pace, Eds. Cham: Springer International Publishing, 2017, pp. 83–94. doi: 10.1007/978-3-319-52280-7_8.

[25] N. Sharpe, “Remodeling Following Infarction,” *HEART Fail. Manag.*, p. 7.

[26] D. Maclean, M. C. Fishbein, E. Braunwald, and P. R. Maroko, “Long-Term Preservation of Ischemic Myocardium after Experimental Coronary Artery Occlusion,” *J. Clin. Invest.*, vol. 61, no. 3, pp. 541–551, Mar. 1978, doi: 10.1172/JCI108965.

[27] M. A. Pfeffer and E. Braunwald, “Ventricular remodeling after myocardial infarction. Experimental observations and clinical implications.,” *Circulation*, vol. 81, no. 4, pp. 1161–1172, Apr. 1990, doi: 10.1161/01.CIR.81.4.1161.

[28] G. M. Fomovsky and J. W. Holmes, “Evolution of scar structure, mechanics, and ventricular function after myocardial infarction in the rat,” *Am. J. Physiol.-Heart Circ. Physiol.*, vol. 298, no. 1, pp. H221–H228, Jan. 2010, doi: 10.1152/ajpheart.00495.2009.

[29] L. R. Caggiano, J.-J. Lee, and J. W. Holmes, “Surgical reinforcement alters collagen alignment and turnover in healing myocardial infarcts,” *Am. J. Physiol.-Heart Circ. Physiol.*, vol. 315, no. 4, pp. H1041–H1050, Oct. 2018, doi: 10.1152/ajpheart.00088.2018.

[30] J. D. Humphrey and K. Rajagopal, “A constrained mixture model for growth and remodeling of soft tissues,” *Math. Models Methods Appl. Sci.*, vol. 12, no. 03, pp. 407–430, 2002.

[31] M. A. Pfeffer *et al.*, “Myocardial infarct size and ventricular function in rats.,” *Circ. Res.*, vol. 44, no. 4, pp. 503–512, Apr. 1979, doi: 10.1161/01.RES.44.4.503.

[32] C. M. Witzenburg and J. W. Holmes, “The Impact of Hemodynamic Reflex Compensation Following Myocardial Infarction on Subsequent Ventricular Remodeling,” *J. Biomech. Eng.*, vol. 141, no. 9, p. 091010, Sep. 2019, doi: 10.1115/1.4043867.

[33] B. I. Jugdutt, M. I. Khan, S. J. Jugdutt, and G. E. Blinston, “Effect of prolonged inotropic stimulation on ventricular remodeling during healing after myocardial infarction in the dog: mechanistic insights,” *J. Am. Coll. Cardiol.*, vol. 27, no. 7, pp. 1787–1795, 1996.

[34] B. I. Jugdutt, M. I. Khan, S. J. Jugdutt, and G. E. Blinston, “Effect of enalapril on ventricular remodeling and function during healing after anterior myocardial infarction in the dog,” *Circulation*, vol. 91, no. 3, pp. 802–812, 1995.

[35] B. A. French and C. M. Kramer, “Mechanisms of postinfarct left ventricular remodeling,” *Drug Discov. Today Dis. Mech.*, vol. 4, no. 3, pp. 185–196, 2007.

[36] J. M. Pfeffer, M. A. Pfeffer, P. J. Fletcher, and E. Braunwald, “Progressive ventricular remodeling in rat with myocardial infarction,” *Am. J. Physiol.-Heart Circ. Physiol.*, vol. 260, no. 5, pp. H1406–H1414, 1991.

[37] M. P. Boyle and H. F. Weisman, “Limitation of infarct expansion and ventricular remodeling by late reperfusion. Study of time course and mechanism in a rat model.,” *Circulation*, vol. 88, no. 6, pp. 2872–2883, 1993.

[38] S. E. Litwin, S. E. Katz, J. P. Morgan, and P. S. Douglas, “Serial echocardiographic assessment of left ventricular geometry and function after large myocardial infarction in the rat.,” *Circulation*, vol. 89, no. 1, pp. 345–354, 1994.

[39] M. Saeed *et al.*, “Left ventricular remodeling after infarction: sequential MR imaging with oral nicorandil therapy in rat model,” *Radiology*, vol. 224, no. 3, pp. 830–837, 2002.

[40] I. Ahmet, E. G. Lakatta, and M. I. Talan, “Pharmacological stimulation of β 2-adrenergic receptors (β 2 AR) enhances therapeutic effectiveness of β 1 AR blockade in rodent dilated ischemic cardiomyopathy,” *Heart Fail. Rev.*, vol. 10, no. 4, pp. 289–296, 2005.

[41] I. Ahmet, M. Krawczyk, P. Heller, C. Moon, E. G. Lakatta, and M. I. Talan, “Beneficial effects of chronic pharmacological manipulation of β-adrenoreceptor subtype signaling in rodent dilated ischemic cardiomyopathy,” *Circulation*, vol. 110, no. 9, pp. 1083–1090, 2004.

[42] A. Miranda *et al.*, “Time course of echocardiographic and electrocardiographic parameters in myocardial infarct in rats,” *An. Acad. Bras. Ciênc.*, vol. 79, pp. 639–648, 2007.

[43] W. J. Richardson and J. W. Holmes, “Why is infarct expansion such an elusive therapeutic target?,” *J Cardiovasc. Transl. Res.*, vol. 8, no. 7, pp. 421–430, 2015.

[44] J. R. McGarvey *et al.*, “Temporal changes in infarct material properties: an in vivo assessment using magnetic resonance imaging and finite element simulations,” *Ann. Thorac. Surg.*, vol. 100, no. 2, pp. 582–589, 2015.

[45] M. Latorre and J. D. Humphrey, “Fast, rate-independent, finite element implementation of a 3D constrained mixture model of soft tissue growth and remodeling,” *Comput. Methods Appl. Mech. Eng.*, vol. 368, p. 113156, 2020.

[46] S. T. Wall, J. C. Walker, K. E. Healy, M. B. Ratcliffe, and J. M. Guccione, “Theoretical impact of the injection of material into the myocardium: a finite element model simulation,” *Circulation*, vol. 114, no. 24, pp. 2627–2635, 2006.

[47] S. A. Maas, B. J. Ellis, G. A. Ateshian, and J. A. Weiss, “FEBio: finite elements for biomechanics,” *J. Biomech. Eng.*, vol. 134, no. 1, 2012.

[48] G. A. Ateshian and K. D. Costa, “A frame-invariant formulation of Fung elasticity,” *J. Biomech.*, vol. 42, no. 6, pp. 781–785, 2009.

[49] J. M. Guccione, A. D. McCulloch, and L. K. Waldman, “Passive material properties of intact ventricular myocardium determined from a cylindrical model,” 1991.

[50] K. D. Costa, J. W. Holmes, and A. D. McCulloch, “Modelling cardiac mechanical properties in three dimensions,” *Philos. Trans. R. Soc. Lond. Ser. Math. Phys. Eng. Sci.*, vol. 359, no. 1783, pp. 1233–1250, 2001.

[51] J. D. Humphrey, *Cardiovascular solid mechanics: cells, tissues, and organs*. Springer Science & Business Media, 2013.

[52] J. H. Omens, D. A. MacKenna, and A. D. McCulloch, “Measurement of strain and analysis of stress in resting rat left ventricular myocardium,” *J. Biomech.*, vol. 26, no. 6, pp. 665–676, 1993.

[53] E. K. Rodriguez, A. Hoger, and A. D. McCulloch, “Stress-dependent finite growth in soft elastic tissues,” *J. Biomech.*, vol. 27, no. 4, pp. 455–467, 1994.

[54] A. C. Estrada, K. Yoshida, J. J. Saucerman, and J. W. Holmes, “A multiscale model of cardiac concentric hypertrophy incorporating both mechanical and hormonal drivers of growth,” *Biomech. Model. Mechanobiol.*, vol. 20, no. 1, pp. 293–307, 2021.

[55] P. J. Hunter, A. D. McCulloch, and H. E. D. J. ter Keurs, “Modelling the mechanical properties of cardiac muscle,” *Prog. Biophys. Mol. Biol.*, vol. 69, no. 2–3, pp. 289–331, Mar. 1998, doi: 10.1016/S0079-6107(98)00013-3.

[56] A. D. Rouillard and J. W. Holmes, “Mechanical regulation of fibroblast migration and collagen remodelling in healing myocardial infarcts,” *J. Physiol.*, vol. 590, no. 18, pp. 4585–4602, 2012.

[57] S. M. Rikard *et al.*, “Multiscale coupling of an agent-based model of tissue fibrosis and a logic-based model of intracellular signaling,” *Front. Physiol.*, vol. 10, p. 1481, 2019.

[58] I. Kehat *et al.*, “Extracellular Signal-Regulated Kinases 1 and 2 Regulate the Balance Between Eccentric and Concentric Cardiac Growth,” *Circ. Res.*, vol. 108, no. 2, pp. 176–183, Jan. 2011, doi: 10.1161/CIRCRESAHA.110.231514.

[59] C. M. Witzenburg and J. W. Holmes, “A Comparison of Phenomenologic Growth Laws for Myocardial Hypertrophy,” *J. Elast.*, vol. 129, no. 1, pp. 257–281, Dec. 2017, doi: 10.1007/s10659-017-9631-8.

[60] S. Göktepe, O. J. Abilez, K. K. Parker, and E. Kuhl, “A multiscale model for eccentric and concentric cardiac growth through sarcomerogenesis,” *J. Theor. Biol.*, vol. 265, no. 3, pp. 433–442, Aug. 2010, doi: 10.1016/j.jtbi.2010.04.023.

[61] R. C. P. Kerckhoffs, J. H. Omens, and A. D. McCulloch, “A single strain-based growth law predicts concentric and eccentric cardiac growth during pressure and volume overload,” *Mech. Res. Commun.*, vol. 42, pp. 40–50, Jun. 2012, doi: 10.1016/j.mechrescom.2011.11.004.

[62] Y. Chen *et al.*, “Dynamic molecular and histopathological changes in the extracellular matrix and inflammation in the transition to heart failure in isolated volume overload,” *Am. J. Physiol.-Heart Circ. Physiol.*, vol. 300, no. 6, pp. H2251–H2260, Jun. 2011, doi: 10.1152/ajpheart.01104.2010.

[63] O. Savu *et al.*, “Morphological and Functional Adaptation of the Maternal Heart During Pregnancy,” *Circ. Cardiovasc. Imaging*, vol. 5, no. 3, pp. 289–297, May 2012, doi: 10.1161/CIRCIMAGING.111.970012.

[64] D. Klepach *et al.*, “Growth and remodeling of the left ventricle: A case study of myocardial infarction and surgical ventricular restoration,” *Mech. Res. Commun.*, vol. 42, pp. 134–141, Jun. 2012, doi: 10.1016/j.mechrescom.2012.03.005.

[65] R. D. Patten *et al.*, “17 Beta-Estradiol Differentially Affects Left Ventricular and Cardiomyocyte Hypertrophy Following Myocardial Infarction and Pressure Overload,” *J. Card. Fail.*, vol. 14, no. 3, pp. 245–253, Apr. 2008, doi: 10.1016/j.cardfail.2007.10.024.

[66] J. You *et al.*, “Differential cardiac hypertrophy and signaling pathways in pressure versus volume overload.,” *Am. J. Physiol.-Heart Circ. Physiol.*, p. ajpheart.00212., Dec. 2017, doi: 10.1152/ajpheart.00212.2017.

[67] L. C. Lee, M. Genet, G. Acevedo-Bolton, K. Ordovas, J. M. Guccione, and E. Kuhl, “A computational model that predicts reverse growth in response to mechanical unloading,” *Biomech. Model. Mechanobiol.*, vol. 14, no. 2, pp. 217–229, Apr. 2015, doi: 10.1007/s10237-014-0598-0.

[68] A. Valentín, J. d. Humphrey, and G. a. Holzapfel, “A finite element-based constrained mixture implementation for arterial growth, remodeling, and adaptation: Theory and numerical verification,” *Int. J. Numer. Methods Biomed. Eng.*, vol. 29, no. 8, pp. 822–849, 2013, doi: 10.1002/cnm.2555.

[69] S. Göktepe, O. J. Abilez, and E. Kuhl, “A generic approach towards finite growth with examples of athlete’s heart, cardiac dilation, and cardiac wall thickening,” *J. Mech. Phys. Solids*, vol. 58, no. 10, pp. 1661–1680, Oct. 2010, doi: 10.1016/j.jmps.2010.07.003.

[70] L. A. Taber, “Biomechanical Growth Laws for Muscle Tissue,” *J. Theor. Biol.*, vol. 193, no. 2, pp. 201–213, Jul. 1998, doi: 10.1006/jtbi.1997.0618.

[71] J. A. Niestrawska, C. M. Augustin, and G. Plank, “Computational modeling of cardiac growth and remodeling in pressure overloaded hearts—Linking microstructure to organ phenotype,” *Acta Biomater.*, vol. 106, pp. 34–53, Apr. 2020, doi: 10.1016/j.actbio.2020.02.010.

[72] M. K. Rausch, A. Dam, S. Göktepe, O. J. Abilez, and E. Kuhl, “Computational modeling of growth: systemic and pulmonary hypertension in the heart,” *Biomech. Model. Mechanobiol.*, vol. 10, no. 6, pp. 799–811, Dec. 2011, doi: 10.1007/s10237-010-0275-x.

[73] W. Kroon, T. Delhaas, T. Arts, and P. Bovendeerd, “Computational modeling of volumetric soft tissue growth: application to the cardiac left ventricle,” *Biomech. Model. Mechanobiol.*, vol. 8, no. 4, pp. 301–309, Aug. 2009, doi: 10.1007/s10237-008-0136-z.

[74] M. Latorre, M. R. Bersi, and J. D. Humphrey, “Computational modeling predicts immuno-mechanical mechanisms of maladaptive aortic remodeling in hypertension,” *Int. J. Eng. Sci.*, vol. 141, pp. 35–46, Aug. 2019, doi: 10.1016/j.ijengsci.2019.05.014.

[75] J. Arumugam, J. Mojumder, G. Kassab, and L. C. Lee, “Model of Anisotropic Reverse Cardiac Growth in Mechanical Dyssynchrony,” *Sci. Rep.*, vol. 9, no. 1, p. 12670, Sep. 2019, doi: 10.1038/s41598-019-48670-8.

[76] T. S. E. Eriksson, P. N. Watton, X. Y. Luo, and Y. Ventikos, “Modelling volumetric growth in a thick walled fibre reinforced artery,” *J. Mech. Phys. Solids*, vol. 73, pp. 134–150, Dec. 2014, doi: 10.1016/j.jmps.2014.09.003.

[77] I.-E. Lin and L. A. Taber, “A Model for Stress-Induced Growth in the Developing Heart,” *J. Biomech. Eng.*, vol. 117, no. 3, pp. 343–349, Aug. 1995, doi: 10.1115/1.2794190.

[78] W. Grossman, D. Jones, and L. P. McLaurin, “Wall stress and patterns of hypertrophy in the human left ventricle.,” *J. Clin. Invest.*, vol. 56, no. 1, pp. 56–64, Jul. 1975, doi: 10.1172/JCI108079.

[79] J. L. Emery and J. H. Omens, “Mechanical regulation of myocardial growth during volume-overload hypertrophy in the rat,” *Am. J. Physiol.-Heart Circ. Physiol.*, vol. 273, no. 3, pp. H1198–H1204, Sep. 1997, doi: 10.1152/ajpheart.1997.273.3.H1198.

[80] L. A. Taber and S. Chabert, “Theoretical and experimental study of growth and remodeling in the developing heart,” *Biomech. Model. Mechanobiol.*, vol. 1, no. 1, pp. 29–43, Jun. 2002, doi: 10.1007/s10237-002-0002-3.

[81] R. C. P. Kerckhoffs, J. H. Omens, and A. D. McCulloch, “Mechanical discoordination increases continuously after the onset of left bundle branch block despite constant electrical dyssynchrony in a computational model of cardiac electromechanics and growth,” *Europace*, vol. 14, no. suppl 5, pp. v65–v72, Nov. 2012, doi: 10.1093/europace/eus274.

[82] X. Wang, B. Ren, S. Liu, E. Sentex, P. S. Tappia, and N. S. Dhalla, “Characterization of cardiac hypertrophy and heart failure due to volume overload in the rat,” *J. Appl. Physiol.*, vol. 94, no. 2, pp. 752–763, Feb. 2003, doi: 10.1152/japplphysiol.00248.2002.

[83] S. Kimata and E. Morkin, “Comparison of myosin synthesis in heart and red and white skeletal muscles,” *Am. J. Physiol.-Leg. Content*, vol. 221, no. 6, pp. 1706–1713, Dec. 1971, doi: 10.1152/ajplegacy.1971.221.6.1706.

[84] F. A. Kamal *et al.*, “Simultaneous Adrenal and Cardiac G-Protein–Coupled Receptor-Gβγ Inhibition Halts Heart Failure Progression,” *J. Am. Coll. Cardiol.*, vol. 63, no. 23, pp. 2549–2557, Jun. 2014, doi: 10.1016/j.jacc.2014.02.587.

[85] Y. Liao *et al.*, “Activation of Adenosine A_1 Receptor Attenuates Cardiac Hypertrophy and Prevents Heart Failure in Murine Left Ventricular Pressure-Overload Model,” *Circ. Res.*, vol. 93, no. 8, pp. 759–766, Oct. 2003, doi: 10.1161/01.RES.0000094744.88220.62.

[86] K. Lindpaintner *et al.*, “Tissue Renin-Angiotensin Systems: Focus on the Heart,” *J. Hypertens.*, vol. 5, p. S33, Jul. 1987.

[87] B. H. Lorell and B. A. Carabello, “Left Ventricular Hypertrophy: Pathogenesis, Detection, and Prognosis,” *Circulation*, vol. 102, no. 4, pp. 470–479, Jul. 2000, doi: 10.1161/01.CIR.102.4.470.

[88] A. Rapacciuolo, G. Esposito, K. Caron, L. Mao, S. A. Thomas, and H. A. Rockman, “Important role of endogenous norepinephrine and epinephrine in the development of in vivo pressure-overload cardiac hypertrophy,” *J. Am. Coll. Cardiol.*, vol. 38, no. 3, pp. 876–882, Sep. 2001, doi: 10.1016/S0735-1097(01)01433-4.

[89] H. Schunkert, V. J. Dzau, S. S. Tang, A. T. Hirsch, C. S. Apstein, and B. H. Lorell, “Increased rat cardiac angiotensin converting enzyme activity and mRNA expression in pressure overload left ventricular hypertrophy. Effects on coronary resistance, contractility, and relaxation.,” *J. Clin. Invest.*, vol. 86, no. 6, pp. 1913–1920, Dec. 1990, doi: 10.1172/JCI114924.

[90] T. Yamazaki, I. Komuro, and Y. Yazaki, “Molecular mechanism of cardiac cellular hypertrophy by mechanical stress,” *J. Mol. Cell. Cardiol.*, vol. 27, no. 1, pp. 133–140, Jan. 1995, doi: 10.1016/S0022-2828(08)80013-2.

[91] F. A. McAlister *et al.*, “Cardiac Resynchronization Therapy for Patients With Left Ventricular Systolic DysfunctionA Systematic Review,” *JAMA*, vol. 297, no. 22, pp. 2502–2514, Jun. 2007, doi: 10.1001/jama.297.22.2502.

[92] S. Baldasseroni *et al.*, “Left bundle-branch block is associated with increased 1-year sudden and total mortality rate in 5517 outpatients with congestive heart failure: A report from the Italian network on congestive heart failure,” *Am. Heart J.*, vol. 143, no. 3, pp. 398–405, Mar. 2002, doi: 10.1067/mhj.2002.121264.

[93] K. C. Bilchick, R. H. Helm, and D. A. Kass, “Physiology of biventricular pacing,” *Curr. Cardiol. Rep.*, vol. 9, no. 5, pp. 358–365, Sep. 2007, doi: 10.1007/BF02938362.

[94] W. Shamim *et al.*, “Intraventricular conduction delay: a prognostic marker in chronic heart failureq,” *Int. J. Cardiol.*, p. 8, 1999.

[95] F. W. Prinzen, C. H. Augustijn, T. Arts, M. A. Allessie, and R. S. Reneman, “Redistribution of myocardial fiber strain and blood flow by asynchronous activation,” *Am. J. Physiol.-Heart Circ. Physiol.*, vol. 259, no. 2, pp. H300–H308, Aug. 1990, doi: 10.1152/ajpheart.1990.259.2.H300.

[96] D. A. Auger *et al.*, “Imaging left-ventricular mechanical activation in heart failure patients using cine DENSE MRI: Validation and implications for cardiac resynchronization therapy,” *J. Magn. Reson. Imaging*, vol. 46, no. 3, pp. 887–896, 2017, doi: 10.1002/jmri.25613.

[97] L. S. Fixsen *et al.*, “Echocardiographic Assessment of Left Bundle Branch–Related Strain Dyssynchrony: A Comparison With Tagged MRI,” *Ultrasound Med. Biol.*, vol. 45, no. 8, pp. 2063–2074, Aug. 2019, doi: 10.1016/j.ultrasmedbio.2019.03.012.

[98] K. Vernooy *et al.*, “Left bundle branch block induces ventricular remodelling and functional septal hypoperfusion,” *Eur. Heart J.*, vol. 26, no. 1, pp. 91–98, Jan. 2005, doi: 10.1093/eurheartj/ehi008.

[99] M. F. M. van Oosterhout *et al.*, “Asynchronous Electrical Activation Induces Asymmetrical Hypertrophy of the Left Ventricular Wall,” *Circulation*, vol. 98, no. 6, pp. 588–595, Aug. 1998, doi: 10.1161/01.CIR.98.6.588.

[100] F. W. Prinzen *et al.*, “Asymmetric thickness of the left ventricular wall resulting from asynchronous electric activation: A study in dogs with ventricular pacing and in patients with left bundle branch block,” *Am. Heart J.*, vol. 130, no. 5, pp. 1045–1053, Nov. 1995, doi: 10.1016/0002-8703(95)90207-4.

[101] C. M. Tracy *et al.*, “2012 ACCF/AHA/HRS Focused Update of the 2008 Guidelines for Device-Based Therapy of Cardiac Rhythm Abnormalities,” *J. Am. Coll. Cardiol.*, vol. 60, no. 14, pp. 1297–1313, Oct. 2012, doi: 10.1016/j.jacc.2012.07.009.

[102] Authors/Task Force Members *et al.*, “2013 ESC Guidelines on cardiac pacing and cardiac resynchronization therapy: The Task Force on cardiac pacing and resynchronization therapy of the European Society of Cardiology (ESC). Developed in collaboration with the European Heart Rhythm Association (EHRA),” *Europace*, vol. 15, no. 8, pp. 1070–1118, Aug. 2013, doi: 10.1093/europace/eut206.

[103] M. R. Bristow, S. Krueger, P. Carson, and B. G. White, “Cardiac-Resynchronization Therapy with or without an Implantable Defibrillator in Advanced Chronic Heart Failure,” *N. Engl. J. Med.*, p. 11, 2004.

[104] J. G. F. Cleland, E. Erdmann, and L. Kappenberger, “The Effect of Cardiac Resynchronization on Morbidity and Mortality in Heart Failure,” *N. Engl. J. Med.*, p. 11, 2005.

[105] A. J. Moss *et al.*, “Cardiac-Resynchronization Therapy for the Prevention of Heart-Failure Events,” *N. Engl. J. Med.*, vol. 361, no. 14, pp. 1329–1338, Oct. 2009, doi: 10.1056/NEJMoa0906431.

[106] M. G. St John Sutton *et al.*, “Effect of Cardiac Resynchronization Therapy on Left Ventricular Size and Function in Chronic Heart Failure,” *Circulation*, vol. 107, no. 15, pp. 1985–1990, Apr. 2003, doi: 10.1161/01.CIR.0000065226.24159.E9.

[107] P. Steendijk *et al.*, “Hemodynamic Effects of Long-Term Cardiac Resynchronization Therapy: Analysis by Pressure-Volume Loops,” *Circulation*, vol. 113, no. 10, pp. 1295–1304, Mar. 2006, doi: 10.1161/CIRCULATIONAHA.105.540435.

[108] M. St. John Sutton *et al.*, “Left Ventricular Architecture, Long-Term Reverse Remodeling, and Clinical Outcome in Mild Heart Failure With Cardiac Resynchronization,” *JACC Heart Fail.*, vol. 5, no. 3, pp. 169–178, Mar. 2017, doi: 10.1016/j.jchf.2016.11.012.

[109] E. Chung, F. Yeung, and L. A. Leinwand, “Akt and MAPK signaling mediate pregnancy-induced cardiac adaptation,” *J. Appl. Physiol.*, vol. 112, no. 9, pp. 1564–1575, May 2012, doi: 10.1152/japplphysiol.00027.2012.

[110] R. Ramachandran, X. Chen, C. M. Kramer, F. H. Epstein, and K. C. Bilchick, “Singular Value Decomposition Applied to Cardiac Strain from MR Imaging for Selection of Optimal Cardiac Resynchronization Therapy Candidates,” *Radiology*, vol. 275, no. 2, pp. 413–420, May 2015, doi: 10.1148/radiol.14141578.

[111] D. Mozaffarian *et al.*, “Prediction of Mode of Death in Heart Failure: The Seattle Heart Failure Model,” *Circulation*, vol. 116, no. 4, pp. 392–398, Jul. 2007, doi: 10.1161/CIRCULATIONAHA.106.687103.

[112] K. C. Bilchick *et al.*, “CMR DENSE and the Seattle Heart Failure Model Inform Survival and Arrhythmia Risk After CRT,” *JACC Cardiovasc. Imaging*, vol. 13, no. 4, pp. 924–936, Apr. 2020, doi: 10.1016/j.jcmg.2019.10.017.

[113] M. Cikes *et al.*, “Machine learning-based phenogrouping in heart failure to identify responders to cardiac resynchronization therapy: Machine learning-based approach to patient selection for CRT,” *Eur. J. Heart Fail.*, vol. 21, no. 1, pp. 74–85, Jan. 2019, doi: 10.1002/ejhf.1333.

[114] A. K. Feeny *et al.*, “Machine Learning of 12-Lead QRS Waveforms to Identify Cardiac Resynchronization Therapy Patients With Differential Outcomes,” *Circ. Arrhythm. Electrophysiol.*, vol. 13, no. 7, Jul. 2020, doi: 10.1161/CIRCEP.119.008210.

[115] Y. Iwanaga *et al.*, “B-Type Natriuretic Peptide Strongly Reflects Diastolic Wall Stress in Patients With Chronic Heart Failure,” *J. Am. Coll. Cardiol.*, vol. 47, no. 4, pp. 742–748, Feb. 2006, doi: 10.1016/j.jacc.2005.11.030.

[116] F. Alpendurada *et al.*, “Right ventricular dysfunction is a predictor of non-response and clinical outcome following cardiac resynchronization therapy,” *J. Cardiovasc. Magn. Reson.*, vol. 13, no. 1, p. 68, Dec. 2011, doi: 10.1186/1532-429X-13-68.

[117] J.-H. Park *et al.*, “Echocardiographic Predictors of Reverse Remodeling After Cardiac Resynchronization Therapy and Subsequent Events,” *Circ. Cardiovasc. Imaging*, vol. 6, no. 6, pp. 864–872, Nov. 2013, doi: 10.1161/CIRCIMAGING.112.000026.

[118] W. P. Santamore and L. J. Dell’Italia, “Ventricular interdependence: Significant left ventricular contributions to right ventricular systolic function,” *Prog. Cardiovasc. Dis.*, vol. 40, no. 4, pp. 289–308, Jan. 1998, doi: 10.1016/S0033-0620(98)80049-2.

[119] J. A. Doust, R. Lehman, and P. Glasziou, “The Role of BNP Testing in Heart Failure,” *Am. Fam. Physician*, vol. 74, no. 11, pp. 1893–1898, Dec. 2006.

[120] R. Deo and J. A. de Lemos, “B-type natriuretic peptide in ischemic heart disease,” *Curr. Cardiol. Rep.*, vol. 5, no. 4, pp. 271–277, Jul. 2003, doi: 10.1007/s11886-003-0062-8.

[121] A. Brenyo *et al.*, “Brain Natriuretic Peptide and Cardiac Resynchronization Therapy in Patients With Mildly Symptomatic Heart Failure,” *Circ. Heart Fail.*, vol. 6, no. 5, pp. 998–1004, Sep. 2013, doi: 10.1161/CIRCHEARTFAILURE.112.000174.

[122] W. P. Santamore and D. Burkhoff, “Hemodynamic consequences of ventricular interaction as assessed by model analysis,” *Am. J. Physiol.-Heart Circ. Physiol.*, Jan. 1991, doi: 10.1152/ajpheart.1991.260.1.H146.

[123] R. C. P. Kerckhoffs, M. L. Neal, Q. Gu, J. B. Bassingthwaighte, J. H. Omens, and A. D. McCulloch, “Coupling of a 3D Finite Element Model of Cardiac Ventricular Mechanics to Lumped Systems Models of the Systemic and Pulmonic Circulation,” *Ann. Biomed. Eng.*, vol. 35, no. 1, pp. 1–18, Dec. 2006, doi: 10.1007/s10439-006-9212-7.

[124] T. Arts, T. Delhaas, P. Bovendeerd, X. Verbeek, and F. W. Prinzen, “Adaptation to mechanical load determines shape and properties of heart and circulation: the CircAdapt model,” *Am. J. Physiol.-Heart Circ. Physiol.*, vol. 288, no. 4, pp. H1943–H1954, Apr. 2005, doi: 10.1152/ajpheart.00444.2004.

[125] D. A. Beard, K. H. Pettersen, B. E. Carlson, S. W. Omholt, and S. M. Bugenhagen, “A computational analysis of the long-term regulation of arterial pressure,” *F1000Research*, vol. 2, p. 208, Oct. 2013, doi: 10.12688/f1000research.2-208.v1.

[126] C. C. Aggarwal, *Neural Networks and Deep Learning: A Textbook*, 1st ed. 2018 edition. Cham, Switzerland: Springer, 2018.

[127] N. Frey and E. N. Olson, “Cardiac Hypertrophy: The Good, the Bad, and the Ugly,” *Annu. Rev. Physiol.*, vol. 65, no. 1, pp. 45–79, Mar. 2003, doi: 10.1146/annurev.physiol.65.092101.142243.